A Reduced-Order Framework for the Thermo-hydraulic Design of Additively Manufactured Compact Heat Exchangers

Heat Sink Design and Optimization

Sérgio Machado

Delft University of Technology

TU Delft Ergon research

A Reduced-Order Framework for the Thermo-hydraulic Design of Additively Manufactured Compact Heat Exchangers

Heat Sink Design and Optimization

by

Sérgio Machado

to obtain the degree of Master of Science

at the Delft University of Technology,

to be defended publicly on Friday January 30, 2026 at 10:00 AM.

Thesis committee:	Dr. Matteo Pini	TU Delft, Chair
	Dr. Woutijn Baars	TU Delft, External Examiner
	Dr. Carlo De Servi	TU Delft, Supervisor
	Floyd van Steen	TU Delft, Supervisor
	Dr. Lorenzo Mazzei	Ergon Research, Supervisor
	Niccolò Casini	Ergon Research, Supervisor

Place:	Faculty of Aerospace Engineering, Delft
Project duration:	April 1, 2023 – December 31, 2025
Student number:	6068626

Cover: A 2D Simulation of a Kelvin-Helmholtz instability by user u/unnecessaryellipses1, Reddit, CC BY

An electronic version of this thesis is available at `http://repository.tudelft.nl/`.

TU Delft Ergon research

Preface

This thesis marks the end of my academic journey, a journey that started in a small town in the north of Portugal, continued through Lisbon, made its way to the Netherlands, and ended up concluding in beautiful Florence. This project sums up the questions, challenges, frustrations, and victories of the past year, something I am very proud of. However, I could not have done it alone.

To begin with, this would not have been possible without the guidance and advice of both my supervisors, Dr. Carlo De Servi and Floyd van Steen. Thank you for being supportive, for constantly bringing new ideas to our discussions, and for the countless revisions in the final stretch.

On the other end of the supervisory team, I had Dr. Lorenzo Mazzei and Niccolò Casini from Ergon Research. Your daily support and encouragement represent a large part of this project. Thank you for welcoming me into the team and for making me feel like I belonged from the very beginning. This gratitude extends to all the people in that office that, underneath all the madness, were a great prototype of my Italian family. In particular, thank you Giulio for developing my critical thinking through your simple but wise words: "Ma come?". You all truly made Florence a lot closer to home.

To all the friends I have made throughout this journey, thank you for inspiring me and making all these years far from home go by so fast. To those who have been with me since the beginning of my life, thank you for making any distance feel small. This would not have been worth it without you. To Carolina, thank you for listening to me and pushing me through the worst steps, despite not having the remotest idea of what this thesis is about.

To my family, to my mom, thank you for the incredible effort you made to provide me with all of these opportunities and for all the unconditional support. To my uncle, Osvaldo, thank you for the example of integrity and perseverance. To Marta, thank you for all the care and support, and for always believing. To my grandmother, Milinha, thank you for inspiring me and being my role-model. This work is dedicated to you.

Sérgio Machado
Delft, January 2026

Contents

List of Figures

List of Tables

Nomenclature

Abbreviations

Abbreviation	Definition
AM	Additive Manufacturing
BCC	Body Cubic Centered
CFD	Computational Fluid Dynamics
EAP	Electrified Aircraft Propulsion
GCI	Grid Convergence Index
NTU	Number of Transfer Units
RANS	Reynolds-Averaged Navier-Stokes
RBF	Radial Basis Function
RMSE	Root Mean Square Error
RVE	Representative Volume Elements
TPMS	Triply Periodic Minimal Surface
WEG	Water-Ethylene Glycol

Symbols

Symbol	Definition	Unit
A	Area	$[m^2]$
C	Heat Capacity Rate	$[J\,s^{-1}K^{-1}]$
D_h	Hydraulic Diameter	$[m]$
f	Friction Factor	[-]
h	Heat Transfer Coefficient	$[W\,m^{-2}K^{-1}]$
H	Height	$[m]$
L	Length	$[m]$
m	Fin Parameter	[-]
$\dot{m}$	Mass Flow Rate	$[kg\,s^{-1}]$
N	Number of Fins	[-]
Nu	Nusselt Number	[-]
p	Perimeter	$[m]$
P	Pressure	$[Pa]$
Pr	Prandtl Number	[-]
$\dot{q}$	Wall Heat Flux	$[W\,m^{-2}]$
$\dot{Q}$	Heat Transfer Rate	$[W]$
R	Thermal Resistance	$[K\,W^{-1}]$
Re	Reynolds Number	[-]
t	Thickness	$[m]$
T	Temperature	$[K]$

Symbol	Definition	Unit
U	Overall Heat Transfer Coefficient	$[W\,m^{-2}K^{-1}]$
v	Bulk Velocity	$[m\,s^{-1}]$
V	Volume	$[m^3]$
Δ	Grid spacing	$[m]$
ϵ	Thermal effectiveness	[-]
η	Efficiency	[-]
λ	Thermal conductivity	$[W\,m^{-1}K^{-1}]$
μ	Dynamic viscosity	$[Pa\,s]$
ρ	Density	$[kg\,m^{-3}]$
σ	Sigmoid-type function	[-]
ϕ	Porosity	[-]

Subscripts and Superscripts

Symbol	Definition
b	Bulk
$base$	Base
c	Cross-section
eff	Effective
f	Fluid
$finned$	Finned
$global$	Global
in	Inlet
$interf$	Interface
max	Maximum
min	Minimum
o	Overall
out	Outlet
p	Pore definition
s	Superficial definition; solid
$total$	Total
uc	Unit cell
V	Velocity
w	Wall

Part I

Introduction and Research Definition

1

Introduction

Aviation today makes a non-trivial contribution to global anthropogenic greenhouse gas emissions, accounting for roughly 2.5% of energy-related CO_2 emissions [1]. Although this share may seem modest, as seen in Figure 1, global aviation demand continues to grow. This causes emissions to rise even faster than for other methods of transportation, despite efforts to increase energy efficiency [2].

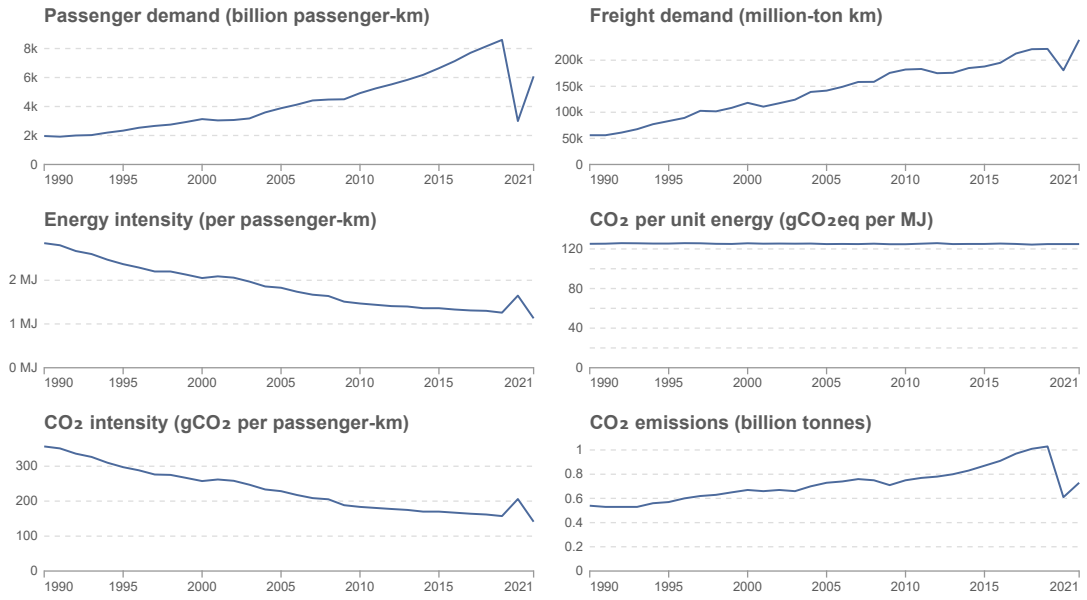

Figure 1: Overview of global aviation demand impact on CO_2 emissions from 1990 to 2021, regardless of the reduction in CO_2 intensity per passenger. Adapted from [2].

In addition, non-$\mathrm{CO_2}$ effects further exacerbate aviation's climate impact, increasing its contribution to around 4% of global warming to date [2]. The main non-$\mathrm{CO_2}$ contributions come from the formation of persistent contrails, as well as from chemical processes in the atmosphere involving nitrogen oxides ($\mathrm{NO_x}$) [3]. $\mathrm{NO_x}$ emissions at low altitudes affect local air quality and threaten respiratory health, while at high altitudes they lead to a series of photochemical reactions that enhance ozone production (warming effect) and reduce atmospheric methane (cooling effect) [3, 4].

With current measures deemed insufficient to meet climate goals established in the Paris Agreement [5], the aerospace industry is exploring different solutions, such as the electrification of aircraft propulsion, to reduce or eliminate in-flight carbon emissions. Electrified aircraft propulsion (EAP) is widely seen as a promising approach, particularly for short-haul and regional aviation. However, achieving a significant reduction in emissions via hybrid-electric and fully-electric flight comes with significant technical challenges, especially in meeting the extreme performance requirements of aircraft applications.

An important barrier to the success of EAP is the thermal management of the electrical components. Although these components typically operate at high efficiency (over 90%), the electric power levels required for some EAP aircraft concepts result in megawatts of waste heat that must be effectively removed. The rejection into ambient of these thermal power is complicated by the relatively low operating temperature limits of electric components, approximately 40°C for batteries and power electronics and up to 120°C for motors [6]. Addressing these cooling requirements without incurring excessive penalties in power consumption, aerodynamic drag, or system weight is essential. If not carefully mitigated, such penalties could significantly reduce, or even negate, the overall system-level benefits of an electrified propulsion architecture [7].

Aerospace is not alone in its quest for advanced thermal management technologies. Across multiple industries, there is a growing demand for compact, high-performance thermal management solutions. As devices and systems become more powerful, yet lighter and smaller, they generate higher heat fluxes per unit volume. This calls for thermal solutions that are simultaneously lightweight, compact, and capable of handling extreme heat loads. Unfortunately, traditional thermal management hardware is struggling to keep up with these requirements. Conventional heat exchangers (such as finned tube coils, plate-fin exchangers, or roll-bonded cold plates) are often bulkier than required and offer limited potential for further performance improvement because their designs have already reached the limits imposed by traditional manufacturing processes (machining, casting, extrusion, stamping, and brazing) [8].

In recent years, additive manufacturing (AM), also known as metal 3D printing, has gained exponential interest across several industries, particularly in the aerospace and energy sectors, given its potential to significantly reduce part count, weight, material waste, and possibly manufacturing costs, depending upon the application [8]. AM enables the creation of novel geometric designs that enhance the complexity and performance of thermal management components that are impossible to produce using conventional manufacturing techniques. With the growing adoption of AM, the focus shifts toward developing more advanced and efficient cooling systems.

Additive manufacturing has fundamentally changed what is possible in thermal management design. In recent decades, this capability has enabled the use of porous and lattice-based structures, geometries inspired by natural forms that were previously too complex or expensive to manufacture using conventional methods. Unlike traditional cooling geometries limited by machining and assembly processes, these AM-enabled structures offer several advantages: they improve fluid mixing and create more uniform temperature distributions through their three-dimensional, interconnected flow paths. Their high surface area density and structural strength allow for compact, lightweight designs. The geometric versatility of lattice architectures further allows their thermal and flow characteristics to be tailored to specific applications [9].

However, the thermal and fluid-dynamic behavior of these structures is fundamentally different from traditional finned surfaces. Flow through lattice geometries is unsteady and three-dimensional, often resembling flow through porous media rather than flow over discrete fins. Consequently, the characterization work previously done for classical secondary surfaces must be revisited for these new geometries. Accurate characterization requires detailed numerical simulations or experimental

studies, from which new correlations can be developed. This need has motivated growing research interest in understanding and modeling of the thermal and fluid-dynamic behavior of lattice-based heat transfer surfaces.

For strut-based lattices, initial efforts focused on cross-topology benchmarking to establish performance hierarchies and identify the physical mechanisms governing thermo-hydraulic behavior. Comparative studies have identified which lattice topologies perform best under specific conditions. Kaur et al. [10], Castelli et al. [11], and Corbett and Thole [12] evaluated multiple lattice families, including octet, TKD, FD-CUBE, cube, Kagome, and body-centered cubic (BCC) structures, demonstrating that topology fundamentally determines the trade-off between heat transfer enhancement and pressure loss minimization. Importantly, Kaur et al. found that performance rankings among these topologies are sensitive to thermal boundary conditions, indicating that optimal lattice selection is highly application-specific. Building on these topology comparisons, parametric investigations by Liang et al. [13] and Lorenzon et al. [14] examined how strut geometry (specifically strut shape and diameter) affects the performance within individual lattice families.

Parallel efforts have advanced the understanding of flow and heat transfer surface-based lattices, also called triply periodic minimal surfaces (TPMS), where research has evolved from pore-scale hydrodynamics to conjugate heat-transfer modeling and, more recently, to experimental validation at both coupon and component scale. Early computational work by Rathore et al. [15], Piedra et al. [16], and Ornelas-Ramón et al. [17] quantified permeability, inertial drag coefficients, and laminar Nusselt number relationships for diamond, IWP, primitive, and gyroid structures. Subsequent studies by Rathore et al. [18], Torri et al. [19], and Yan et al. [20] extended the analysis to conjugate heat transfer in multi-cell domains and full heat exchanger configurations, showing that TPMS structures outperform conventional fins but incur higher pressure drop penalties. Turbulent regime investigations by Samson et al. [21], Wang et al. [22], and Brambati et al. [23] produced increasingly general correlations, with Brambati et al. developing a cross-fluid, multi-topology formulation. Experimental campaigns by Reynolds et al. [24], Tang et al. [25, 26], and Zou et al. [27] validated numerical predictions and confirmed consistent performance trends across porosities and topologies.

Despite this extensive body of work, existing correlations remain topology-dependent and regime-specific, with inconsistent treatment of parameters, boundary conditions, and data reduction methods, as highlighted by Caket et al. [28] in their comprehensive review. Taking this into account, these closure relationships for friction and heat transfer derived from laminar and turbulent studies do not yet enable robust reduced-order modeling of these geometries across the full Reynolds-number spectrum. At the same time, emerging design and optimization frameworks for AM heat exchangers, ranging from stochastic and evolutionary algorithms to topology and multiscale optimization, increasingly rely on high-fidelity CFD evaluations with high computational cost for preliminary design [29–32] or on black-box surrogate models with limited physical interpretability [29, 33].

Considering this, the main objective of this research project is to develop and verify a reduced-order model for the design and optimization of additively manufactured compact heat exchangers. This reduced-order model should connect the microscale thermo-fluid behavior of complex lattice geometries to component-level performance models suitable for preliminary design and design optimization. It should also allow for a computationally efficient and physically interpretable methodology to support the early-stage development of advanced thermal management systems enabled by additive manufacturing.

2

Research Definition

To accomplish this, the research is organized around three intermediate objectives and three guiding research questions that define the scope and methodology of the work.

2.1. Research Objectives

Research Objective 1: Characterization of the thermo-hydraulic performance of lattice structures.

The goal is to establish a comprehensive dataset of friction factor and heat transfer performance for four representative lattice geometries (Pin Fin, BCC, Gyroid, and Diamond). This dataset should span laminar, transitional, and turbulent flow conditions and include the effects of porosity and fluid properties. The outcome is an extensive database for correlation development, addressing the current lack of information across the full range of operating conditions.

Research Objective 2: Formulation of performance correlations for friction factor and Nusselt number.

The goal is to formulate mathematical correlations for friction factor and Nusselt number that remain valid across all flow regimes and account for geometric and fluid property variations. These correlations should enable performance predictions for different lattice designs and working fluids without requiring case-by-case simulations. The outcome must provide designers with predictive tools that work beyond the narrow ranges of existing correlations, particularly capturing the under-represented transitional regime.

Research Objective 3: Formulation and verification of a preliminary design model for heat exchangers incorporating lattice structures.

The goal is to create an $\epsilon - NTU$-based model that predicts heat exchanger performance with sufficient accuracy for design purposes while being computationally efficient. The model should reproduce both thermal and hydraulic behavior within acceptable error bounds when compared against high-fidelity simulations. The outcome must be a verified tool that enables fast design exploration and optimization without the computational burden of CFD analysis.

2.2. Research Questions

To meet these objectives, the research is structured around the following research questions and sub-questions:

RQ 1 - What computational setup allows for the characterization of the thermo-hydraulic behavior of lattice structures in a way that captures the effects of geometry, flow regime, and porosity across the entire laminar-turbulent spectrum?

RQ 2 - What generalized relationships can accurately describe the friction factor and Nusselt number of lattice structures across varying geometries and flow regimes?

Sub-questions:

RQ 2.1 - What is the most suitable characteristic length scale for the non-dimensionalization of thermo-hydraulic performance data to develop general correlations?

RQ 2.2 - Which correlation expressions can accurately capture the trend in friction factor and Nusselt number from laminar to turbulent flow, ensuring also smooth and physically meaningful trends over the transitional regime?

RQ 2.3 - How do the proposed correlations compare to existing empirical models in terms of predictive capability and generalization?

RQ 3 - How can the derived correlations be integrated into a reduced-order model to accurately predict the performance of heat exchangers?

Sub-questions:

RQ 3.1 - What are the limitations of simplified reduced-order approaches in predicting the thermo-hydraulic performance of heat-exchangers?

RQ 3.2 - How much is the difference in terms of computational time, memory requirements, and solution accuracy between the reduced-order model and high-fidelity CFD analysis?

2.3. Thesis Outline

The thesis report is structured as follows. The report continues with Part II, which is organized as a scientific article and constitutes the core part of the thesis. This part presents the adopted numerical methodology for the thermo-hydraulic characterization of lattice-based heat transfer structures and the development of correlation-based reduced-order heat exchanger models including their validation against high-fidelity CFD data. It concludes with the application of the developed tool in an optimization study targeting the optimal design of a cold plate. Part III comprises the literature study, providing a comprehensive review of advanced secondary heat transfer surface characterization techniques, component-level modeling approaches, and heat exchanger performance optimization methods. This review supports the research definition, enabling the identification of the research gap and the formulation of the research objectives. Finally, Part IV concludes the report by summarizing the main findings of the work, addressing the formulated research questions, and outlining recommendations for future developments aimed at broadening the applicability of the proposed framework.

Part II

Scientific Article

A Reduced-Order Framework for the Thermo-Hydraulic Design of Additively Manufactured Compact Heat Exchangers

Sérgio Machado[1,2], **Niccolò Casini**[2], **Lorenzo Mazzei**[2], **Riccardo Da Soghe**[2], **Floyd van Steen**[1], **Carlo De Servi**[1]

[1]*Delft University of Technology, 2629 HS Delft, The Netherlands*
[2]*Ergon Research S.r.l., Via Giuseppe Campani 50, 50127, Firenze (FI), Italy*

The increasing electrification of aircraft subsystems and the integration of high-power-density components are creating significant challenges for onboard thermal management systems. These key subsystems are reaching their performance limits, motivating the development of new advanced solutions. One promising option is the adoption of innovative heat exchanger concepts featuring complex internal geometries, such as strut-based lattice structures, and triply periodic minimal surfaces (TPMS), that are only feasible to manufacture through additive processes. The aim of this work is to develop a systematic methodology to characterize the thermo-hydraulic performance of advanced heat transfer structures based on periodic unit cell (Representative Volume Elements) simulations. The resulting numerical data are then used to calibrate reduced order models suitable for the preliminary design of heat transfer devices. More in detail, the study focuses on the characterization of four heat transfer topologies over a wide range of Reynolds and Prandtl numbers and structure porosities. The performance data from the simulations were used to derive empirical correlations for the friction factor and Nusselt number as a function of the topology porosity. These correlations were then implemented into an $\epsilon - NTU$-based model to support preliminary design activities. To verify this methodology, a cold plate was analyzed and the results were validated against CFD simulations. The methodology showed adequate accuracy for preliminary design, providing reliable predictions where CFD is computationally prohibitive. Future work will expand geometric inputs beyond porosity to broaden the design space of additively manufactured heat transfer devices.

1. Introduction

The increasing electrification of aircraft subsystems and the integration of high-power-density components are creating significant challenges for onboard thermal management systems. An important barrier to the success of electrified aircraft propulsion is the thermal management of the electrical components. Although these components typically operate at high efficiency (more than 90%), given the levels of electric power that the propulsion system is required to deliver, the cooling loads aboard aircraft can be on the order of several megawatts. As devices and systems become more powerful, yet lighter and smaller, they generate higher heat fluxes per unit volume. This requires thermal solutions that are simultaneously lightweight, compact and capable of handling extreme heat loads. Unfortunately, conventional thermal management hardware is struggling to keep up with these requirements because their designs have already reached the limits imposed by traditional manufacturing processes.

In the field of heat transfer devices, additive manufacturing (AM) has fundamentally expanded the design space. In recent years, this capability has enabled the development of heat exchangers with porous and lattice-based structures, that were previously too complex to manufacture using conventional methods. Unlike traditional heat transfer geometries, these AM-enabled topologies offer several advantages: they improve fluid mixing and create a more uniform temperature distribution along the flow paths. Their high surface area density and structural strength allow for more compact and lightweight thermal designs. Furthermore, the geometric versatility of lattice architectures allows their thermal and flow characteristics to be tailored to meet specific requirements.

Since the adoption of secondary surfaces in heat exchanger design, the scientific community has made sustained efforts to characterize their thermo-hydraulic performance. However, the thermal and fluid characteristics of the lattice structures are fundamentally different from those of traditional finned surfaces. Flow through lattice geometries is inherently unsteady and three-dimensional, often resembling flow through porous media rather than flow in finned channels. Consequently, the characterization work previously done for classical secondary surfaces must be revisited for these new geometries. Accurate characterization of

their thermo-hydraulic performance requires detailed numerical simulations or experimental studies, from which new correlations can be developed. This need has motivated an increasing number of studies targeting the modeling of the thermal and fluid behavior of lattice-based heat transfer surfaces, although this research area still remains underdeveloped.

For strut-based lattices, initial efforts focused on cross-topology benchmarking to establish performance hierarchies and identify the physical mechanisms governing thermo-hydraulic behavior. Comparative studies have identified which lattice topologies perform best under specific conditions. Kaur et al. [10], Castelli et al. [11], and Corbett and Thole [12] evaluated multiple lattice families, including octet, TKD, FD-CUBE, cube, Kagome, and body-centered cubic (BCC) structures, demonstrating that topology fundamentally determines the trade-off between heat transfer enhancement and pressure loss minimization. Importantly, Kaur et al. found that performance rankings among these topologies are sensitive to thermal boundary conditions, indicating that optimal lattice selection is highly application-specific. Building on these topology comparisons, parametric investigations by Liang et al. [13] and Lorenzon et al. [14] examined how strut geometry (specifically strut shape and diameter) affects the performance within individual lattice families. Their results confirm that decreasing porosity (thereby increasing wetted area and enhancing fluid mixing) improves heat transfer at the cost of higher hydraulic losses.

Parallel efforts have advanced the understanding of surface-based lattices, also called triply periodic minimal surfaces (TPMS), where research has evolved from pore-scale hydrodynamics to conjugate heat-transfer modeling and, more recently, to experimental validation at both coupon and component scale. Early computational work by Rathore et al. [15], Piedra et al. [16], and Ornelas-Ramón et al. [17] quantified permeability, inertial drag coefficients, and laminar Nusselt number relationships for diamond, IWP, primitive, and gyroid structures. Subsequent studies by Rathore et al. [18], Torri et al. [19], and Yan et al. [20] extended the analysis to conjugate heat transfer in multi-cell domains and full heat exchanger configurations, showing that TPMS structures outperform conventional fins but incur higher pressure drop penalties. Turbulent regime investigations by Samson et al. [21], Wang et al. [22], and Brambati et al. [23] produced increasingly general correlations, with Brambati et al. developing a cross-fluid, multi-topology formulation. Experimental campaigns by Reynolds et al. [24], Tang et al. [25, 26], and Zou et al. [27] validated numerical predictions and confirmed consistent performance trends across porosities and topologies.

Despite this extensive body of work, existing correlations remain topology-dependent and regime-specific, with inconsistent treatment of parameters, boundary conditions, and data reduction methods, as highlighted by Caket et al. [28] in their comprehensive review. Taking this into account, these closure relationships for friction and heat transfer derived from laminar and turbulent studies do not yet enable robust reduced-order modeling of additively manufactured geometries across the full Reynolds-number spectrum. At the same time, emerging design and optimization frameworks for AM heat exchangers, ranging from stochastic and evolutionary algorithms to topology and multiscale optimization, increasingly rely on high-fidelity CFD evaluations with prohibitive computational cost for preliminary design [29–32] or on black-box surrogate models with limited physical interpretability [29, 33].

The main goal of this work is to develop and verify a reduced-order framework for the thermo-hydraulic design and optimization of additively manufactured compact heat exchangers. This framework should connect micro-scale thermo-fluid characteristics of lattice structures to component-level performance predictions suitable for preliminary design optimization. To establish this connection, the study begins with a systematic characterization of the thermo-hydraulic performance of four geometries (pin fins, BCC, gyroid, and diamond) using periodic unit cell simulations. The resulting numerical data are used to develop correlations for the friction factor and the Nusselt number, which are subsequently implemented in an $\epsilon - NTU$-based model for preliminary design.

To verify the proposed framework, a cold plate design case study for power electronics cooling is used to identify optimal geometries targeting two competing global objectives: maximizing thermal effectiveness while minimizing pressure drop. The reduced-order model predictions for these optimal designs are then validated against CFD simulations. Lastly, the computational efficiency of the reduced-order model enables exploration of a more sophisticated design approach in which porosity is treated as a spatially varying parameter rather than a uniform property. This additional degree of freedom is investigated as a means to improve temperature uniformity across the cold plate while preserving the global thermo-hydraulic performance of an optimal uniform-porosity design.

2. Methodology

In this section, the methodology to design and optimize the performance of a cold plate will be outlined.

2.1. Characterization of Lattice Structures

The foundation of the model lies in characterizing the selected lattice structures in terms of both pressure losses and thermal performance. To establish correlation laws that accurately describe the behavior of these structures, several approaches are available. Traditionally, correlations for smooth channels and conventional fins have been derived primarily from experimental data. However, conducting a comprehensive experimental campaign requires significant time and resources for manufacturing test articles. Given these limitations, the present work will characterize these novel lattice structures through numerical simulations.

Four geometries were selected for this analysis: pin fins, BCC, gyroid, and diamond. A graphical representation of the unit cell of each geometry is presented in Fig. 2. Pin fins have been considered in the study because they are one of the most widely used cooling features in traditional heat exchangers. Thus, their performance serves as the benchmark for the AM topologies analyzed in this study. The BCC is selected as a representative example of strut-based lattices, whereas the gyroid and diamond structures represent surface-based lattices. The pin fins consist of vertical cylindrical pins arranged in a staggered configuration with equal lateral and longitudinal spacing. The BCC features four ligaments with circular cross-sections oriented along the diagonals of a cubic domain. The gyroid and diamond structures are defined through implicit trigonometric functions, as proposed by Schwarz [34] and Schoen [35], respectively.

2.1.1. Computational Domains

To minimize the computational cost of the CFD simulations aimed at characterizing the thermo-hydraulic characteristics of the various topologies, the periodic nature of the lattice structures was exploited. Specifically, the computational domain includes only a single unit cell that serves as a representative volume element (RVE). Streamwise periodic boundary conditions were applied under the assumption of fully developed flow. The specific geometry of each structure enables further computational savings. For the pin fin and BCC configurations, vertical and lateral symmetry permits to capture the performance of the entire geometry by simulating only one quarter of the unit cell. The TPMS structures essentially consist of two topologically equivalent but non-connected flow channels. Since both channels exhibit identical hydrodynamic and thermal responses under the same boundary conditions, the computational domain can be limited to a single channel.

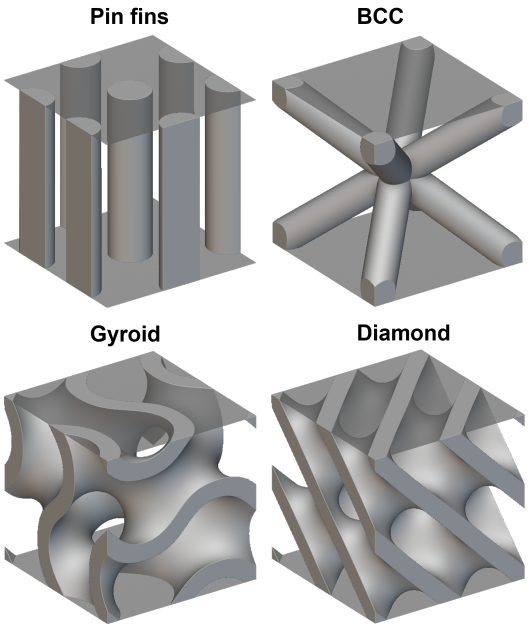

Figure 2: Unit cells of the studied geometries.

The geometry of the various computational domains was generated using the commercial software nTop [36], which is designed for implicit modeling and can generate TPMS structures directly from their mathematical definitions.

2.1.2. Computational Grid

The geometries were meshed using a commercial software [37]. A polyhedral mesh with prismatic inflation layers was used to discretize the computational domains. To determine the appropriate mesh configuration, a mesh sensitivity analysis was performed, examining the influence of both the mesh sizing and the number of prismatic layers on the simulation results. The pin fin geometry was selected for this sensitivity study, conducted at a Reynolds number of 1500. To assess mesh independence and quantify discretization uncertainty, the Grid Convergence Index (GCI) methodology proposed by Roache [38] was used. This approach provides a standardized method to demonstrate grid independence. The GCI method is based on Richardson Extrapolation theory and indicates how much the solution would change with further mesh refinement. A small GCI value confirms that the solution is within the asymptotic range of convergence, providing confidence that the chosen mesh resolution adequately captures

the flow physics with minimal discretization error.

For this study, four meshes were evaluated with a refinement ratio of 1.5, resulting in four grids with approximately 15, 25, 35, and 50 grid elements per hydraulic diameter (Mesh 0, 1, 2, 3, respectively). The results of this analysis are presented in Fig. 3 and Tab. 1.

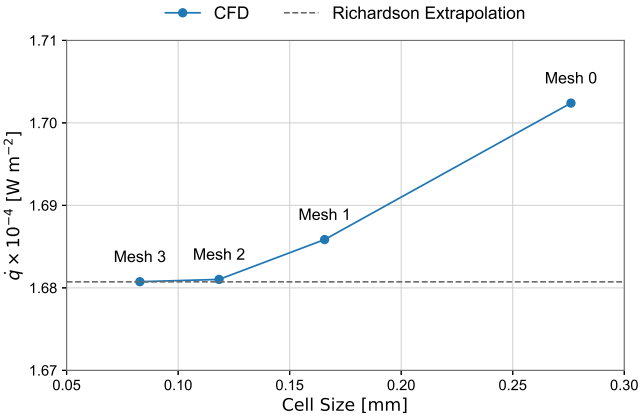

Figure 3: Results of the wall heat flux sensitivity to mesh refinement.

Even the coarsest mesh (Mesh 0) can be considered adequately refined, with a relative deviation from the finest grid of approximately 2.4%. As shown in Tab. 1, the three finer meshes are well within the asymptotic range of convergence, with the highest GCI value being approximately 0.5%. Therefore, further refinements beyond Mesh 1 would significantly increase computational cost with negligible improvement in solution accuracy. Consequently, Mesh 1 was selected for the characterization of all structures.

Table 1: Mesh sensitivity analysis results and grid convergence index.

Mesh	$\mathbf{D_h/\Delta}$ $[-]$	$\dot{\mathbf{q}}$ $[\mathbf{W\,m^{-2}}]$	**GCI** $[\%]$
Mesh 0	15	1.702×10^4	–
Mesh 1	25	1.685×10^4	0.505
Mesh 2	35	1.681×10^4	0.148
Mesh 3	50	1.680×10^4	0.001

Another important mesh parameter is the number of inflation layers, which controls the resolution of the boundary layer region. In the previous analysis, 15 prismatic layers were used for all tested meshes, which is generally considered adequate. To evaluate the sensitivity of the solution to this parameter, different variants of Mesh 1 were tested in which the number of layers was varied between 5, 15, and 25. The results are presented in Fig. 4 and Fig. 2.

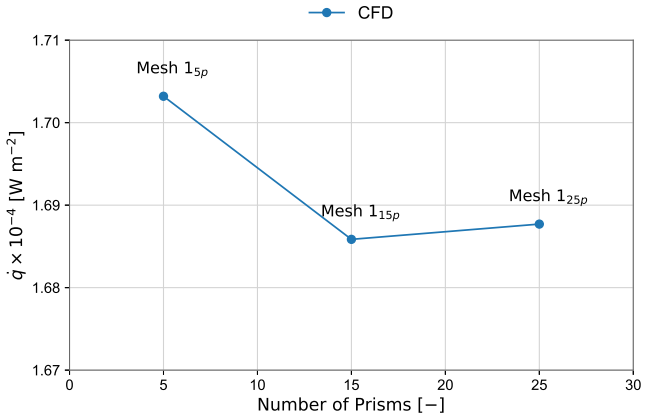

Figure 4: Results of the wall heat flux sensitivity to the number of inflation layers.

The analysis of the results reveals that increasing the number of layers from 5 to 15 leads to a solution deviation of approximately 1%, while a further increase from 15 to 25 layers reduces this deviation to only 0.1%. Based on these findings, Mesh 1 with 15 prismatic layers was selected as it provides the optimal balance between solution accuracy and computational cost.

Table 2: Results of the mesh sensitivity to the number of inflation layers.

Mesh	**Prism Layers [-]**	$\dot{\mathbf{q}}$ $[\mathbf{W\,m^{-2}}]$
Mesh 1_5	5	1.703×10^4
Mesh 1_{15}	15	1.686×10^4
Mesh 1_{25}	25	1.688×10^4

2.1.3. Numerical Setup

All cases were simulated using a commercial solver [37]. As mentioned before, periodic boundary conditions were applied along the streamwise direction, with a user-defined pressure gradient enforcing the desired mass flow rate. For the TPMS structures, periodic boundary conditions were applied in the lateral directions. For the pin fin and BCC structures, symmetry boundary conditions were applied at the two unit cell symmetry planes as well as at the unit cell lateral surface. These settings are applicable under the assumption of fully developed flow and of an infinite lattice matrix. Finally, the top, bottom, and internal surfaces were treated as smooth, no-slip walls., maintained at a constant prescribed wall temperature. An example of the gyroid computational domain and respective boundary conditions is shown in Fig. 5.

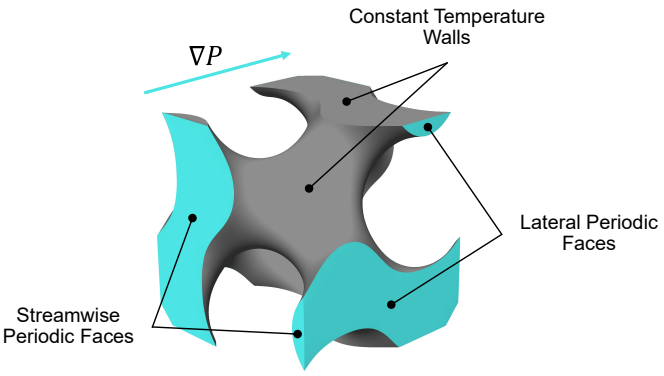

Figure 5: Example of the computational domain and summary of boundary conditions.

The working fluid was assumed to be incompressible, with thermophysical properties (density, viscosity, thermal conductivity, and specific heat) evaluated at the bulk inlet temperature and held constant throughout the domain.

Furthermore, the simulations were conducted using a steady-state, pressure-based solver using the SIMPLE algorithm for pressure-velocity coupling. Besides this, a second-order upwind scheme was used for the spatial discretization in the transport equations. For turbulence modeling, the RANS $k-\omega$ shear stress transport (SST) model was adopted. Literature on turbulent flow in lattice structures, especially in TPMS, shows no clear consensus on the optimal turbulence model, with researchers choosing between $k-\epsilon$ variants (Standard, RNG, Realizable) and $k-\omega$ SST. Yan et al. [20] compared multiple turbulence models across a wide Reynolds numbers range. His study concluded that the $k-\omega$ SST provided the most consistent predictions for both friction factor and Nusselt number, particularly at low Reynolds numbers. Although some $k-\epsilon$ variants offer computational efficiency and handle swirl and separated flows well, the $k-\omega$ SST model is superior for low-Reynolds number flows and complex boundary layers. Additionally, the mesh resolution selected in the sensitivity analysis naturally ensures $y^+ \approx 1$, meeting the near-wall refinement requirements of this model. Therefore, despite its potential to be slightly dissipative in free shear regions, the $k-\omega$ SST model was selected based on its proven accuracy on internal flows and compatibility with the mesh resolution used in this study.

Finally, due to the large number of simulations required for the characterization of the structures, the simulation process was automated using the Python library PyFluent [39].

2.1.4. Computational Model Validation

To assess the reliability of the numerical setup, a validation study was conducted using the pin fin geometry. The pin fin configuration analyzed has a height-to-diameter ratio (H/D) of 4, with both streamwise (X/D) and spanwise (S/D) spacings equal to 2. The predicted friction factors and Nusselt numbers from the simulations were compared with well-established empirical correlations available in the literature.

In particular, the friction factor was compared against empirical correlations derived from experimental data by Metzger [40] and Ostanek [41]. As shown in Fig. 6, the CFD results demonstrate good agreement with Metzger's correlation across the entire Reynolds number range, while a modest deviation from Ostanek's correlation is observed, particularly at lower Reynolds numbers.

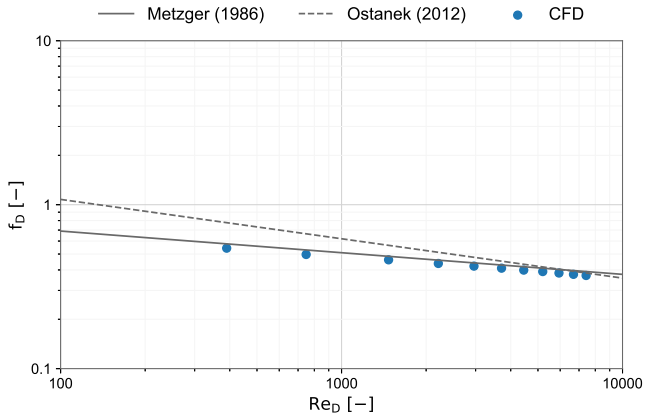

Figure 6: Friction factor predictions estimated from the simulation results against the predictions of empirical correlations from Metzger [40] and Ostanek [41].

The Nusselt number predictions were also compared with the results of the empirical correlations from Metzger [40] and Chyu et al. [42]. As presented in Fig. 7, the CFD model predictions show good agreement with both correlations throughout the Reynolds number range analyzed.

In general, the validation study confirms that the numerical model accurately captures both the friction and heat transfer characteristics of the pin fin configuration. This provides confidence in the reliability of the computational setup and justifies its application to the characterization of the studied subset of structures.

2.1.5. Numerical Dataset

Regardless of the specific geometry analyzed, the simulation domain consisted of a unit cell of 5 mm in all three dimensions. Its porosity varied as a function of

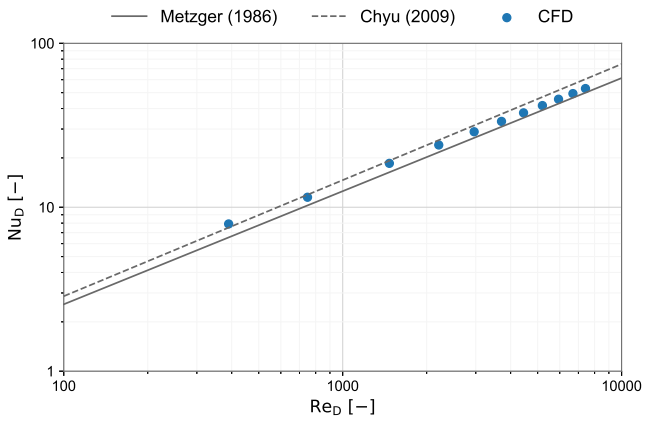

Figure 7: Nusselt number predictions estimated from the simulation results against the predictions of empirical correlations from Metzger [40] and Chyu et al. [42].

the geometry characteristics in a range of 25% to 95%. To evaluate performance across different flow regimes, simulations were conducted over a Reynolds number range spanning from 100 to 100,000. Two working fluids were considered: air and a 50-50% by volume water-ethylene glycol mixture (WEG50-50). This allowed the effect of Prandtl number on heat transfer to be captured throughout all the investigated topologies. The inlet bulk temperature was also varied between 303.15 K and 343.15 K, while the wall temperature was consistently defined as the bulk temperature plus 40 K, thus maintaining a constant temperature difference between the fluid and the wall in all simulation cases. This comprehensive test matrix enabled systematic evaluation of the effects of geometry, flow regime, and fluid properties on the thermo-hydraulic performance of the studied lattice structures.

2.1.6. Post-Processing and Data Reduction

Given the streamwise pressure gradient and the wall temperature as boundary conditions, the primary outputs of the simulations are the mass flow rate, $\dot{m}$, and the wall heat flux, $\dot{q}$. These two quantities, combined with the geometric characteristics of each structure, are sufficient to calculate all the relevant performance parameters.

It is important to calculate the flow and thermal properties to define the reference volume or area being considered. In particular, in this work, a distinction is made between superficial quantities and pore quantities, as commonly done in the field of porous media modeling. The former are defined with respect to the total cross-sectional area of the computational domain, as if the channel were empty, and represent bulk-averaged properties of the medium as observed externally, without considering porosity or internal features. Instead, pore quantities, also referred to as intrinsic or interstitial quantities, are defined with respect to the fluid volume within the porous medium. These quantities describe the local flow conditions within the channel and account for the porosity (ϕ) of the structure, as defined in Eq. 2.1.

$$\phi = \frac{V_\mathrm{f}}{V_\mathrm{total}} \tag{2.1}$$

where V_f and V_total represent the fluid volume and total unit cell volume, respectively.

For example, the superficial velocity is calculated using the total frontal area of the unit cell, A_total, which includes both the solid and fluid regions, as shown in Eq. 2.2.

$$v_s = \frac{\dot{m}}{\rho\, A_\mathrm{in,total}} \tag{2.2}$$

In contrast, the pore velocity accounts for the actual flow area available to the fluid. Since the fluid occupies only the porous fraction of the total area, the fluid frontal area is given by $A_\mathrm{in,f} = \phi A_\mathrm{in,total}$. The pore velocity is therefore defined as shown in Eq. 2.3.

$$v_p = \frac{\dot{m}}{\rho\, A_\mathrm{in,f}} \tag{2.3}$$

This distinction is important because the pore velocity represents the actual velocity experienced by the fluid as it flows through the structure, while the superficial velocity provides a normalized reference based on the overall geometry.

Another important distinction lies in the definition of the hydraulic diameter. For an infinitely wide channel, as for the periodic and symmetry boundary conditions imposed in the unit cell, the superficial hydraulic diameter, $D_{h,s}$, is simply twice the unit cell height, $2H$, representing the hydraulic diameter of an empty channel with the same external dimensions. In contrast, the pore hydraulic diameter, $D_{h,p}$ accounts for the actual geometry within the porous structure and is defined based on the fluid volume and interfacial surface area of the unit cell: $D_{h,p} = 4V_\mathrm{fluid}/A_\mathrm{interface}$. This diameter characterizes the effective local flow passages inside the lattice structures.

To enable a general interpretation of the results independently of specific flow conditions or fluid properties, all thermo-hydraulic quantities were expressed in dimensionless form. The use of dimensionless parameters allows for direct comparison between different geometries and operating conditions, and facilitates the

development of generalized correlations. The key parameters considered in this study are the Reynolds number, friction factor, and Nusselt number.

The Reynolds number is defined as shown in Eq. 2.4.

$$Re = \frac{\rho v D_h}{\mu}, \tag{2.4}$$

Here ρ and μ are the fluid density and dynamic viscosity, respectively, v is the characteristic velocity (either superficial or pore, depending on the definition adopted), and D_h is the corresponding hydraulic diameter.

The Darcy friction factor is obtained from the prescribed streamwise pressure gradient, $\Delta P/L$, as

$$f = \frac{\Delta P}{L} \frac{D_h}{\frac{1}{2}\rho v^2}, \tag{2.5}$$

Additionally, the average convective heat transfer coefficient is defined as

$$h = \frac{\dot{q}}{T_{\text{wall}} - T_{\text{inlet}}}, \tag{2.6}$$

where $\dot{q}$ is the wall heat flux and T_{wall} and T_{inlet} denote the imposed wall and inlet fluid temperatures, respectively.

Finally, the Nusselt number provides a dimensionless measure of convective heat transfer in the unit cell and is computed according to Eq. 2.7.

$$Nu = \frac{h D_h}{\lambda}, \tag{2.7}$$

It is important to note that each of these dimensionless parameters can be defined using either superficial or pore quantities. To distinguish among them the subscripts (s) or (p) are introduced. Accordingly, the superficial definitions (Re_s, f_s, Nu_s) are computed with v_s and $D_{h,s}$, whereas the pore definitions (Re_p, f_p, Nu_p) use v_p and $D_{h,p}$.

2.1.7. Data Regression and Correlation Formulation

One of the objectives of this study is to develop physics-based correlations that describe the thermo-hydraulic performance of each investigated structure. These correlations are intended to capture the effect of the primary geometric parameter, porosity (ϕ), and to remain valid across laminar, transitional, and turbulent flow regimes, as well as across the Prandtl number range representative of typical coolants.

Friction Factor

Analyzing hydraulic performance, based on superficial and pore quantities, it was observed that while the use of pore-based quantities allows for a better scaling of the numerical data, the resulting distribution does not exhibit a consistent correlation applicable across all porosities. In contrast, the superficial definition produces clearer relationships between f_s and Re_s, with a monotonic shift in the curves as porosity varies, as shown in Fig. 8 for the pin fin structure. Therefore, the friction factor correlations were fitted based on the superficial quantities.

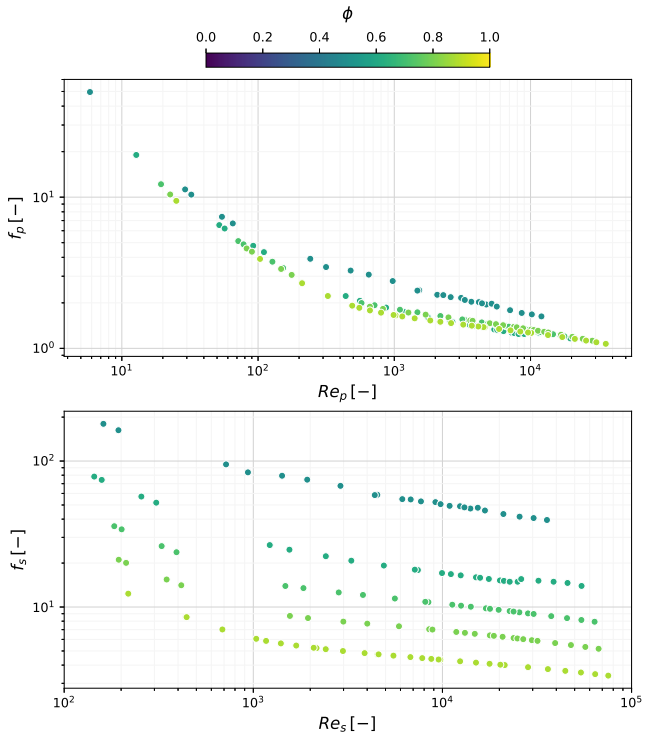

Figure 8: Comparison of the superficial and pore-based friction factor-Reynolds number trends for the pin fin configuration.

The main challenge in formulating a friction factor correlation is to define a mathematical expression that can accurately predict the friction factor across the full range of flow regimes. Many compact heat exchangers operate in the transitional region, where neither purely laminar nor fully turbulent models provide accurate predictions [43]. Therefore, the correlation must ensure a smooth and physically consistent transition between flow regimes. A single, continuous expression is particularly advantageous, as piecewise correlations often exhibit discontinuities and lose predictive accuracy near regime boundaries, which can introduce numerical instability in optimization or system-level analyzes.

Few attempts have been made in the literature to develop correlations for a range of Reynolds numbers as wide as that analyzed in this study ($100 - 100{,}000$). For instance, in pipe flow, the analytical solution $f = 64/Re$ is typically used for the laminar regime, while the Colebrook equation [44] is commonly adopted for turbulent flow. Recognizing the need for a continuous expression, Morrison developed a correlation that spans the entire range of Reynolds numbers, from laminar through transitional to fully turbulent flow [45]. This was accomplished using a sigmoid-type function (see Eq. 2.8) to smoothly transition between the laminar and turbulent regimes.

$$\sigma(x) = \frac{1}{1 + \left(\frac{x}{x_t}\right)^k} \tag{2.8}$$

This function transitions smoothly from 1 to 0, with the parameter k controlling the transition behavior: when $k > 1$, the function exhibits a sharp sigmoid-like transition with a clear inflection point at x_t, while $k < 1$ produces a more gradual decay. The inverse trend, thus from 0 to 1, is obtained using $1 - \sigma(x)$.

Following Morrison's approach, the mathematical properties of the sigmoid function can be leveraged to establish a single friction factor correlation of the form

$$f = \sigma(Re)\, f_{\text{lam}} + (1 - \sigma(Re))\, f_{\text{turb}}, \tag{2.9}$$

where f_{lam} and f_{lam} are the values of the friction factor in the laminar and turbulent regimes, respectively, predicted via two dedicated correlations.

The next step was to identify the mathematical expressions that best fit the data in the two flow regimes for all the structures studied. The use of a consistent formulation for all geometries, facilitates model implementation and its adaption if the lattice structure is changed, and provides indirect evidence that the correlation captures reliably the underlying flow physics.

Starting from the laminar regime, the analytical form $f = A/Re$ was not accurate enough to capture the trends between f_s and Re_s observed for all structures. Better agreement was obtained using Ergun's equation (Eq. 2.10), originally developed to describe pressure losses in packed columns [46]. The Ergun model combines two contributions: a viscous term proportional to $1/Re$ derived from the Kozeny-Carman law for laminar flow through porous media, and an inertial term independent of the Reynolds number, obtained empirically from experimental data at higher Reynolds numbers. By superposing these two asymptotes, Ergun's equation provides a continuous transition between the viscous and inertial flow regimes

$$f_{\text{lam}} = A + \frac{B}{Re} \tag{2.10}$$

This formulation is particularly appropriate for lattice or porous structures, where unsteady flow features and local recirculation appear even at relatively low Reynolds numbers, making the simple analytical $1/Re$ formulation inadequate.

For the turbulent regime, the classical friction factor correlation for smooth pipes and channels, proposed by Blasius [47] and Moody [48], was found to be accurate for all cases studied. This correlation, presented in Eq. 2.11, has also been applied by Hicks [49] for turbulent flows in porous media, supporting its validity for lattice structures.

$$f_{\text{turb}} = \frac{C}{Re^D} \tag{2.11}$$

With the form of the friction correlations established, a significant number of parameters needed to be fitted to the simulation data. Given the complexity of fitting all parameters simultaneously, this process was tackled in three sequential steps using the least squares (LS) method: estimating the optimal value for the coefficients A and B of the correlation for the laminar region, estimating the optimal value of the coefficients C and D for the correlation of the turbulent region, and then fitting the sigmoid function parameters. It is important to note that although Morrison [45] defines the inflection point of the sigmoid function as the Reynolds number at which the transition occurs and indicates it with Re_t, in this work x_t is simply considered as a tuning parameter without direct physical meaning.

This process was repeated for each geometry studied, meaning each porosity of each topology. However, relying on a separate set of correlation parameters for each porosity is impractical for heat exchanger preliminary design. To address this, a general correlation for each structure was developed by expressing the fitted parameters as functions of porosity. This approach yields a friction correlation explicitly defined in terms of both Reynolds number and porosity. Details about the final correlations and additional results are provided in Appendix B.

Figure 9 compares CFD-predicted friction factors with the fitted correlations. The results demonstrate strong agreement, with most data points falling within

$\pm 10\%$ deviation across the investigated Reynolds number and porosity ranges. The accuracy of the fitted correlations is measured by the root mean square error (RMSE) and coefficient of determination R^2, reported in Tab. 3. Overall, the correlations exhibit excellent agreement with the CFD data, with $R^2 > 0.99$ and low root-mean-square errors (RMSE $< 7\%$) across all cases. Among the geometries, the diamond and BCC correlations show the most accurate fits, with the lowest RMSE values and R^2 nearly equal to unity. The gyroid geometry shows slightly higher deviation but remains well within acceptable limits (RMSE $< 7\%$).

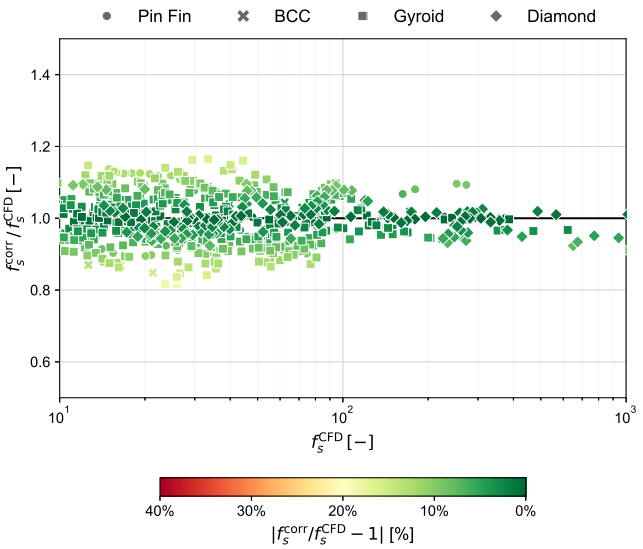

Figure 9: Deviation between the friction factor correlation predictions and CFD simulation results for all four structures.

Table 3: Goodness of fitting for the friction factor correlations.

Geometry	RMSE [%]	$\mathbf{R^2}$ [−]
Pin Fin	6.5	0.9979
BCC	5.6	0.9998
Gyroid	6.9	0.9924
Diamond	4.2	0.9993

Nusselt Number

In contrast to the friction factor results, the heat transfer analysis revealed that using pore-based quantities causes Nusselt number data to collapse onto a single curve for each structure, regardless of porosity. This collapse is illustrated in Fig. 10 for the pin fin structure. This means that a single correlation can be formulated for each studied geometry, with geometrical characteristics such as porosity implicitly included in the pore quantities definition.

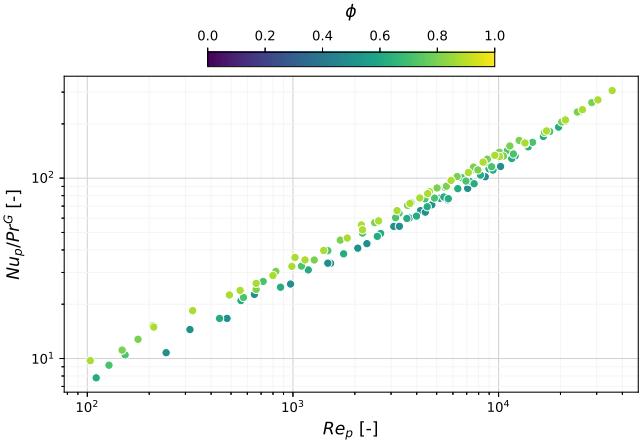

Figure 10: Pore Nusselt number results for the pin fin configuration.

The Dittus-Boelter correlation [50], shown in Eq. 2.12, accurately reproduces the relationship between the Nusselt and Reynolds numbers while accounting for the influence of the fluid through the Prandtl number. Its power-law form is simple, requiring only the fitting of three parameters (E, F, and G).

$$Nu = E Re^F Pr^G \tag{2.12}$$

In their original work on turbulent heat transfer in smooth pipes, Dittus and Boelter proposed different values for the Prandtl number exponent: $G = 0.4$ for heating and $G = 0.3$ for cooling. This distinction reflects the coupling between the momentum and thermal boundary layers when the fluid thermophysical properties vary with temperature. For a fluid being heated, the temperature increases toward the wall, which typically decreases the fluid's viscosity. This lower viscosity near the wall reduces the damping of turbulent fluctuations in the near-wall region, enhancing turbulent mixing and heat transfer. Conversely, for a fluid being cooled, the viscosity increases near the wall, which damps turbulent fluctuations and reduces heat transfer efficiency.

In the present numerical study, all thermophysical properties, including viscosity, are prescribed as constants in space and are independent of temperature. Thus the physical mechanism behind the heating/-cooling case differences, are not captured. Therefore, the distinction between heating and cooling cases becomes irrelevant, and the Prandtl number exponent was treated simply as a fitting parameter.

Finally, the fitting procedure for Nusselt number cor-

relations is simpler, with a single correlation fitted for each structure using the least squares method. Figure 11 compares CFD results for Nusselt number with the predictions of the fitted correlations. The correlation predictions show strong agreement with the CFD simulations, with most data points falling within $\pm 20\%$ deviation. More details on the correlation formulation and additional results can be found in Appendix B.

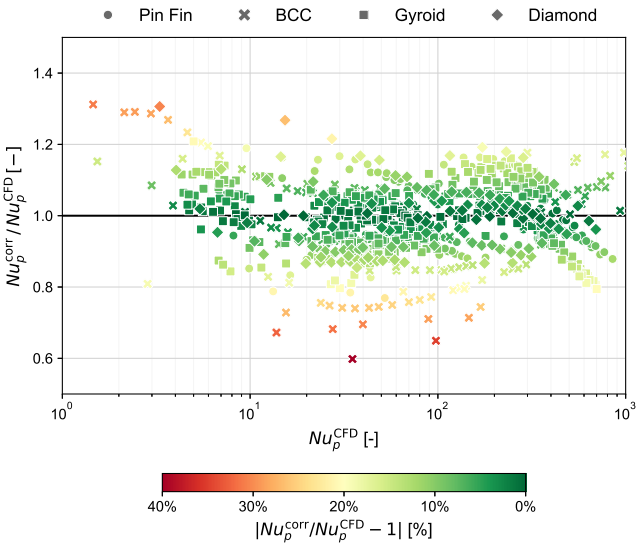

Figure 11: Deviation between the Nusselt number correlation predictions and CFD simulation results for all four structures.

The values of the indicators presented in Tab. 4 indicate a strong agreement between the correlations and the CFD data, with all R^2 values exceeding 0.98 and RMSE values remaining below 13%. The gyroid and diamond geometries show the most accurate fits, with RMSE values around 67%, while the BCC configuration presents the largest deviation, though still within an acceptable range for empirical correlations. Overall, the correlations demonstrate high predictive capability across the different geometries and effectively capture the heat transfer trends over the analyzed flow conditions.

Table 4: Goodness of fitting for the Nusselt number correlations.

Geometry	RMSE [%]	$\mathbf{R^2}$ [–]
Pin Fin	8.0	0.9924
BCC	12.42	0.9897
Gyroid	6.5	0.9952
Diamond	6.9	0.9933

2.2. Component-level Modeling

2.2.1. Cold Plate Modeling

An effective tool for cold plate preliminary design optimization requires a modeling approach that balances physical accuracy with computational efficiency. The model must be capable of rapidly evaluating multiple design configurations while capturing the essential physics governing thermal and hydraulic performance. Additionally, it should seamlessly integrate the detailed correlations derived before.

Thermal Performance

The thermal performance of the cold plate is modeled using the ϵ-NTU method, a heat exchanger reduced-order (HERO) model, which provides a simple yet physically sound framework for heat exchanger analysis. Although the ϵ-NTU method was derived for two-fluid heat exchangers [43], it can be adapted to cold plate configurations through appropriate modeling assumptions.

Copeland [51] proposed an approach that treats the cold plate base as an isothermal surface at temperature T_s^{base}. This assumption implies that the hot-side heat capacity rate becomes infinite ($C_{\max} \to \infty$), resulting in a heat capacity ratio of $C^* = 0$. Under these conditions, $C_{\min}$ corresponds to the working fluid's heat capacity rate, C_f. With this simplification, the effectiveness becomes

$$\epsilon = \frac{\dot{Q}}{\dot{Q}_{\max}} = \frac{C_{\text{f}}(T_{\text{f}}^{\text{in}} - T_{\text{f}}^{\text{out}})}{C_{\min}(T_{\text{s}}^{\text{base}} - T_{\text{f}}^{\text{in}})}, \tag{2.13}$$

Since $C^* = 0$, the ϵ-NTU relationship simplifies to

$$\epsilon = 1 - e^{-NTU}. \tag{2.14}$$

The NTU depends on both the fluid heat capacity rate and the cold plate conductance, UA, which is computed as

$$UA = \left(\frac{t}{\lambda_{\text{s}} A^{\text{base}}} + \frac{1}{\eta_o h A^{\text{interf}}} \right)^{-1}. \tag{2.15}$$

Here, h represents the convective heat transfer coefficient in the cold plate calculated from the Nusselt number correlations, and η_{o} is the overall fin efficiency that accounts for the reduced effectiveness of the finned surfaces. The overall fin efficiency reads

$$\eta_o = 1 - \frac{A^{\text{finned}}}{A^{\text{interf}}}(1 - \eta_{\text{f}}), \tag{2.16}$$

where A_{finned} represents the finned (extended) area and η_{f} the fin efficiency, which is defined as

$$\eta_{\mathrm{f}} = \frac{\tanh\left(mL_{\mathrm{eff}}\right)}{mL_{\mathrm{eff}}}, \quad m = \sqrt{\frac{h\, p_{\mathrm{eff}}}{\lambda_s\, A_{\mathrm{c,\,eff}}}}, \tag{2.17}$$

here, L_{eff} is the effective length of the fin, p_{eff} is the effective fin perimeter, and $A_{\mathrm{c,\,eff}}$ is the effective fin cross-sectional area. The formulation in Eq. 2.15 explicitly incorporates both the conduction resistance through the base plate ($t/\lambda_{\mathrm{s}} A^{\mathrm{base}}$) and the convective resistance at the fluid-solid interface ($1/\eta_{\mathrm{o}} h A^{\mathrm{interf}}$).

Deans et al. [52] proposed an alternative approach that interprets the cold plate as a two-stream cross-flow heat exchanger. In this framework, heat conduction along the fins is treated as a pseudo-fluid stream with an equivalent heat capacity rate, C_{s}, defined based on fin geometry, as shown in Equation 2.18.

$$C_s = \frac{NhP_{\mathrm{eff}}}{m} \frac{\tanh\left(mL_{\mathrm{eff}}\right)}{1 - \dfrac{1}{\cosh\left(mL_{\mathrm{eff}}\right)}} \tag{2.18}$$

where N is the number of fins and h is the heat transfer coefficient.

In contrast to Copeland's methodology, this method yields a non-zero heat capacity ratio, requiring the use of the cross-flow ϵ-NTU relationship for both fluids mixed, namely

$$\epsilon = \frac{1}{\dfrac{1}{1 - e^{(-NTU)}} + \dfrac{C^*}{1 - e^{(-C^*\,NTU)}} - \dfrac{1}{NTU}}, \tag{2.19}$$

to predict the cold plate effectiveness.

Another difference is the calculation of thermal conductance. Since fin efficiency is implicitly incorporated through the solid heat capacity rate, C_{s}, the cold plate conductance reduces to $UA = hA^{interf}$. However, this formulation does not intrinsically capture the temperature variation along the base plate, which was accounted for in Copeland's method through the conduction resistance term. When necessary, this temperature gradient can be computed separately using Fourier's law of conduction.

Both methodologies account for the temperature gradient that develops along the extended surfaces, which reduces the heat transfer effectiveness. However, they employ different strategies to model this effect. Copeland's approach explicitly incorporates the overall surface efficiency, η_o, as a multiplier in the convective thermal resistance. In contrast, Deans' method embeds this effect within the equivalent solid-side heat capacity rate, C_{s}, treating fin conduction as a thermal capacitance effect.

These methods require information about geometric characteristics of the fins, including their effective length, perimeter, and cross-sectional area. While these quantities are straightforward to obtain for strut-based structures such as Pin Fins and BCC lattice, their determination for TPMS geometries presents additional challenges due to their complex topology. For TPMS, the effective fin length is approximated as half the unit cell height, $L_{\mathrm{eff}} = H_{\mathrm{uc}}/2$. The effective perimeter is obtained from the ratio of the total finned area to the height of the unit cell, $P_{\mathrm{eff}} = A^{\mathrm{interf}}/H_{\mathrm{uc}}$. Finally, the effective cross-sectional area is calculated by dividing the solid volume by the unit cell height, $A_{\mathrm{c,\,eff}} = V_{\mathrm{s}}/H_{\mathrm{uc}}$.

Hydraulic Performance

While the preceding analysis addresses the thermal performance of the cold plate, the hydraulic characteristics are equally critical for system design. Pressure losses are computed using the predictions of the fitted empirical correlations through the Darcy-Weisbach friction factor definition (see Eq. 2.9).

2.2.2. Model Implementation

As a proof of concept, the methodology was applied to the design of a cold plate. The selected test case represents a relevant aerospace application for evaluating design methodologies for additively manufactured heat exchangers. The same design problem has been studied by Raske et al. [31], Daifalla et al. [32], and Chiodi et al. [33].

The baseline design has been proposed by a relevant OEM in the aerospace sector, namely, Rolls-Royce. More in detail, the test case consists of a cold-plate heat exchanger used as a heat sink for power electronics. As shown in Fig. 12, the baseline geometry features a multi-pass serpentine channel with 180° U-bends, and both the flow inlet and outlet positioned on the same side. The power electronics are represented by six heating elements or cells, three on each side of the cold plate. Unlike conventional heat exchangers, cold plates must maintain the surface temperature of each heating cell uniform and within the allowable operating range of the power electronics. The 180° U-bends in the serpentine configuration generate high pressure losses providing limited heat transfer enhancement.

In this work, the working fluid is WEG50-50, with an inlet temperature of 333.15 K and a mass flow rate

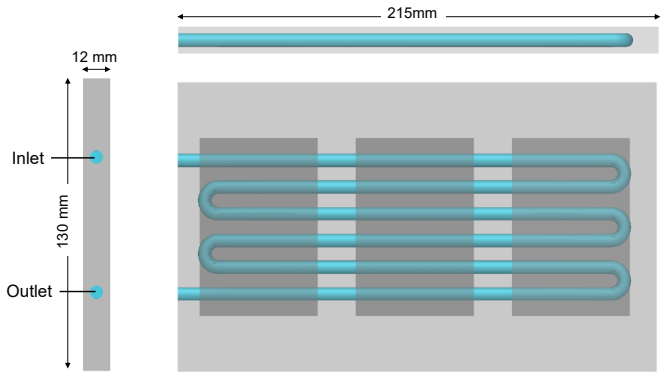

Figure 12: Rolls-Royce cold plate benchmark geometry, adapted from [32].

of $0.05\,kg/s$. Each heating cell generates a heat flux of $94{,}500\,\mathrm{Wm}^{-2}$ and the external walls of the cold plate are assumed to be adiabatic. The cold plate material is characterized by a thermal conductivity of $\lambda_s = 202.4\,\mathrm{Wm}^{-1}\mathrm{K}^{-1}$.

The application of the HERO model to the test case required some specific adaptations. The serpentine channel is replaced by a U-shaped configuration filled with the structures investigated in this study. To promote uniform flow distribution up to the last heating cells, a septum extends along the centerline, covering two-thirds of the cold plate total length. This flow configuration is illustrated schematically in Fig. 13.

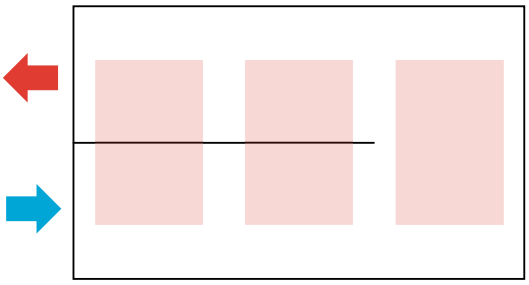

Figure 13: Schematic of the adapted coldplate.

Additionally, since the HERO model is based on the $\epsilon - NTU$ formulation, it assumes unidirectional flow and uniform boundary conditions over each modeled surface. Consequently, it cannot directly represent the flow reversal at the U-turn or the spatially varying heat flux imposed by individual heating cells. To address these limitations, three modeling strategies of increasing complexity were implemented.

In the first one, see Fig. 14, the two branches of the cold plate are concatenated into a single equivalent channel, with the same total heat transfer area but with an overall length double the original one and a width halved with respect to that of the cold plate. This simplification allows the entire device to be represented by a single control volume, assuming uniform heat flux distribution over the external walls. While this approach, indicated as the lumped-parameter approach, provides a computationally efficient way of estimating the average wall temperature and the overall thermal performance of the cold plate, it cannot capture spatial temperature variations.

Figure 14: Lumped-parameter modeling approach: the two branches of the cold plate are represented as a single equivalent straight channel with uniform heat flux.

To capture the thermal gradient along the plate, a second modeling approach was evaluated. This is depicted in Fig. 15, where the cold plate is divided into six consecutive modules, each represented by an independent control volume. The outlet temperature of each module becomes the inlet temperature of the next one, allowing the temperature evolution along the flow path to be captured. Although the uniform heat flux assumption is retained within each module, this strategy , which is referred to as the segmented modeling approach, provides a higher spatial resolution of the temperature difference across the cold plate without significantly increasing model complexity.

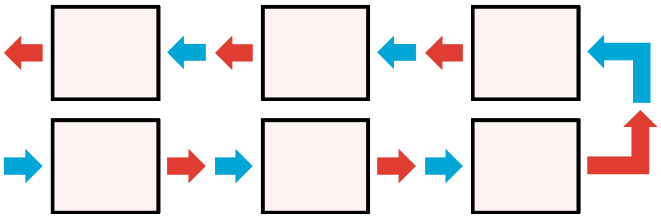

Figure 15: Segmented modeling approach: the cold plate is divided into six modules connected in series.

Finally, the discretized modeling approach (Fig. 16) is based on a discretization scheme that resolves the actual heat flux distribution in the cold plate surface as illustrated in Fig. 16.

However, this higher spatial resolution increases complexity. Furthermore, the heat applied to the top and bottom surfaces does not transfer directly to the working fluid. Instead, it first conducts through the solid on the top and bottom thin end plates, where a portion is redistributed laterally by in-plane conduction. The model thus needs to solve a two-dimensional steady-state heat conduction problem on the end plates.

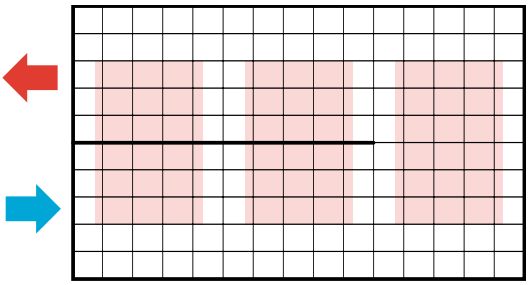

Figure 16: Discretized modeling approach: the cold plate is divided into multiple control volumes.

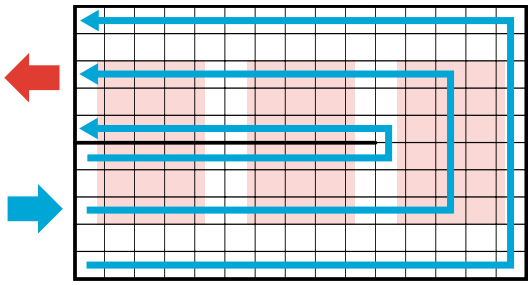

Figure 17: Schematic representation of the concentric U-shaped channels or tubes of flow used in the discretized model.

In principle, this problem could be solved numerically using a finite-volume or finite-element method. However, such an approach would require the iterative solution of a coupling scheme between the fluid and the solid solvers and would be computationally expensive. Assuming steady-state conditions, uniform thermal conductivity and convective heat transfer coefficient, and that the end plate thickness is much smaller than its lateral dimensions, the two-dimensional heat conduction problem on the end plates can be solved efficiently. Applying a Fourier transform to the governing heat conduction equation converts the partial differential equation into an algebraic expression in the spectral domain, as described in [53], significantly reducing computational cost.

Since the heat conduction problem on the end plates depends on the convective heat transfer coefficient, which in turn depends on the local fluid conditions determined by the heat flux distribution, the solution procedure requires an iterative approach. Starting with an initial estimate of the heat transfer coefficient, the conduction problem is solved to obtain the local heat flux distribution. This heat flux is then applied to each control volume, where the $\epsilon - NTU$ method updates the heat transfer coefficient, and the iteration continues until convergence is achieved.

Beyond the thermal coupling between solid conduction and fluid convection, the discretized model must also ensure mass conservation across the network of control volumes. In this regard, it is assumed that the working fluid flows through a set of independent concentric U-shaped channels without cross-communication with the parallel channels, as represented in Fig. 17. Thus, the mass flow rate is conserved along each tube of flow. At the component level, the total mass flow supplied to the inlet manifold equals the total mass flow exiting through the outlet.

The manifolds are treated as plena, regions where static pressure is spatially uniform. Thus, the pressure drop between inlet and outlet must be equal for all channels. To satisfy this constraint, the mass flow rate must distribute among the channels such that pressure losses in each branch are equal. Channels with lower hydraulic resistance (e.g. due to shorter effective length) carry a larger share of the total flow, while those with higher resistance receive proportionally less. The flow distribution is achieved by solving the network continuity equations across the network of control volumes iteratively. The solver adjusts the individual channel mass flow rates until two conditions are met: equal pressure drop across all branches and conservation of the total inlet mass flow rate.

Because the thermal and hydraulic problems are inherently coupled, an outer iteration loop is required to ensure convergence of all field variables. Despite these nested iterations, the computational cost remains moderate due to the analytical nature of the 2D conduction problem solution and the efficiency of the $\epsilon - NTU$ formulation. The number of control volumes was selected based on a grid sensitivity analysis, which showed that further refinement beyond 32 channels (96×64 control volumes) produced less than a 0.1% change in all performance metrics. The details of the discretized model derivation and the results of this grid sensitivity analysis are provided in Appendix C.

Model Verification

Before using it in the case study, the heat exchanger reduced-order (HERO) model was validated against CFD simulations of four TPMS arrays studied by Casini et al. [54]. Two coupons featured Gyroid structures with porosities of 75% and 55%, while the remaining two had Diamond structures with the same porosities. The computational setup is described in detail in Ref. [54]. The computational domain consisted of an array of 5 unit cells with lateral translational periodicity, as shown in Figure 18.

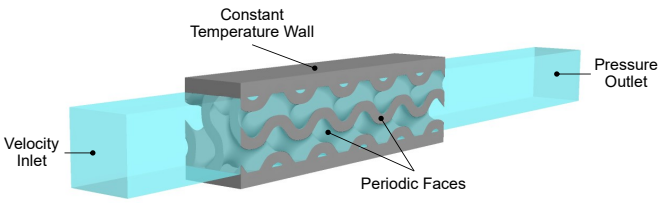

Figure 18: Coupon computational domain and corresponding boundary conditions.

In the verification exercise, whose results are presented in Figure 19, two versions of the HERO model were compared: Copeland's single-stream model (HERO SS) and Deans' two-stream model (HERO TS). Regarding discretization, the lumped-parameter version of the HERO model was adopted since the configuration involves only a 5-unit cell array with a constant temperature boundary condition at the external wall.

For the Gyroid structures, HERO SS underestimated the heat transfer rate by 5.0% at 55% porosity and 1.6% at 75% porosity, while HERO TS showed larger deviations of 9.0% and 10.1%, respectively. For the Diamond structures, the agreement was notably better: HERO SS slightly overpredicted heat transfer by 1.9% at 55% porosity and 3.2% at 75% porosity, while HERO TS remained within 2.4% to 5.9% deviation.

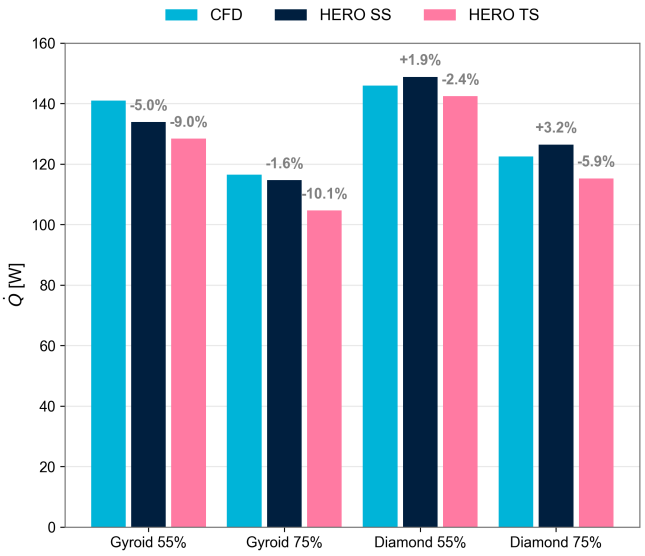

Figure 19: Comparison between CFD and HERO model predictions of heat transfer rate for Gyroid and Diamond coupons at different porosities.

These deviations, all within 10%, can be attributed to several factors. First, the correlations were obtained for a fully periodic domain representing fully developed flow, whereas the CFD computational domain comprised only five unit cells in the streamwise direction. This length is insufficient to render entrance effects negligible, and the developing region exhibits higher heat transfer rates. Consequently, the reduced-order model, based on fully developed flow correlations, would be expected to underpredict the CFD results. This holds true for the two-stream approach; however, the single-stream approach overpredicts the heat transfer rate for the Diamond geometry by a small margin ($<3\%$). This result points to another source of deviation. The correlation regression process itself carries some uncertainty, which, combined with possible numerical uncertainties from the CFD simulations used to generate the synthetic dataset, may be the cause of this slight overprediction.

Overall, although the HERO TS model shows more consistent behavior by underpredicting heat transfer across all geometries, the HERO SS model exhibited substantially lower deviations. Therefore, the single-stream formulation will be adopted for the application to a real system test case and will hereafter be referred to simply as the HERO model.

The verification exercise also included a comparison of the pressure drop predicted by the HERO model against those from the reference CFD simulations. The pressure drop comparison, shown in Figure 20, revealed generally good agreement across all configurations, with relative deviations within $\pm 10\%$. For the Gyroid structures, the HERO model slightly underpredicted the pressure drop by 9.0% at 55% porosity and 6.6% at 75% porosity. For the Diamond structures, the model slightly overpredicted the pressure drop by 4.6% at 55% porosity and underpredicted it by 8.1% at 75% porosity.

Similar to the heat transfer process, the fact that entrance effects are neglected would suggest that the HERO model should underpredict the pressure losses. However, for the Diamond structure at 55% porosity, the HERO model slightly overpredicts the pressure drop. The absence of systematic deviations associated with either geometry or porosity suggests that the observed discrepancies stem from inherent uncertainties in both the correlation formulation and the CFD simulations themselves.

In summary, the HERO model predictions showed reasonable agreement with CFD results across all tested configurations, with pressure drop deviations not exceeding $\pm 9\%$ and heat transfer deviations remaining within $\pm 10\%$. These results indicate that the HERO model can adequately capture both the hydraulic and thermal behavior of heat exchangers fea-

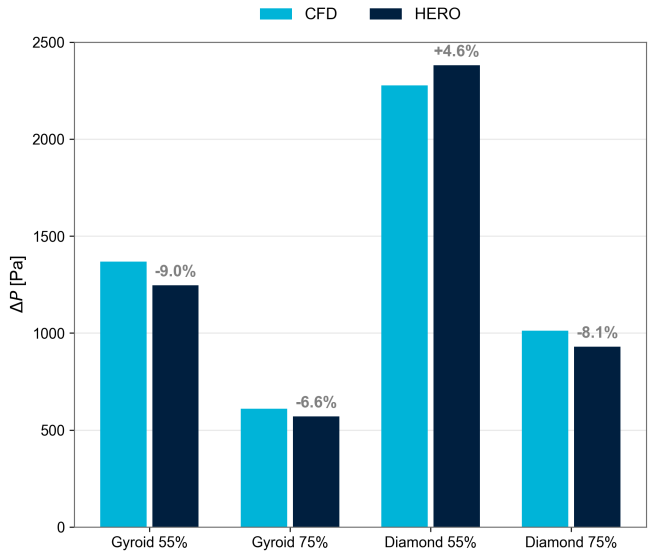

Figure 20: Comparison between CFD and HERO predictions of pressure drop for Gyroid and Diamond coupons at different porosities.

turing lattice structures with considerably lower computational cost than high-fidelity simulations. The observed deviations are consistent with typical limitations of reduced-order formulations, which arise primarily from the homogenization of local flow structures and thermal gradients.

3. Results and Discussion

This section presents, first, the results of a parametric analysis aimed at assessing the thermo-hydraulic performance of each lattice structure for the cold plate design problem; second, the accuracy and computational cost of the cold plate model based on the adopted discretization approach for various lattice structure geometries.

3.1. Component-level Performance of Lattice Structures

To compare the performance of the lattice structures under consideration, hen adopted for the geometry of the internal channels of the cold plate, the porosity of each candidate topology was varied in the range of 0.45 to 0.85, and the resulting cold plate average external wall temperature and pressure drop were analyzed. This porosity range was selected to ensure the manufacturability of all lattice structures while providing sufficient design space to identify the main performance trends. The segmented modeling approach was used for the cold plate model, as it offers a reasonable trade-off between computational efficiency and spatial accuracy.

Figure 21 summarizes the thermo-hydraulic performance of the four lattice structures for the cold plate design. A consistent trend emerges across all geometries: higher porosity reduces pressure drop but also leads to poorer heat transfer and, consequently, higher external wall temperatures, highlighting the inherent trade-off between heat transfer and pumping power.

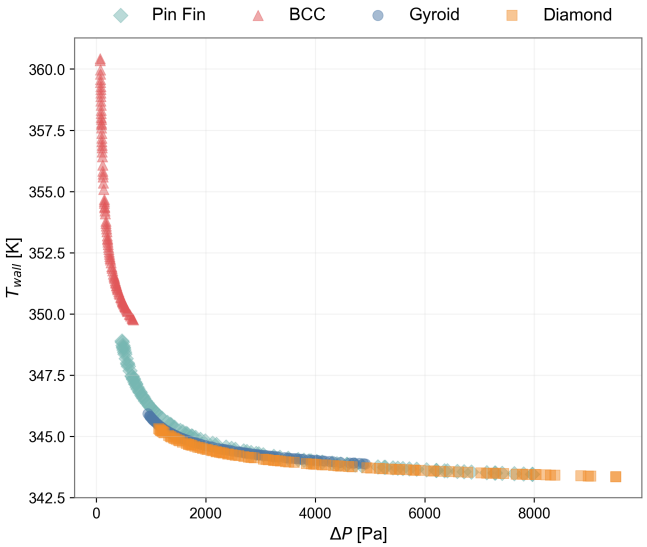

Figure 21: thermo-hydraulic performance map comparing lattice structures across the design space. Each data point represents a simulation at a specific porosity value, with porosity increasing from right to left along each curve.

The BCC structure stands out as as the best solution if minimizing pumping power is the dominant design constraint. However, regardless of the chosen porosity, cold plates with this channel topology feature wall temperatures $3 - 10$ K higher than that achieved with the other design options.

In contrast, TPMS structures demonstrate superior thermal performance, allowing for the lowest wall temperatures. However, this advantage comes at the expense of significantly higher pressure losses. Beyond a certain pressure loss threshold, around $5 - 6$ kPa, the thermal performance approaches an asymptote, and further decreases in porosity produce only marginal thermal improvements despite substantial increases in pressure drop. Within the TPMS family, the gyroid and diamond structures show comparable performance across much of the operating range. While all diamond configurations deliver strong thermal performance, those with lower porosities yield the highest pressure drops observed in this study.

The pin fin structure-based designs occupy an intermediate position between the solutions with TPMS

and BCC lattices, offering favorable thermal performance while requiring substantially lower pressure drops than TPMS-based cold plates.

These performance differences can be attributed to the distinct characteristics of each topology. The BCC structure presents a cross-shaped geometry that forms four triangular channels aligned with the primary flow direction. While the struts do induce turbulence and promote mixing, the relatively large open flow area allows a significant portion of the mass flow to bypass regions of high momentum exchange. This flow characteristic explains both the observed low pressure losses and the reduced heat transfer effectiveness, as the intensity of mixing remains insufficient and the secondary heat transfer surfaces are ineffective.

TPMS structures, by contrast, feature minimal free flow area, forcing the fluid through highly tortuous pathways. This topology intensifies secondary flows that enhance mixing and heat transfer. The improved thermal performance naturally comes with higher pressure penalties due to the increased flow resistance through these channels of complex shape.

The pin fin configurations represents an intermediate solution with its performance strongly dependent on porosity. At higher porosities, the flow experiences minimal deflection around the pins, resulting in performance closer to the BCC lattice. However, as porosity decreases, the flow path becomes progressively more tortuous, leading to increased pressure losses accompanied by enhanced heat transfer. This enhancement arises from two mechanisms: first, the intensification of flow mixing, and second, the increase in available surface area for convective heat transfer.

3.2. Selected Optimal Designs

To identify a single optimal design for each topology, all designs from all structures were combined into a single set to establish a global Pareto front with respect to the design objectives. Each objective value was then normalized to $[0, 1]$ using

$$F^* = \frac{F - F_{\min}^{\text{global}}}{F_{\max}^{\text{global}} - F_{\min}^{\text{global}}}, \tag{3.1}$$

where $F_{\min}^{\text{global}}$ and $F_{\max}^{\text{global}}$ represent the minimum and maximum values across the whole set of solutions. This creates a normalized objective space where $(0, 0)$ represents the ideal performance or utopia point, as this theoretical solution would yield simultaneously the lowest wall temperature and lowest pressure drop found in the dataset. For each topology, the Euclidean distance from each point in the design set to the utopia point was calculated, and the design solution exhibiting the minimum distance was identified as the optimal trade-off for that structure.

This approach implicitly assigns equal weighting to thermal performance and pressure drop. In practice, heat exchanger optimal design strongly depends on application-specific constraints and objectives. Accordingly, a more rigorous approach would require a multi-criteria decision making framework incorporating explicit cost functions or weights defined based on the intended operating conditions. The distance-to-utopia approach adopted here therefore serves only as a an initial comparative metric in the absence of specific application requirements are not defined and the selected geometries should not be regarded as universally optimal.

Figure 22 shows the optimal design selected for each structure in the normalized objective space, and Tab. 5 summarizes the corresponding performance metrics for these designs.

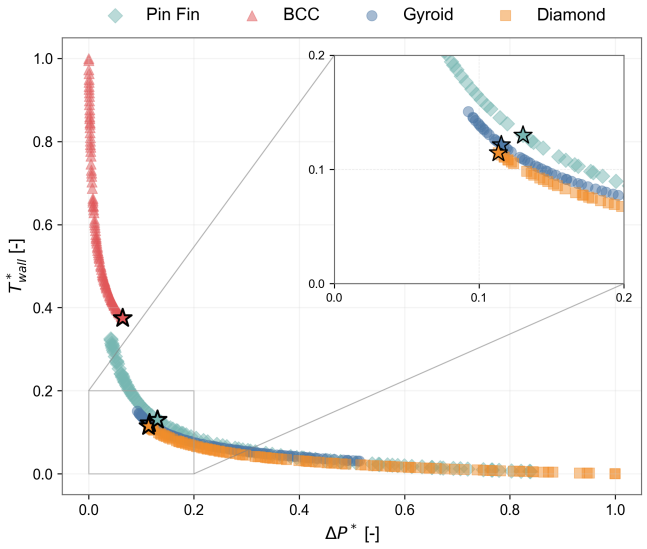

Figure 22: Normalized performance objectives space of the four investigated structures. The starred markers indicate the optimal trade-off point for each structure.

Among the selected optimal designs, the solutions with diamond and gyroid lattices achieve the lowest wall temperatures ($T_{\text{w}} \approx 345\,\text{K}$) with nearly identical pressure drops ($\Delta P \approx 1.1 - 1.2\,\text{kPa}$), demonstrating the superior thermo-hydraulic performance of these topologies. The cold plate with pin fin structures exhibits comparable performance, but requires a slightly higher pressure drop to achieve similar levels of cooling. The selected BCC geometry shows weaker thermal performance despite its moderate pressure drop. Com-

pared to the baseline design (see Fig. 12), all lattice-based designs substantially outperform it, reducing the average wall temperature by $13 - 14K$ as well as the pressure drop by an order of magnitude.

Table 5: Summary of the optimal trade-off designs identified for each structure and comparison with the benchmark serpentine channel.

Geometry	ϕ	$\mathbf{T_w\,[K]}$	$\mathbf{\Delta P\,[Pa]}$
Serpentine	–	359.17	12597
Pin Fin	68%	345.57	1298
BCC	45%	349.76	676
Gyroid	79%	345.43	1157
Diamond	85%	345.30	1138

The optimal designs of the TPMS and pin fin configurations are extremely close to each other, with performance differences within model uncertainty. Therefore, no conclusive ranking can be established among these three structures. Given their comparable performance, these design solutions will be used as test cases to assess the different discretization schemes considered for the HERO model (lumped-parameter, segmented, and discretized), and ultimately to validate the HERO model against high-fidelity numerical simulations.

3.3. Model Validation

The three modeling approaches under consideration for the Hero model differ fundamentally in how they represent the spatial variation of fluid properties and flow distribution within the cold plate. By comparing the predictions obtained with these approaches and also against the results of high-fidelity CFD simulations, this section is aimed at identifying the HERO model implementation that enables a trade-off between computational cost and accuracy suitable for cold plate preliminary design.

3.3.1. Comparison of Modeling Approaches

Table 6 presents the results obtained with the three modeling approaches and the high-fidelity CFD simulations for each of the three optimal cold plate designs. The reported percentage error refers to the deviation of the reduced order model prediction from the corresponding CFD result. The percentage errors for pressure drop are computed using the standard relative definition with respect to the CFD reference, $\mathrm{Error}[\%] = |\Delta P_{\mathrm{HERO}} - \Delta P_{\mathrm{CFD}}|\,/\Delta P_{\mathrm{CFD}} \times 100$. For wall temperature, the error is normalized by the wall-to-inlet temperature difference $\mathrm{Error}[\%] = |T_{\mathrm{w,HERO}} - T_{\mathrm{w,CFD}}|\,/\,(T_{\mathrm{w,CFD}} - T_{\mathrm{in}}) \times 100$, in order to avoid misleadingly small percentage values.

The lumped-parameter approach consistently yields higher values for both average external wall temperature and pressure drop when compared to the more complex approaches. The wall temperature difference is particularly significant, stemming from the model's inability to capture the streamwise evolution of fluid temperature. By evaluating thermophysical properties at inlet temperature and assuming them constant throughout the domain, this approach fails to account for the exponential decrease in fluid viscosity as temperature rises. This viscosity reduction increases the Reynolds number along the flow path, which implies an increase in heat transfer. Since the lumped-parameter model does not capture these phenomena, it systematically underestimates thermal performance. Pressure drop is also overpredicted, though to a lesser extent.

The segmented approach, by dividing the domain into six modules, captures properly the variation in fluid properties as the bulk temperature is updated in each module. The pressure drop estimate also decreases compared to the lumped-parameter model, though more moderately than the wall temperature. This is the result of two competing effects: the decrease in fluid density with temperature increases flow velocity, which would typically raise pressure losses, while the exponential decrease in viscosity reduces friction. The viscosity effect appears dominant, leading to a net reduction in predicted pressure drop.

The discretized approach, despite splitting the domain into several control volumes, produces results generally comparable to those obtained with the segmented model. The modest differences in wall temperature and pressure drop arise primarily from the non-uniform distribution of mass flow rate across parallel channels. Channels located closer to the heat sources exhibit higher mass flow rates, which slightly reduces both local wall temperatures and overall pressure losses compared to the uniform flow distribution assumption inherent in both the segmented and lumped-parameter discretization approaches.

3.3.2. Comparison with CFD Results

The results were validated against full-scale CFD conjugate heat transfer simulations using the setup from Casini et al. [54]. The mesh featured 15 elements per hydraulic diameter, resulting in approximately 80 million cells, consistent with the mesh resolution used by Daifalla et al. [32] for the same test case. Considering this, these high-fidelity simulations came at a

Table 6: Comparison between the results predicted by the Lumped-parameter, Segmented, and Discretized models and the reference CFD simulations for each optimal design. The percentage error refers to the deviation of the reduced order model prediction from the corresponding CFD result.

Pin Fin							
Objective	**Lumped**	**Error [%]**	**Segmented**	**Error [%]**	**Discretized**	**Error [%]**	**CFD**
T_{w} [K]	348.28	28.2%	345.57	5.3%	345.38	3.6%	344.95
ΔP [Pa]	1338	35.7%	1298	31.77%	1214	23.2%	985
Gyroid							
Objective	**Lumped**	**Error [%]**	**Segmented**	**Error [%]**	**Discretized**	**Error [%]**	**CFD**
T_{w} [K]	348.19	31.9%	345.43	7.7%	345.17	5.4%	344.55
ΔP [Pa]	1181	4.5%	1157	2.4%	1114	-1.4%	1130
Diamond							
Objective	**Lumped**	**Error [%]**	**Segmented**	**Error [%]**	**Discretized**	**Error [%]**	**CFD**
T_{w} [K]	348.11	16.6%	345.30	-5.3%	345.21	-6.0%	345.98
ΔP [Pa]	1149	-8.7%	1138	-9.6%	1101	-12.5%	1259

significant computational cost. Beyond the extensive work required for geometry generation and meshing, each simulation required approximately 6 hours to converge on a 196-core cluster. In contrast, the discretized HERO model offers dramatic computational savings: in the same 6-hour window, the reduced-order model can be evaluated 20,000 times.

Across all three geometric configurations, the segmented and discretized formulations demonstrate substantially better agreement with CFD predictions than the lumped approach. While the lumped formulation remains useful for preliminary design screening and qualitative comparisons, its lumped treatment of flow and heat transfer results in the largest deviations from the reference solutions.

The HERO model's accuracy shows clear geometry-dependent patterns. For the Pin Fin configuration, all three approaches predict wall temperatures in close agreement with CFD, with the segmented and discretized models nearly matching the reference value. However, all models significantly overestimate pressure drop ($Error \approx 23\%$ for the discretized approach), suggesting that the Pin Fin geometry is particularly sensitive to local flow effects not captured by the reduced-order model.

Analysis of the velocity contour at the mid-height plane (Fig. 23) reveals the source of this overprediction. In the straight sections, the flow encounters a staggered pin arrangement that forces the fluid to weave through the struts, generating substantial pressure losses. However, during the U-turn region, which comprises roughly one-third of the cold plate, the geometric orientation changes with respect to the incoming flow. The pins that were previously staggered now align to create open flow channels, allowing the fluid to bypass the obstacles with minimal resistance. This flow bypassing effect substantially reduces the actual pressure drop compared to what the HERO model predicts, since it is based on the straight-section flow regime.

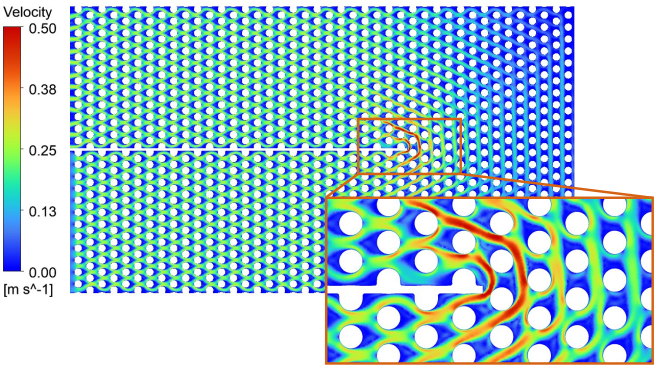

Figure 23: Velocity contour of the pin fin configuration predicted by CFD simulation.

The Hero model estimates for the gyroid-based configuration of the cold plate exhibit excellent agreement with CFD results for both wall temperature and pressure drop with all discretization options. The smooth, continuous flow path characteristic of gyroid structures appear to reduce local flow nonuniformities, making the predictions less sensitive to modeling simplifica-

tions. This inherent flow uniformity allows even the model adopting the segmented approach to achieve high accuracy.

For the diamond configuration, all models slightly underpredict wall temperature, though the deviations remain small. The pressure drop is systematically underpredicted regardless of the discretization approach, suggesting the presence of additional localized losses that are not fully captured by the reduced-order models. In fact, a limitation of the reduced-order model is its failure to account for local losses from inlet and outlet area contraction and expansion, as well as losses associated with flow turning. These considerations are case-specific and can be the subject of future research.

From a practical standpoint, the segmented model represents a good balance between computational complexity and accuracy, making it well-suited for parametric studies that require evaluating hundreds of configurations. However, when more detailed spatial information is needed, such as limiting thermal gradients along the wall, the discretized model becomes particularly valuable, as it provides the resolution necessary to support such design purposes.

As an example, Fig. 24 compares wall temperature distributions predicted by the HERO model against high-fidelity CFD results.

The HERO model predictions show little variation across different cold plate configurations. This is expected, since these designs were selected specifically for their comparable performance. In contrast, the CFD results reveal meaningful differences between geometries. The diamond structure exhibits a higher average wall temperature, as reported in Tab. 6. While gyroids and pin fins show similar temperature distributions overall, pin fins display higher temperatures in the U-bend region due to the fact that pins do not promote enough flow mixing as described earlier.

The comparison reveals that the reduced-order model predicts steeper temperature gradients near the heating zones boundaries on the upper part of the cold plate when compared with the CFD simulation result. This occurs because the model does not account for flow mixing and redistribution after the turn or lateral heat transport between adjacent tubes. Despite this limitation, the HERO model implementing the discretized approach still provides a reliable estimate of the temperature distributions in the cold plate.

3.4. Porosity Field Optimization

Another advantage of the discretized HERO formulation is its ability to accommodate spatially varying lattice properties along the flow path. Unlike uniform-porosity models, the discretized approach can treat porosity as a local design variable. This capability enables a more sophisticated design strategy in which the internal architecture of the cold plate can be spatially

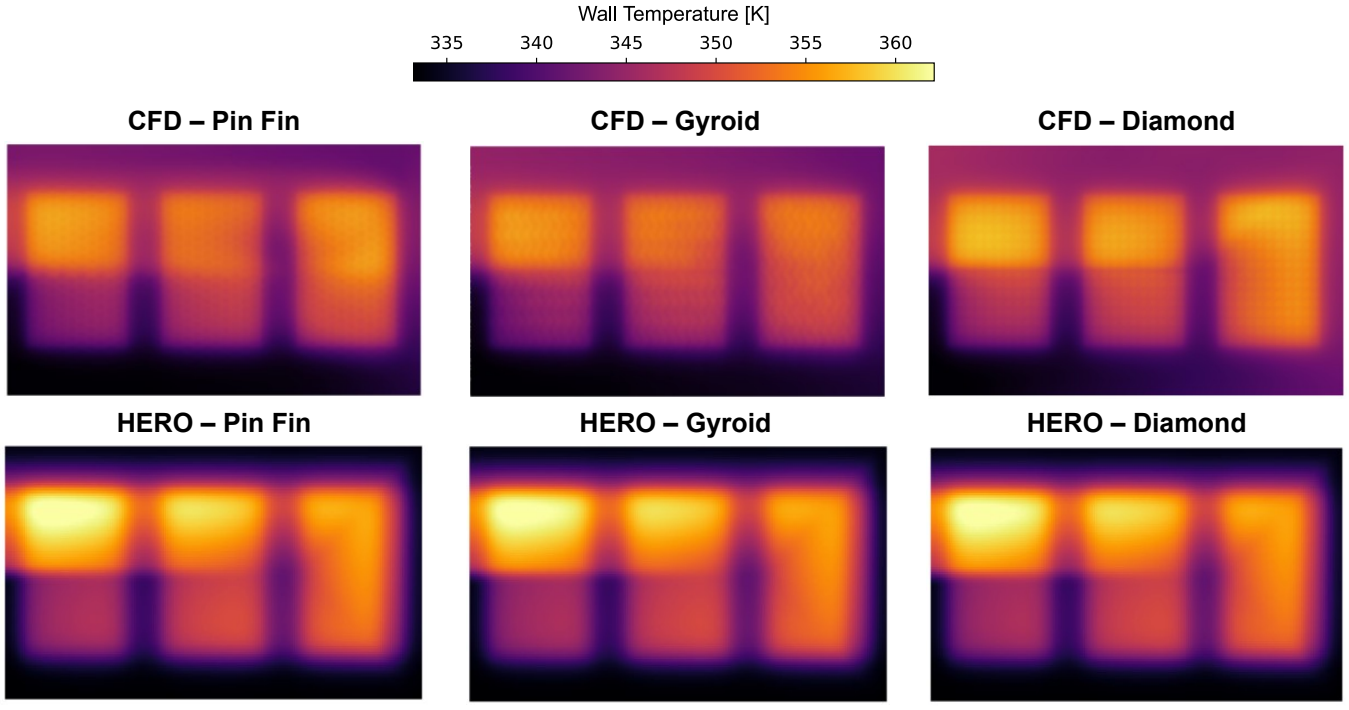

Figure 24: Temperature distribution on the external wall of the cold plate according to the discretized HERO and CFD model predictions.

tuned to address local thermal performance requirements.

As discussed previously, minimizing the average wall temperature alone is insufficient for power electronics cooling. Temperature uniformity is equally critical, making the mitigation of local hot spots a primary design driver. Accordingly, the cold plate design was optimized to spatially redistribute the lattice structure porosity to achieve more uniform wall temperatures for the same pressure drop and average wall temperature of the baseline design.

To allow a smooth spatial variation of porosity, the distribution was parameterized through a reduced set of control points rather than optimizing directly its value in each cell, as illustrated in Fig. 25. Each control point prescribed a local porosity value and the full field was reconstructed through normalized radial basis function (RBF) interpolation. This approach ensured smooth spatial gradients consistent with manufacturability constraints, reduced the dimensionality of the optimization problem, and prevented non-physical checkered patterns that could arise from direct cell-by-cell porosity specification.

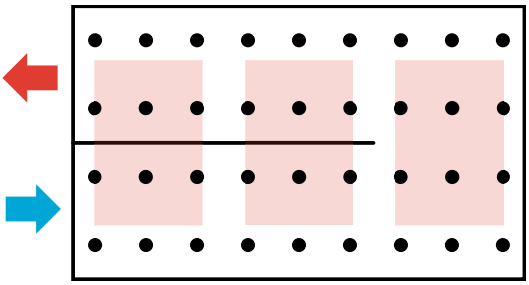

Figure 25: Illustration of the 36 control points parameterization defined for the spatial optimization problem.

The RBF interpolation employed a Gaussian kernel centered at each control point. For a given spatial location (x, y) and a set of M control points located at $\mathbf{c}_i = (c_{x,i}, c_{y,i})$ with associated porosity values ϕ_i, the local porosity field $\phi(x, y)$ was computed as:

$$\phi(x,y) = \frac{\sum_{i=1}^{M} \phi_i \, w_i(x,y)}{\sum_{i=1}^{M} w_i(x,y)}, \tag{3.2}$$

where the weights were defined by Gaussian basis functions:

$$w_i(x,y) = e^{\left[-\frac{1}{2}\left(\left(\frac{x-c_{x,i}}{\sigma_x}\right)^2+\left(\frac{y-c_{y,i}}{\sigma_y}\right)^2\right)\right]}. \tag{3.3}$$

The parameters σ_x and σ_y control the smoothness of the interpolation in the streamwise and transverse directions, respectively, and were set to 75% of the spacing between consecutive control points in each direction. Normalization by the sum of weights ensured that intermediate regions blend smoothly between control point porosity values.

The spatial optimization study is conducted starting from the optimal uniform-porosity gyroid cold plate identified in the preceding design phase, reported in section 3.2. This configuration represents a well-balanced solution in terms of pressure drop and average wall temperature, but still exhibits local high-temperature regions associated with the imposed heat flux distribution and flow path geometry.

The spatial porosity optimization was formulated as a constrained single-objective optimization problem, in which the porosity distribution within the lattice core was treated as the design variable. The objective was to reduce temperature non-uniformities along the cold plate wall, while preserving the global thermo-hydraulic performance achieved by the optimal uniform-porosity reference design.

Let $\boldsymbol{\phi}$ denote the vector of design variables defining the spatial porosity field. For a given porosity distribution, the discretized HERO model provides the corresponding wall temperature field and pressure drop. Considering this, the optimization problem was defined as

$$\begin{aligned}
\min_{\boldsymbol{\phi}} \quad & \Delta T_{\mathrm{w}}(\boldsymbol{\phi}) = T_{\mathrm{w,max}}(\boldsymbol{\phi}) - T_{\mathrm{w,min}}(\boldsymbol{\phi}) \\
\text{subject to} \quad & \frac{\overline{T}_{\mathrm{w}}(\boldsymbol{\phi})}{\overline{T}_{\mathrm{w,ref}}} - 1 \leq 0, \\
& \frac{\Delta P(\boldsymbol{\phi})}{\Delta P_{\mathrm{ref}}} - 1 \leq 0, \\
& 0.45 \leq \phi_i \leq 0.85, \quad i = 1, \ldots, M.
\end{aligned}$$

The objective function minimizes the difference between the maximum and minimum wall temperatures, thereby directly targeting the reduction of local hot spots and improving temperature uniformity across the cold plate.

Two inequality constraints were also introduced to ensure that the optimized design did not degrade the global performance relative to the reference configuration. The first constraint limited the mean wall temperature to values equal to or lower than that of the optimal uniform-porosity gyroid design, while the second constraint enforced an upper bound on the total pressure drop. Finally, porosity values were bounded within a predefined interval $\phi = [0.45, 0.85]$ to ensure structural feasibility and consistency with the validated

correlation ranges.

The constrained optimization problem was solved using a genetic algorithm (GA), selected following the best practices for nonlinear optimization problems with multiple design variables. In the present study, a population size of 200 individuals is adopted, consistent with commonly recommended ranges for maintaining genetic diversity in problems of moderate dimensionality [55, 56]. Convergence was assessed using a combination of objective function tolerance, constraint violation tolerance, and stagnation criteria over successive generations, ensuring that the optimization terminated only once both performance improvement and feasibility had stabilized. The algorithm was implemented using the Python Pymoo optimization library [57].

Figure 26 shows the final optimized porosity field. Porosity decreases significantly in the final section of the flow path in the upper left corner, which corresponds to the hottest region, as shown in Fig. 24. Lower porosity regions also appear at the U-turn corners, reducing coolant flow in the outer regions and redirecting it toward the inner areas where the heat-generating cells are located and the cooling requirements are highest. In contrast, porosity increases in the remaining sections of the cold plate, to maintain the overall pressure losses comparable to that of the uniform-porosity reference design.

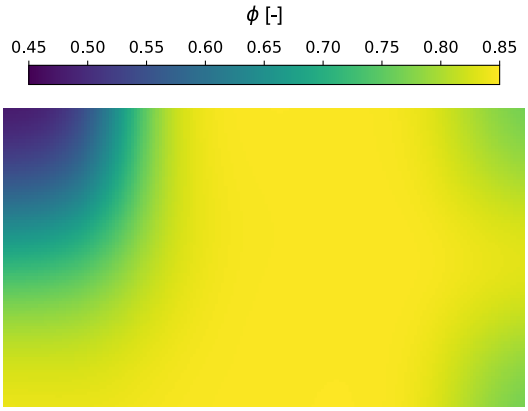

Figure 26: Optimized porosity field.

Table 7 summarizes the key performance indicators for the uniform-porosity reference design and the spatially optimized porosity field.

The results indicate that spatial porosity optimization successfully improved wall temperature uniformity while maintaining a comparable global thermo-hydraulic performance. The maximum wall temperature difference is reduced from 30.27 K in the uniform-porosity configuration to 28.09 K in the optimized design, corresponding to a reduction of approximately 7%. At the same time, the mean wall temperature remains essentially unchanged, increasing by less than 0.3 K relative to the reference case. Similarly, the total pressure drop shows only a marginal increase of approximately 1%, remaining within the imposed constraint and confirming that the redistribution of porosity does not introduce an hydraulic penalty.

Table 7: Comparison of global performance metrics between the uniform-porosity reference design and the spatially optimized porosity field.

KPI	Reference	Optimized
ΔP [Pa]	1114	1125
T_{w} [K]	345.17	345.44
$\Delta T_{\max}$ [K]	30.27	28.09

The improvement in temperature uniformity observed in Fig. 27, is achieved through a spatial redistribution of porosity: regions prone to elevated wall temperatures benefit from locally reduced porosity, enhancing heat transfer effectiveness, while compensatory increases in porosity elsewhere preserve the global pressure drop. The porosity reduction at the U-turn corners is intended to reduce flow in the outer regions, thereby redirecting a greater portion of the coolant toward the inner sections where the heat-generating cells are positioned. The net result is an improvement of heat transfer where it is most needed.

From a design perspective, these results demonstrate that spatial porosity optimization offers clear advantages for applications where temperature uniformity is critical, such as power electronics cooling. The ability to redistribute heat transfer capability without increasing pressure drop highlights the value of treating porosity as a spatially variable design parameter. More generally, this result illustrates how the adoption of a model based on a fine discretization of the heat transfer geometry, such as the HERO model, enables design solutions that cannot be achieved using conventional lumped-parameter models or by adopting the same geometric patterns throughout the heat transfer device.

4. Conclusion

The research work focused on the thermo-hydraulic characterization of novel lattice structures as heat transfer surfaces and the subsequent implementation of the derived performance correlations into a reduced-order model that enables rapid analysis and design optimization of thermal management components. As

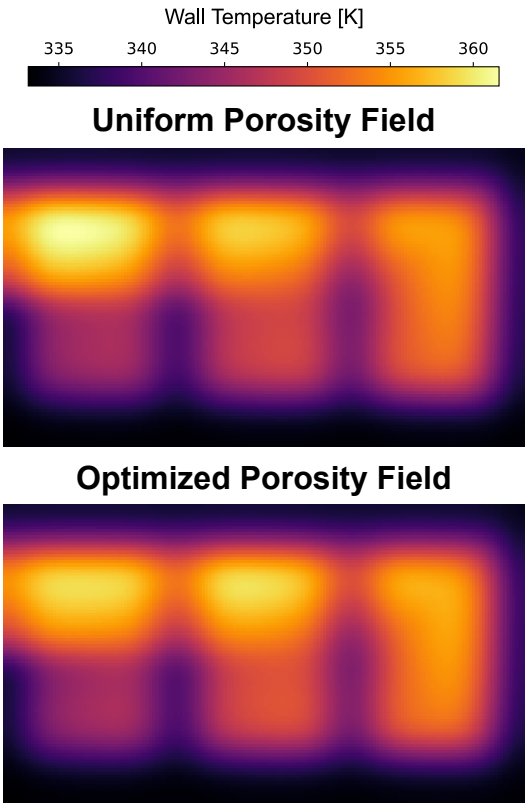

Figure 27: Comparison of wall temperature distribution on the external wall of the cold plate for the uniform-porosity and optimized designs.

a proof of concept, the proposed methodology was applied to a cold plate test case to identify optimal cold plate geometries targeting two competing objectives: maximizing thermal effectiveness while minimizing pressure losses. The main findings can be summarized as follows.

1. The predictions of friction factor and Nusselt number obtained with the derived correlations fall within deviations of $\leq$10% and $\leq$15%, respectively, with respect to the CFD simulations results used for the fitting.
2. The comparison of different discretization approaches reveals that the assumption of constant properties across the cold plate typical of the lumped-parameter modeling approach leads to inaccuracies, particularly in predicting thermal effectiveness. In contrast, the segmented and discretized versions of the model showed comparable and more accurate results.
3. The reduced-order model predictions demonstrated close agreement with the results of the full-scale CFD simulations, while requiring only a fraction of the computational cost. However, a limitation of the methodology was identified. It does not predict anisotropic flow effects, since its models are built upon the assumption of isotropic periodic structures.
4. Using a finely discretized representation of the heat transfer device proved particularly beneficial for optimizing the spatial distribution of porosity. The optimization algorithm strategically reduced porosity in high-temperature regions where thermal demands were most critical, while simultaneously increasing porosity in regions where cooling requirements were less stringent, in order to maintain pressure losses below the prescribed constraint.

Future work will expand the characterization to include geometric inputs beyond porosity and explore additional topologies to broaden the design space of additively manufactured heat transfer devices. Furthermore, experimental validation of the correlations would enhance their reliability and, therefore, increase confidence in the preliminary design tool.

References

[1] *Non-CO2 Emissions and Effects*. IATA. URL: https://www.iata.org/contentassets/726b8a2559ad48fe9decb6f2534549a6/non-co2-emissions-and-effects.pdf (visited on 09/29/2025).

[2] H. Ritchie. "What share of global CO emissions come from aviation?" In: *Our World in Data* (2024). URL: https://ourworldindata.org/global-aviation-emissions (visited on 09/29/2025).

[3] *Non-CO2 Aviation Emissions*. IATA. URL: https://www.iata.org/contentassets/5499da2b3b7d46b3b13be4dad54a9689/policy-position-non-co2-aviation-emissions.pdf (visited on 09/29/2025).

[4] R.G. Sanchez and T.K. Walker III. "Aviation Non-CO_2 Effects - Strategies for Minimizing Contrail Climate Impact". In: *Clean Air Task Force* (2025). URL: https://www.catf.us/resource/aviation-non-co2-effects-strategies-for-minimizing-contrail-climate-impact/.

[5] *Paris Agreement*. UNFCCC. URL: https://unfccc.int/process-and-meetings/the-paris-agreement (visited on 09/29/2025).

[6] S.L. Schnulo et al. "Assessment of the Impact of an Advanced Power System on a Turboelectric

Single-Aisle Concept Aircraft". In: *AIAA Propulsion and Energy 2020 Forum*. American Institute of Aeronautics and Astronautics, Aug. 2020. ISBN: 978-1-62410-602-6. DOI: 10.2514/6.2020-3548.

[7] C. Lents et al. "Parallel Hybrid Gas-Electric Geared Turbofan Engine Conceptual Design and Benefits Analysis". In: July 2016. DOI: 10.2514/6.2016-4610.

[8] K.A. Thole, S.P. Lynch, and A.J. Wildgoose. "Review of advances in convective heat transfer developed through additive manufacturing". In: vol. 53. Advances in Heat Transfer. Elsevier, 2021, pp. 249–325. DOI: https://doi.org/10.1016/bs.aiht.2021.06.004.

[9] C. Pan, Y. Han, and J. Lu. "Design and Optimization of Lattice Structures: A Review". In: *Applied Sciences* 10.18, 6374 (Sept. 2020). ISSN: 2076-3417. DOI: 10.3390/app10186374.

[10] I. Kaur and P. Singh. "Effects of inherent surface roughness of additively manufactured lattice frame material on flow and thermal transport". In: *International Journal of Heat and Mass Transfer* 209, 124077 (Aug. 2023). ISSN: 00179310. DOI: 10.1016/j.ijheatmasstransfer.2023.124077.

[11] N. Castelli et al. "Experimental Analysis of Additive Manufactured Latticework Coupons". In: Boston, Massachusetts, USA: American Society of Mechanical Engineers, June 2023, V07BT13A010. ISBN: 978-0-7918-8701-1. DOI: 10.1115/GT2023-102445.

[12] T.M. Corbett and K.A. Thole. "Large eddy simulations of kagome and body centered cubic lattice cells". In: *International Journal of Heat and Mass Transfer* 218, 124808 (Jan. 2024). ISSN: 00179310. DOI: 10.1016/j.ijheatmasstransfer.2023.124808.

[13] D. Liang et al. "Investigating the effect of element shape of the face-centered cubic lattice structure on the flow and endwall heat transfer characteristics in a rectangular channel". In: *International Journal of Heat and Mass Transfer* 153, 119579 (June 2020). ISSN: 00179310. DOI: 10.1016/j.ijheatmasstransfer.2020.119579.

[14] A. Lorenzon et al. "Experimental investigation of heat transfer and pressure losses across staggered Body Centered cubic arrays fabricated by Laser Powder Bed Fusion". In: *Applied Thermal Engineering* 227, 120381 (2023). ISSN: 1359-4311. DOI: https://doi.org/10.1016/j.applthermaleng.2023.120381.

[15] S.S. Rathore et al. "Flow Characterization in Triply Periodic Minimal Surface (TPMS)-Based Porous Geometries: Part 1Hydrodynamics". In: *Transport in Porous Media* 146.3 (Feb. 2023), pp. 669–701. ISSN: 0169-3913, 1573-1634. DOI: 10.1007/s11242-022-01880-7.

[16] S. Piedra, A. Gómez-Ortega, and J. Pérez-Barrera. *Characterizing Flow Through Tpms Structures Using Darcy-Forchheimer Model*. 2023. DOI: 10.2139/ssrn.4470062.

[17] L.G. Ornelas-Ramón et al. "Computational analysis and engineering modeling for the heat transfer and fluid flow through the gyroid TPMS structure". In: *Applied Thermal Engineering* 268, 125865 (June 2025). ISSN: 13594311. DOI: 10.1016/j.applthermaleng.2025.125865.

[18] S.S. Rathore et al. *Flow Characterization in Triply-Periodic-Minimal-Surface (TPMS) based Porous Geometries: Part 2 Heat Transfer*. Jan. 2023. DOI: 10.21203/rs.3.rs-2427715/v1.

[19] F. Torri et al. "Evaluation of TPMS Structures for the Design of High Performance Heat Exchangers". In: Capri, Italy, Aug. 2023, 2023-24-0125. DOI: 10.4271/2023-24-0125.

[20] K. Yan et al. *Numerical Investigation into Thermal and Hydraulic Characteristics of Triply Periodic Minimal Surface-Based Heat Exchangers*. 2023. DOI: 10.2139/ssrn.4336822.

[21] S. Samson, P. Tran, and P. Marzocca. "Design and modelling of porous gyroid heatsinks: Influences of cell size, porosity and material variation". In: *Applied Thermal Engineering* 235, 121296 (Nov. 2023). ISSN: 13594311. DOI: 10.1016/j.applthermaleng.2023.121296.

[22] J. Wang et al. "Investigation on flow and heat transfer in various channels based on triply periodic minimal surfaces (TPMS)". In: *Energy Conversion and Management* 283, 116955 (May 2023). ISSN: 01968904. DOI: 10.1016/j.enconman.2023.116955.

[23] G. Brambati, M. Guilizzoni, and S. Foletti. "Convective heat transfer correlations for Triply Periodic Minimal Surfaces based heat exchangers". In: *Applied Thermal Engineering* 242, 122492 (Apr. 2024). ISSN: 13594311. DOI: 10.1016/j.applthermaleng.2024.122492.

[24] B.W. Reynolds et al. "Characterisation of Heat Transfer within 3D Printed TPMS Heat Exchangers". In: *International Journal of Heat and Mass Transfer* 212, 124264 (Sept. 2023). ISSN: 00179310. DOI: 10.1016/j.ijheatmasstransfer.2023.124264.

[25] W. Tang et al. "Analysis on the convective heat transfer process and performance evaluation of Triply Periodic Minimal Surface (TPMS) based on Diamond, Gyroid and Iwp". In: *International Journal of Heat and Mass Transfer* 201, 123642 (Feb. 2022). ISSN: 00179310. DOI: 10.1016/j.ijheatmasstransfer.2022.123642.

[26] W. Tang et al. *Experimental Investigation on the Convective Heat Transfer Performance of Five Triply Periodic Minimal Surfaces (Tpms): Gyroid, Diamond, Iwp, Primitive, and Fischer-Koch-S*. 2023. DOI: 10.2139/ssrn.4648952.

[27] Z. Zou et al. "Experimental investigation of the performance of an Industrial-Grade Schwartz-D heat exchanger". In: *Applied Thermal Engineering* 270, 126243 (July 2025). ISSN: 13594311. DOI: 10.1016/j.applthermaleng.2025.126243.

[28] A.G. Caket et al. "Recent studies on 3D lattice metal frame technique for enhancement of heat transfer: Discovering trends and reasons". In: *Renewable and Sustainable Energy Reviews* 167, 112697 (Oct. 2022). ISSN: 13640321. DOI: 10.1016/j.rser.2022.112697.

[29] R. V. Rao et al. "Design Optimization of Heat Exchangers with Advanced Optimization Techniques: A Review". In: *Archives of Computational Methods in Engineering* 27.2 (2020), pp. 517–548. DOI: 10.1007/s11831-019-09318-y.

[30] K. Yeranee et al. "Thermal Performance Enhancement for Gas Turbine Blade Trailing Edge Cooling with Topology-Optimized Printable Diamond TPMS Lattice". In: *International Journal of Heat and Fluid Flow* 110, 109649 (2024). ISSN: 0142-727X. DOI: 10.1016/j.ijheatfluidflow.2024.109649.

[31] N. Raske et al. "Thermal Management for Electrification in Aircraft Engines: Optimization of Coolant System". In: vol. Volume 6B: Heat Transfer General Interest/Additive Manufacturing Impacts on Heat Transfer; Internal Air Systems; Internal Cooling. Turbo Expo. June 2022, V06BT13A013. DOI: 10.1115/GT2022-82538.

[32] E. Daifalla et al. "Multi-Disciplinary Optimization of Gyroid Topologies for a Cold Plate Heat Exchanger Design". In: vol. Volume 13: Heat Transfer: General Interest / Additive Manufacturing Impacts on Heat Transfer; Wind Energy. Turbo Expo. June 2024, V013T13A038. DOI: 10.1115/GT2024-128603.

[33] A. Chiodi et al. "Multidisciplinary Optimisation of Additive Manufactured Heat Exchangers for Aeronautical Applications". In: vol. Volume 13: Heat Transfer: General Interest / Additive Manufacturing Impacts on Heat Transfer; Wind Energy. Turbo Expo. June 2024, V013T13A026. DOI: 10.1115/GT2024-126786.

[34] H.A. Schwarz. *Gesammelte Mathematische Abhandlungen. Erster Band*. 1st ed. Berlin, Heidelberg: Springer-Verlag Berlin Heidelberg, 1890. DOI: 10.1007/978-3-642-50665-9.

[35] A.H. Schoen. *Infinite Periodic Minimal Surfaces without Self-Intersections*. NASA Technical Note NASA-TN-D-5541. Cambridge, MA, United States: NASA Electronics Research Center, May 1970. URL: https://ntrs.nasa.gov/citations/19700020472.

[36] *nTop*. Version 5. nTop Inc. 2025. URL: https://ntop.com.

[37] *Fluent Theory Guide*. Version 2023 R2. ANSYS, Inc. Canonsburg, PA, 2023. URL: https://www.ansys.com/products/fluids/ansys-fluent.

[38] P. J. Roache. "Perspective: A Method for Uniform Reporting of Grid Refinement Studies". In: *Journal of Fluids Engineering* 116.3 (Sept. 1994), pp. 405–413. ISSN: 0098-2202. DOI: 10.1115/1.2910291.

[39] *PyFluent documentation*. Version 0.35.1. PyAnsys. 2025. URL: https://fluent.docs.pyansys.com/.

[40] D. E. Metzger, W. B. Shepard, and S. W. Haley. "Row Resolved Heat Transfer Variations in Pin-Fin Arrays Including Effects of Non-Uniform Arrays and Flow Convergence". In: *Proceedings of the 31st ASME International Gas Turbine Conference and Exhibit*. ASME. Duesseldorf, West Germany, June 1986, p. 9.

[41] J. Ostanek. "Flowfield and Heat Transfer Measurements in Staggered Pin-Fin Arrays". Doctor of Philosophy Dissertation. University Park, PA, USA: The Pennsylvania State University, Mar. 2012.

[42] M. Chyu, S. Siw, and H. Moon. "Effects of Height-to-Diameter Ratio of Pin Element on Heat Transfer From Staggered Pin-Fin Arrays". In: vol. 3. Jan. 2009. DOI: 10.1115/GT2009-59814.

[43] W.M. Kays and A.L. London. *Compact heat exchangers*. McGraw-Hill,New York, NY, Dec. 1983.

[44] C. F. Colebrook and C. M. White. "Experiments with fluid friction in roughened pipes". In: *Proc. R. Soc. Lond.* 161 (Aug. 1937), pp. 367–387. DOI: 10.1098/rspa.1937.0150.

[45] F.A. Morrison. "Data Correlation for Friction Factor in Smooth Pipes". URL: https://pages.mtu.edu/~fmorriso/DataCorrelationForSmoothPipes2013.pdf (visited on 09/05/2025).

[46] S. Ergun. "Fluid Flow Through Packed Columns". In: *Chemical Engineering Progress* 48.2 (1952), p. 89. URL: https://cir.nii.ac.jp/crid/1572261550410403712.

[47] H. Blasius. "Das Aehnlichkeitsgesetz bei Reibungsvorgängen in Flüssigkeiten". In: *Mitteilungen über Forschungsarbeiten auf dem Gebiete des Ingenieurwesens: insbesondere aus den Laboratorien der technischen Hochschulen*. Berlin, Heidelberg: Springer Berlin Heidelberg, 1913, pp. 1–41. ISBN: 978-3-662-02239-9. DOI: 10.1007/978-3-662-02239-9_1.

[48] L.F. Moody. "Friction Factors for Pipe Flow". In: *Transactions of the American Society of Mechanical Engineers* 66.8 (Dec. 2022), pp. 671–678. ISSN: 0097-6822. DOI: 10.1115/1.4018140.

[49] R. E. Hicks. "Pressure Drop in Packed Beds of Spheres". In: *Industrial & Engineering Chemistry Fundamentals* 9.3 (1970), pp. 500–502. DOI: 10.1021/i160035a020.

[50] F. W. Dittus and L.M.K. Boelter. "Heat Transfer in Automobile Radiators of the Tubular Type". In: *Publications in Engineering* 2 (1930), p. 443.

[51] D.W. Copeland. "Fundamental Performance Limits of Heatsinks". In: *Journal of Electronic Packaging* 125.2 (June 2003), pp. 221–225. ISSN: 1043-7398. DOI: 10.1115/1.1569262. URL: https://doi.org/10.1115/1.1569262.

[52] J. Deans et al. "The Use of Effectiveness Concepts to Calculate the Thermal Resistance of Parallel Plate Heat Sinks". In: *Heat Transfer Engineering* 27.5 (June 2006), pp. 56–67. ISSN: 0145-7632, 1521-0537. DOI: 10.1080/01457630600560643.

[53] K. Sankaranarayanan et al. "Architectural implications of spatial thermal filtering". In: *Integration* 46.1 (2013), pp. 44–56. ISSN: 0167-9260. DOI: https://doi.org/10.1016/j.vlsi.2011.12.002.

[54] N. Casini, L. Mazzei, and R. Da Soghe. "Numerical Analysis of Convective Heat Transfer Processes and Performance Assessment of Lattice and Triply Periodic Minimal Surface Geometries". In: vol. Volume 13: Heat Transfer: General Interest / Additive Manufacturing Impacts on Heat Transfer; Wind Energy. Turbo Expo. June 2024, V013T13A041. DOI: 10.1115/GT2024-129097.

[55] D. Rani et al. "Genetic Algorithms and Their Applications to Water Resources Systems". In: *Metaheuristics in Water, Geotechnical and Transport Engineering*. Elsevier, 2013, pp. 43–78. DOI: 10.1016/B978-0-12-398296-4.00003-9.

[56] A. Hassanat et al. "Choosing Mutation and Crossover Ratios for Genetic Algorithms-A Review with a New Dynamic Approach". In: *Information* 10.12, 390 (2019). DOI: 10.3390/info10120390.

[57] J. Blank and K. Deb. "pymoo: Multi-Objective Optimization in Python". In: *IEEE Access* 8 (2020), pp. 89497–89509.

[58] R.K. Shah and D.P. Sekuli. *Fundamentals of Heat Exchanger Design*. Hoboken, NJ, USA: John Wiley & Sons, Inc., 2003. ISBN: 9780471321712. DOI: 10 . 1002 / 9780470172605. URL: https://doi.org/10.1002/9780470172605.

[59] S. Kakaç, H. Liu, and A. Pramuanjaroenkij. *Heat Exchangers: Selection, Rating, and Thermal Design*. 4th ed. CRC Press, 2020. DOI: 10.1201/9780429469862.

[60] V. Gnielinski. "New equations for heat and mass transfer in the turbulent flow in pipes and channels". In: *NASA STI/Recon Technical Report A* 41.1 (Jan. 1975), pp. 8–16.

[61] R.M. Manglik and A.E. Bergles. "Heat transfer and pressure drop correlations for the rectangular offset strip fin compact heat exchanger". In: *Experimental Thermal and Fluid Science* 10.2 (1995). Aerospace Heat Exchanger Technology, pp. 171–180. ISSN: 0894-1777. DOI: https://doi.org/10.1016/0894-1777(94)00096-Q.

[62] I. Kaur et al. "Thermal-hydraulic performance of additively manufactured lattices for gas turbine blade trailing edge cooling". In: *Applied Thermal Engineering* 211, 118461 (July 2022). ISSN: 13594311. DOI: 10.1016/j.applthermaleng.2022.118461.

[63] E.R. Neovius. *Bestimmung zweier speciellen periodischen Minimalflächen*. Helsingfors, 1883.

[64] T. Femmer, A.J.C. Kuehne, and M. Wessling. "Estimation of the structure dependent performance of 3-D rapid prototyped membranes". In: *Chemical Engineering Journal* 273 (Aug. 2015), pp. 438–445. ISSN: 13858947. DOI: 10.1016/j.cej.2015.03.029.

[65] VDI e. V., ed. *VDI Heat Atlas*. 2nd ed. VDI-Buch. Springer Berlin, Heidelberg, 2010. ISBN: 978-3-540-77877-6. DOI: 10.1007/978-3-540-77877-6.

[66] H.A. Navarro and L.C. Cabezas-Gómez. "Effectiveness-ntu computation with a mathematical model for cross-flow heat exchangers". In: *Brazilian Journal of Chemical Engineering* 24.4 (Dec. 2007), pp. 509–521. ISSN: 0104-6632. DOI: 10.1590/S0104-66322007000400005.

[67] A. Ortega et al. "Determination of the Thermal Performance Limits for Single Phase Liquid Cooling Using an Improved Effectiveness-NTU Cold Plate Model". In: Garden Grove, California, USA: American Society of Mechanical Engineers, Oct. 2022, V001T01A008. ISBN: 978-0-7918-8655-7. DOI: 10.1115/IPACK2022-97421.

Part III

Literature Study

1

Thermo-hydraulic Performance of Heat Transfer Surfaces

The design of heat transfer surfaces has long been an essential component in the advancement of the efficiency and compactness of thermal systems. From early shell-and-tube exchangers and plate-and-fin configurations to novel topology-optimized lattices, the fundamental engineering objective has remained unchanged: to maximize the heat transfer rate per unit volume while minimizing the associated pressure losses.

The earliest heat exchangers, shell-and-tube, double-pipe, and plate-type configurations developed in the early 20^{th} century for industrial applications, were prime surface designs. In these devices, heat transfer occurs directly at the primary surface (the tube wall or plate) without additional appendages or extensions. While robust and easily manufactured, prime surface heat exchangers faced a fundamental limitation: when one or both fluids had low heat transfer coefficients (as is common with gases), achieving adequate thermal performance required very large surface areas. This translated directly into heavy, bulky equipment unsuitable for applications with strict weight and volume constraints, such as aerospace systems.

The development of compact heat exchangers in the mid-20^{th} century addressed these limitations through the introduction of secondary/extended surfaces, fins or appendages attached to the primary surface to multiply the available heat transfer area. This approach proved particularly effective for gas-side heat transfer, where the heat transfer coefficients are typically much lower than those on the liquid side. By adding fins, designers could increase surface area by a large factor compared to the prime surface alone. The result was a new class of heat exchangers with dramatically higher surface area density (area per unit volume), enabling substantial reductions in size and weight while maintaining or improving thermal performance [58, 59].

As applications expanded into aerospace, microelectronics, and other high-performance energy systems, simply adding surface area proved insufficient. Designers needed not only more area, but also higher heat transfer coefficients to meet increasingly aggressive performance targets. This drove the development of advanced fin geometries, such as offset strip fins, louvered fins, and pin fins, that went beyond passive area augmentation. These surfaces actively enhance heat transfer through flow interruption, thermal boundary layer disruption, and repeated thermal development. These designs demonstrated that strategic geometric manipulation could yield disproportionate gains in thermal performance, establishing the foundation for modern compact heat exchanger technology [43].

In recent decades, attention has shifted toward porous and lattice-based structures, inspired by natural forms and enabled by advances in computational design and additive manufacturing. These structures offer several advantages over conventional cooling geometries: they enhance fluid mixing and promote more uniform temperature distributions, while their high surface area density and mechanical strength enable compact thermal designs. Additionally, the geometric versatility of lattice architectures allows their thermal and flow characteristics to be tailored to specific applications, making them attractive candidates for lightweight, multifunctional heat exchangers.

Due to their geometric complexity, analytical methods are insufficient for characterizing these high-performance fins and lattice structures. Performance must be determined through controlled experiments or high-fidelity computational analyses, with results generalized into correlations using recognized scaling laws [43].

The thermo-hydraulic performance of a heat transfer surface refers to the simultaneous consideration of its heat transfer and pressure drop characteristics. In practical design, both aspects are inseparable: an increase in heat transfer rate often comes at the expense of higher flow resistance. To generalize experimental or numerical findings across fluids, geometries, and operating conditions, results are usually expressed in terms of dimensionless correlations. These correlations allow surface-specific behavior measured at small scale to inform system-level design [43, 58]. In this way, dimensionless correlations connect the detailed local behavior to the overall performance of compact heat exchangers.

Since the introduction of secondary surfaces in heat exchanger design, the scientific community has made sustained efforts to characterize their thermo-hydraulic performance through dimensionless correlations. Early foundational work established benchmark correlations for smooth channels and pipes, including friction factor correlations by Blasius [47], Colebrook [44], and Moody [48], as well as heat transfer correlations expressed in terms of Nusselt number by Dittus and Boelter [50] and Gnielinski [60]. Building on these foundations, subsequent research has systematically characterized various enhanced surface geometries. Notable examples include the comprehensive characterization of multiple fin configurations by Kays and London [43], such as offset strip-fin, louvered-fin, and wavy-fin surfaces, the widely adopted offset strip-fin correlations developed by Manglik and Bergles [61], and the characterization of pin-fin arrays by Metzger et al. [40]. These correlations have been extensively validated and continue to serve as reference in heat exchanger design and modeling.

Recent advances in additive manufacturing have expanded the design possibilities for heat transfer surfaces, enabling complex three-dimensional geometries with interconnected flow paths. These structures achieve extremely high surface area densities and promote more uniform flow and temperature distributions than conventional finned designs. However, their thermo-hydraulic behavior differs fundamentally from that of traditional surfaces: flow is unsteady, three-dimensional, and often resembles flow through porous media [9]. Consequently, the characterization work previously done for fins and pin fins must be revisited for these new geometries. Reliable characterization requires high-fidelity numerical simulations or experiments, from which new correlations must be developed. This challenge has driven growing research interest in understanding and modeling the thermo-hydraulic behavior of lattice-based heat transfer surfaces, as reviewed in the following section.

1.1. Lattice Structures

Although definitions may vary slightly between authors, lattice structures are generally described as three-dimensional architectures made up of interconnected cells that are arranged repeatedly and continuously in space. They can also be understood as porous materials formed by networks

of struts and nodes distributed throughout a three-dimensional volume [9]. This broad definition encompasses a wide variety of structures, which can be classified based on characteristics such as uniformity, randomness, and periodicity. For the purpose of this work, the focus is placed on uniform and periodic lattice structures. These can be further divided into two main categories: strut-based lattices, which are designed using geometric wireframes, and surface-based lattices, which are defined through mathematical formulations.

1.1.1. State-of-the-Art Characterization of Strut-Based Lattices

Strut-based lattice cooling structures are receiving increasing attention as potential internal cooling architectures for compact heat exchangers and aerospace applications such as turbine vane trailing edge cooling. Compared to conventional pin-fin or ribbed channels, these geometries offer several advantages: enhanced mixing and vortex generation promote more uniform temperature distributions, while increased surface area and mechanical strength enable compact thermal designs. The versatility of lattice structures, encompassing numerous configurations and topologies (see Figure 28) with struts manufactured in various shapes, allows their thermal and mixing characteristics to be tailored to specific applications.

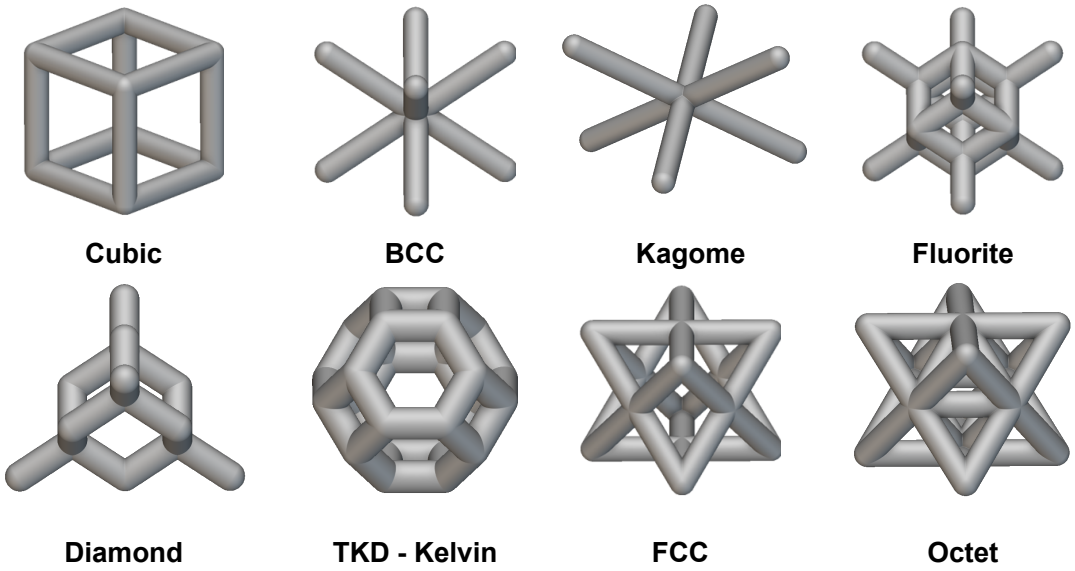

Figure 28: 3D illustration of examples of strut-based lattice structures.

Given the thermo-hydraulic and structural potential of these structures, coupled with advances in additive manufacturing that have increased the feasibility of implementing them in cooling applications, the scientific community has made considerable efforts to characterize their behavior. Research can be broadly understood through two complementary approaches: cross-geometry comparisons that map the performance landscape across topologies and hybrid concepts, and within-family parametric studies that quantify sensitivities to design variables such as strut thickness, porosity, and flow configuration.

The first approach focuses on identifying the best-performing topologies and understanding why certain configurations excel. Researchers have sought to determine which lattice families achieve optimal thermo-hydraulic performance and what flow mechanisms drive these advantages. Kaur et al. [62] experimentally investigated four regular lattice geometries (Octet, TKD, FD-CUBE, and Cube) with similar porosity to assess their suitability for turbine vane trailing edge cooling. The additively manufactured test articles were examined under representative conditions, with heat flux imposed on either both walls or a single wall. Tests were conducted in the turbulent regime

($10{,}000 < Re < 40{,}000$), typical of turbine vane trailing edge cooling applications. The study compared overall thermo-hydraulic performance, defined as $(Nu/Nu_0)/(f/f_0)^{1/3}$, across geometries, as presented in Figure 29, weighting heat transfer enhancement against pressure drop penalties. Results showed that the Cube lattice achieved the highest thermo-hydraulic performance across the Reynolds number range. The Octet and FD-CUBE structures achieved high heat transfer performance but at the expense of high pressure losses, illustrating the inherent trade-off in lattice design. An important finding was the sensitivity of performance to thermal boundary conditions, as heating both walls versus a single wall yielded different relative rankings, indicating that optimal lattice selection is highly application-specific.

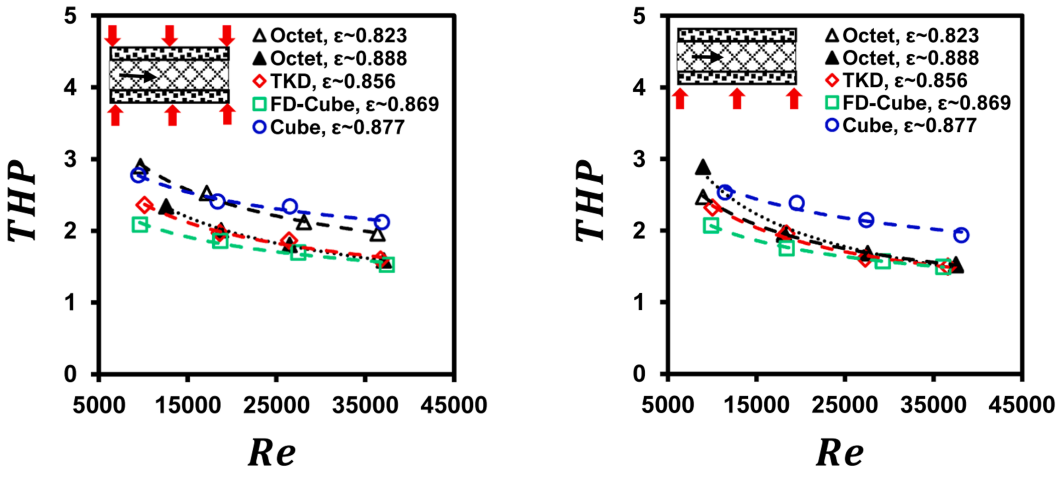

Figure 29: Thermo-hydraulic performance (THP) of the lattice structures, when heating both walls (left) and a single wall (right), adapted from [62].

Building on this comparative approach, Castelli et al. [11] conducted a high Reynolds number experimental campaign ($Re = 18{,}000 - 40{,}000$) to benchmark the performance of a Kagome lattice structure against traditional choices for turbine vane cooling, such as pin-fin arrays and matrix structures. Eight coupons were tested in total: Smooth, Dimples, Pin Fins, Simple Matrix (SM), Double Matrix (DM), and three versions of Kagome (LD/MD/HD) with varying lattice densities. The Double Matrix achieved extremely high Nusselt numbers (up to 13× the Dittus-Boelter correlation) but incurred large friction penalties that degraded overall efficiency at high Reynolds numbers. The high-density Kagome lattice (Kagome-HD) matched the efficiency of Pin Fins and Simple Matrix while offering potential structural advantages. These results confirmed that while "brute-force" approaches using high surface area and enhanced mixing can be effective to increase the heat transfer performance, they often suffer from excessive hydraulic losses. The Kagome lattice offered a more balanced thermo-hydraulic performance at engine-relevant Reynolds numbers.

To better understand the flow physics underlying these performance differences, Corbett and Thole [12] compared two novel lattice structures through combined experimental and numerical analysis. Their study, with an emphasis on the numerical analysis, consisted of Large Eddy Simulations (LES), validated against experiments, to examine unit-cell rows of the Kagome and BCC lattices at $Re = 20{,}000$. The numerical analysis revealed distinct flow development characteristics, as evidenced in the turbulence intensity contours depicted in Figure 30. BCC reached hydrodynamic and thermal development in fewer unit cells, while Kagome exhibited asymmetric flow patterns and uneven local heat transfer. Vortex shedding from BCC struts coupled strongly with endwall boundary layers, significantly enhancing local heat transfer. The authors concluded that development length

and coherent vortex dynamics are topology-dependent features that should inform system-level design decisions, such as the placement of mixing sections versus flow stabilization regions.

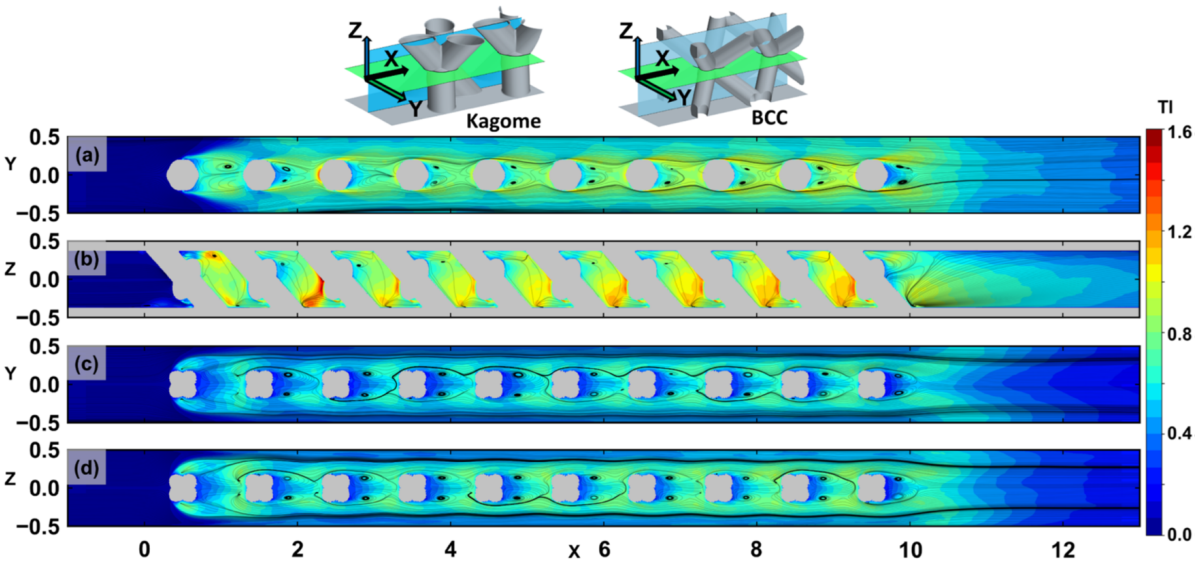

Figure 30: Turbulence intensity at mid-height and mid-span planes for the (a-b) Kagome and (c-d) BCC lattices, adapted from [12].

The comparative studies reviewed above establish a performance hierarchy among lattice families and reveal the flow mechanisms responsible for their distinct behaviors. However, understanding which topology performs best does not address how to optimize that topology for a specific application. This requires a parametric analysis: systematic variation of geometric parameters within a single lattice family to quantify design sensitivities and develop the functional relationships necessary for predictive modeling and correlation-based design.

Liang et al. [13] conducted a combined experimental and CFD investigation of FCC lattices in a rectangular channel, holding porosity constant while varying strut cross-sectional shape (circular, rectangular, elliptical). The non-circular geometries, rectangular and elliptical struts, increased both local and spatially averaged Nusselt numbers due to enhanced wetted area and stronger vortex formation in the wake regions. However, the circular FCC have a superior overall efficiency, once friction penalties are included. This shows that strut shape offers a way to tune the heat transfer-pressure loss trade-off without changing porosity, providing designers with an additional variable to adjust performance.

Extending this parametric approach to a different lattice family, Lorenzon et al. [14] experimentally characterized staggered BCC arrays with three strut diameters using additively manufactured coupons. As expected, larger struts increased the wetted surface area and consequently the Nusselt number, but also led to higher friction factors due to increased flow blockage. The overall thermo-hydraulic efficiency remained approximately constant across the diameter range, indicating that geometric variations produce proportional shifts in both heat transfer and pressure loss. When the Nusselt number, friction factor, and Reynolds number were normalized using a hydraulic diameter that incorporates the BCC strut geometry, the data from all three configurations collapsed onto single curves, as shown in Figure 31. This dimensional analysis enabled the development of power-law correlations for Nu and f as functions of Reynolds number and the ratio of the strut diameter to the coupon hydraulic diameter. These correlations are valid for turbulent flow ($Re > 10{,}000$) with air as the working fluid and provide a predictive model for this specific BCC configuration.

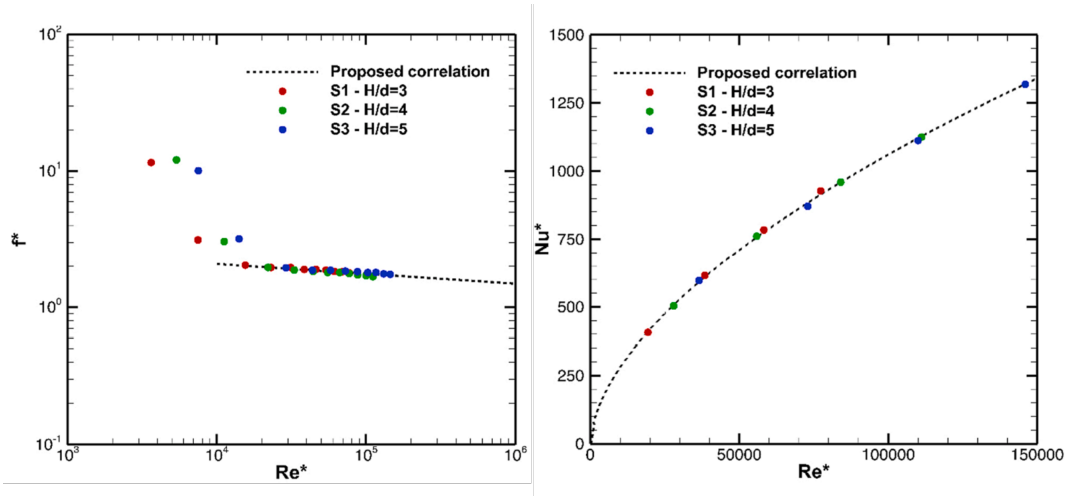

Figure 31: Comparison of experimental results against proposed correlation for: (left) modified friction factor, f^*, and (right) modified Nusselt number, Nu^* , adapted from [14].

1.1.2. State-of-the-Art Characterization of Surface-Based Lattices

Surface-based lattices can also be termed triply periodic minimal surfaces (TPMS). TPMS are smooth, continuous surfaces that exhibit zero mean curvature at every point and repeat periodically in three independent spatial directions. Additionally, these surfaces divide space into two interpenetrating but non-overlapping flow paths. The mathematical foundations of TPMS date back to Schwarz's 1865 description of the Diamond and Primitive structures [34]. Building on this work, his student Neovius described the complement of the Primitive structure (C(P) or Neovius structure) in 1883 [63]. Nearly a century later, Schoen [35] expanded the family of known minimal surfaces by proposing additional configurations, including the Gyroid, IWP, and several others. Examples of these structures are shown in Figure 32.

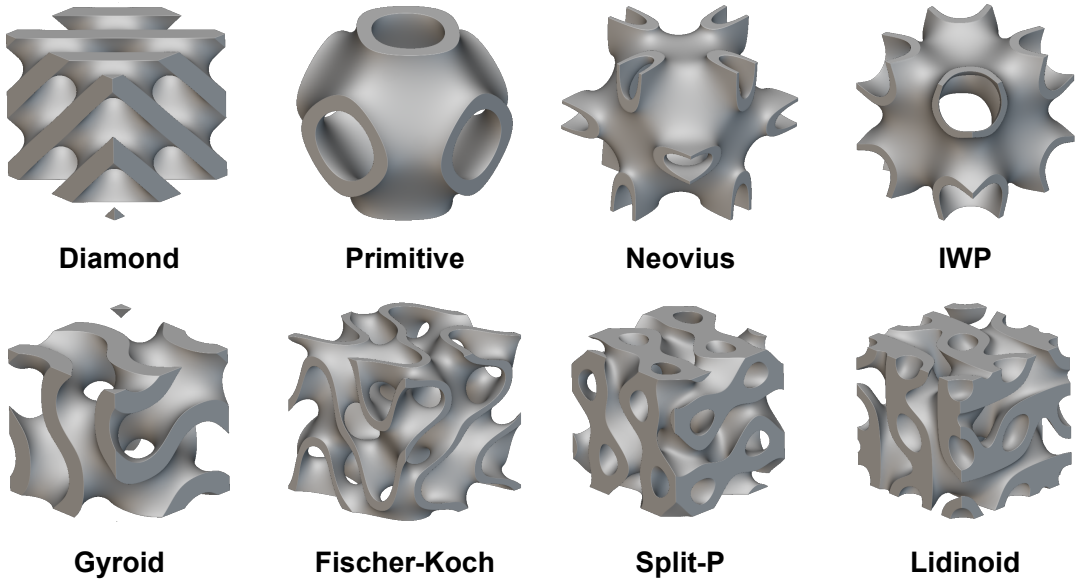

Figure 32: 3D illustration of examples of surface-based lattice structures.

At the time of their discovery, TPMS structures were not considered for thermal management applications because manufacturing methods did not exist to produce them. The recent development of additive manufacturing changed this limitation. TPMS structures are now attractive

candidates for heat transfer applications because of their high surface area density, smooth flow paths, and self-supporting geometry, features that make them well-suited for multifunctional components such as lightweight compact heat exchangers. However, a complete understanding of their thermo-hydraulic behavior has not yet been established. Recent studies have therefore focused on benchmarking their thermo-hydraulic performance and developing correlations and models for their heat transfer and pressure loss characteristics.

The foundational stage of TPMS research, particularly in the context of fluid dynamics and heat transfer, centered on hydrodynamic modeling under laminar or creeping flow conditions, with the goal of establishing permeability and inertial drag correlations.

Rathore et al. [15] performed pore-scale CFD simulations of four TPMS geometries: Diamond, IWP, Primitive, and Gyroid. The domain consisted of a 4x4x4 array of unit cells, with translational periodic boundary conditions applied between inlet and outlet to simulate a hydrodynamically developed flow condition and no-slip conditions prescribed to all the lateral walls, as depicted in . Through these simulations, the authors quantified key transport properties including the permeability (K) and higher-order inertial coefficients (β and α) and established the range of validity for the Darcy law in these structures.

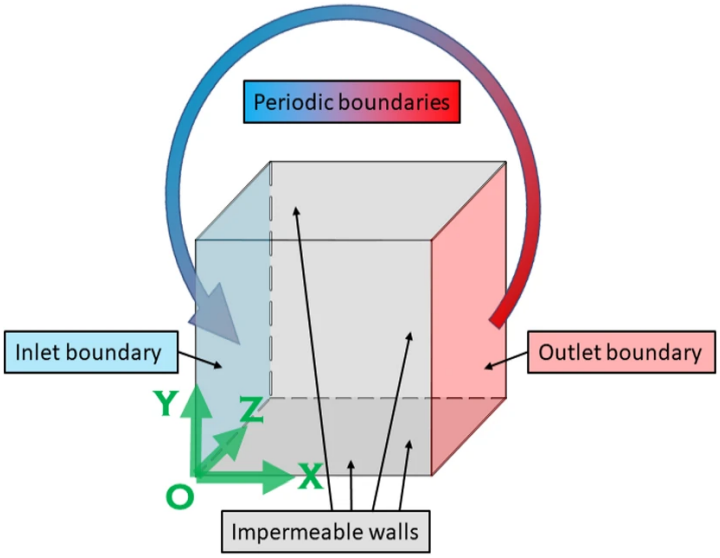

Figure 33: Representation of a lattice computational domain with the translational periodic condition in the streamwise direction, adapted from [15].

While the previous study was performed on arbitrarily selected structures in terms of porosity, Piedra et al. [16] extended this approach by systematically varying porosity to develop power-law correlations between porosity and the transport coefficients in the Darcy-Forchheimer formulation, for Primitive and IWP topologies. Importantly, the simulations were conducted on single unit cells with periodic boundary conditions on the lateral walls, and extended inlet and outlet sections.

Importantly, both studies adopted representative volume element (RVE) approaches, although with different modeling assumptions. This RVE-based methodology represents a significant computational advantage as it enables an efficient characterization of transport properties that can subsequently be extrapolated to full-scale components without the prohibitive cost of simulating entire structures.

The next phase of research expanded from purely hydrodynamic analysis to conjugate heat transfer (CHT) modeling, addressing how the TPMS topology affects both fluid-side convection and solid

conduction pathways. Rathore et al. [18] extended their hydrodynamic work to include conjugate heat transfer simulations using the same 4x4x4 unit cell domain. The authors applied constant heat flux to the lateral walls and examined laminar flows spanning $0.01 < Re < 100$. This study analyzed how the Nusselt number varies with flow conditions, characterized the dominant heat transfer mechanisms, and mapped local temperature distributions within the TPMS structure.

Building on Piedra's approach [16], Ornelas-Ramón et al. [17] investigated Gyroid structures across different porosities. They simulated flow through a 3x3x3 array of Gyroid unit cells arranged in a channel with heating applied to one wall. Following Piedra's methodology, they derived porosity-dependent correlations for the Darcy-Forchheimer transport coefficients (Figures 34a and 34b), highlighting the distinct hydraulic characteristics of Gyroids compared to Primitive and IWP surfaces. As shown in Figure 34a, permeability transitions from linear behavior at low porosities to power-law dependence at high porosities, while the Forchheimer coefficient exhibits the inverse trend (Figure 34b), which was not captured in the other topologies analysis. Additionally, their thermal analysis went further by establishing a Nusselt number correlation for laminar flow conditions (Figure 34c), valid across different fluids with Prandtl numbers ranging from 0.7 to 14.

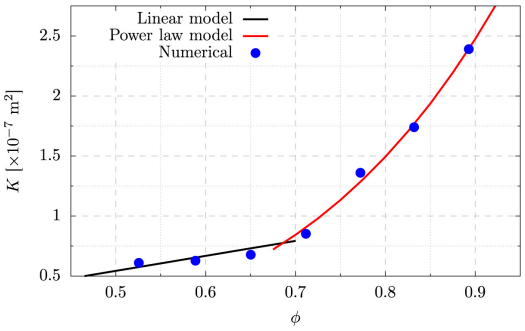

(a) Permeability as a function of porosity.

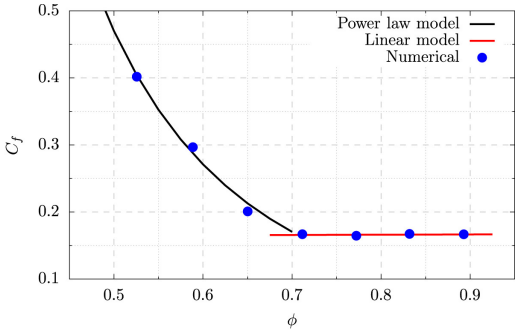

(b) Forchheimer coefficient as a function of porosity.

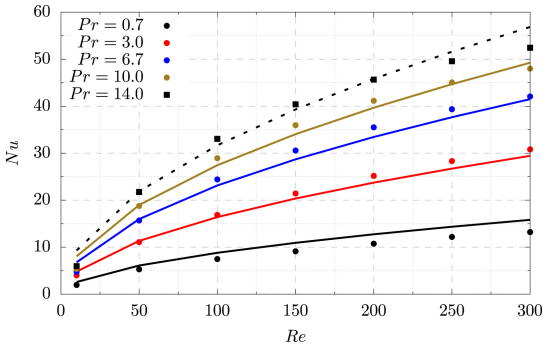

(c) Nusselt number as a function of Reynolds number for various Prandtl numbers.

Figure 34: Darcy-Forchheimer transport coefficients and thermal performance of Gyroid structures. Simulation data (symbols) and fitted correlations (lines) adapted from [17].

Torri et al. [19] extended the analysis beyond laminar flow conditions by comparing TPMS types (Gyroid, IWP, Primitive, Diamond) against conventional turbulator geometry at two fixed Reynolds numbers, one laminar and one turbulent.Their results showed that TPMS structures delivered superior heat transfer compared to the conventional fin geometry, though at the expense of higher pressure drops. Besides this, Torri noted a practical limitation: meshing an entire heat exchanger filled with TPMS structures was computationally prohibitive, making it necessary to develop methods that reduce this computational cost.

Moving from micro-scale analysis to system-level design, Yan et al. [20] simulated full TPMS heat exchangers using conjugate heat transfer models for laminar water flow. They compared four TPMS types (Gyroid, Diamond, Primitive, and IWP) against a printed circuit heat exchanger (PCHE), evaluating Nusselt number and friction factor. Each TPMS heat exchanger consisted of a 4x4x4 stack of unit cells with two fluids flowing in separate channels in a cross-flow arrangement. The study combined system-level performance metrics with detailed analysis of local flow patterns and heat transfer mechanisms. As illustrated in Figure 35 for the gyroid geometry, the curved internal architecture generates secondary circulation flows that create localized regions of enhanced and reduced heat transfer on the channel walls. While significantly weaker than the main flow, these secondary flows represent an important contribution to the overall heat transfer enhancement. Consistent with Torri's findings [19], the TPMS heat exchangers showed superior heat transfer compared to the PCHE, though at the cost of higher pressure losses. Nevertheless, when assessed using an overall performance evaluation criterion that accounts for both heat transfer enhancement and pressure drop penalty, the TPMS designs remained favorable.

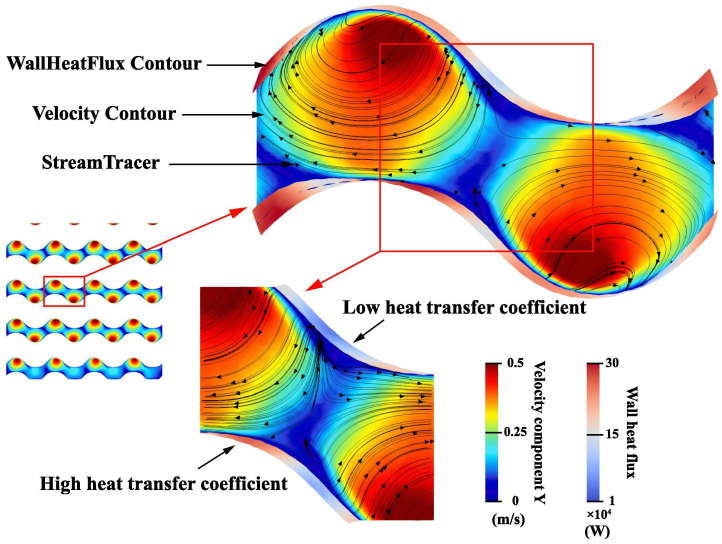

Figure 35: Velocity streamlines and wall heat flux distribution in a gyroid heat exchanger. Adapted from [20].

Other studies have focused on fully turbulent regime analyses, consistent with the operational range of some compact heat exchangers and aerospace cooling applications. Samson et al. [21] studied Gyroid heat sinks at high Reynolds numbers ($2{,}500 - 40{,}000$), systematically varying cell size, porosity, and material properties, and reporting thermo-hydraulic performance metrics (Nu, f, η). Although no correlations were formulated connecting geometrical parameters with performance metrics, previous conclusions from other studies were reinforced. First, Gyroids outperformed the benchmarking geometry, in this case, straight fins, but with increased pressure losses. Additionally, Nusselt trendlines collapsed into a single curve despite geometrical variations, provided that the Nusselt number was defined using the typical porous media hydraulic diameter, since this length scale accounts for changes in heat transfer area resulting from variations in geometrical parameters.

Wang et al. [22] extended the investigation of the turbulent regime ($1{,}000 < Re < 20{,}000$) to other four TPMS types (Primitive, Neovius, Fischer-Koch and IWP). In this work, correlation models for *Nu* and f are proposed as functions of both Reynolds number and a morphological volume-share parameter ($R = V_{\mathrm{f}}/V_{\mathrm{total}}$), that can be interpreted as a porosity. However, the Nusselt number correlation is not valid for fluids other than the studied one which is helium as it does not account for the Prandtl number. On the other hand, Brambati et al. [23] developed a universal turbulent correlation of the form $Nu = ARe^{m}Pr^{n}$, valid across fluids (air, water, acetone), TPMS topologies

(Gyroid, Primitive, Diamond) and structure porosities. In this work, CHT simulations are performed on an array of 3 TPMS unit cells, with a counterflow arrangement with a hot and cold fluid. This work marked a step toward topology-independent predictive modeling and cross-fluid generalization.

The field started converging toward generalized, multi-parameter correlations that incorporate flow regime, fluid properties, and morphology metrics, yet validation remains limited beyond ideal, small-scale or single-material test domains. A significant turning point in the literature came with the shift toward experimental validation, which was essential to verify numerical predictions and evaluate whether these structures could actually be manufactured. Early experimental work on TPMS relied on non-metallic materials because additive manufacturing technology was not advanced enough to produce these complex geometries in metal [24, 64]. As AM technology matured, the fabrication of metal TPMS test articles became feasible, and the following publications have reported experimental results on TPMS performance.

Reynolds et al. [24] conducted one of the most comprehensive experimental studies on TPMS heat exchangers, testing nine different topologies. In addition to this, Gyroid structures were examined over a wide range of porosities (20% to 93%) and hydraulic diameters (2 mm to 10 mm). The heat exchangers were printed with a polymeric material, and because the thermal conductivity of the polymer is low, the fluid used on one channel of the heat exchanger was air, a fluid with low heat capacitance, such that a measurable temperature gradient was created even for small heat transfer rates. Water was used as the second fluid. The experimental results showed that, with proper parameterization, the relationship between Nusselt number and Reynolds number was largely independent of porosity and hydraulic diameter, confirming the previous results obtained by Samson et al. [21]. This finding enabled the development of a single correlation for the Gyroid structure valid for a range of different fluids and for the Reynolds number range tested ($100 < Re < 2{,}500$).

Tang et al. presented two studies [25, 26] that combined numerical analysis and experimental campaigns. The first study evaluated the convective heat transfer performance of three TPMS structures, Diamond, Gyroid, and IWP, whose respective test articles were manufactured from aluminum and tested under constant wall temperature conditions [25]. Performance was compared against a conventional finned heat sink with equivalent surface area. Experimentally validated simulations showed that TPMS structures outperform traditional fins in heat transfer efficiency but with higher flow resistance, consistent with previous findings. Among the tested geometries, the Diamond topology showed the highest Nusselt number enhancement, followed by Gyroid and IWP. Beyond performance comparison, the study examined the mechanisms responsible for enhanced heat transfer in TPMS structures.

The second study expanded this investigation to five TPMS topologies: Fischer-Koch-S, Diamond, IWP, Gyroid, and Primitive [26]. The test articles were tested in a Reynolds number range of $200 - 4{,}000$ under isothermal wall conditions. Experimental measurements of temperature difference and pressure drop were combined with numerical simulations to characterize thermal and hydraulic performance. The Fischer-Koch-S structure achieved the highest heat transfer performance, followed by Diamond, IWP, Gyroid, and Primitive. The study introduced the perforated area ratio, defined as the unobstructed projected area when the TPMS structure is viewed orthogonally in the flow direction, to explain variations in flow and heat transfer behavior. This analysis revealed that non-perforated structures (Diamond, Fischer-Koch-S) produce more uniform velocity fields and superior heat transfer compared to perforated geometries.

The experimental investigations discussed thus far have focused on heat exchangers composed of stacks or arrays of TPMS unit cells [24–26]. Zou et al. [27] extended this work to industrial scale by manufacturing and testing a Diamond meter-scale heat exchanger. The experimental results first validated numerical simulations, which provided insight into the flow structures and heat transfer

mechanisms within the heat exchanger. The experimental data was then used to develop friction and heat transfer correlations valid for different fluids across $1{,}000 < Re < 25{,}000$. The Nusselt number correlation was also compared against results from previous studies [23, 24], showing good agreement with deviations smaller than 20%.

In summary, extensive research has been conducted to characterize the flow phenomena and heat transfer mechanisms in lattice structures. In the past decade, numerous numerical and experimental studies have explored a wide variety of topologies, ranging from strut-based designs to continuous TPMS geometries, to investigate their thermo-hydraulic behavior. Despite this progress, most reported correlations for the Nusselt number and the friction factor remain geometry-specific and confined to narrow Reynolds number ranges (either laminar or turbulent regime), limiting their general applicability. This limitation is particularly significant for compact heat exchanger applications, where the Reynolds number of interest typically falls within the range $500 - 15{,}000$ [43]. Although it is generally recommended to design outside of the transition regime, this range inevitably encompasses the transition region, making it difficult to avoid in practice. Consequently, the absence of a predictive model for this regime becomes highly restrictive for the design of compact heat exchangers.

Furthermore, as concluded by Caket et al. [28] in their extensive review, characterization efforts have often remained fragmented, employing different modeling assumptions, morphological descriptors, boundary conditions, and data reduction methods, thus preventing the formulation of universal scaling laws. A clear research gap therefore persists: currently, there are no comprehensive, cross-regime correlations or physical laws that consistently describe hydrodynamic and thermal transport across porosities and flow regimes in lattice structures. To support the design of compact heat exchangers, a thorough and consistent characterization of these novel structures is required.

2

Component-Level Heat Exchanger Modeling

The design of advanced thermal management systems requires predictive system-level models that capture the essential physics without excessive computational cost, to avoid expensive simulations and/or prototyping. The empirical correlations discussed previously describe local microscale physics, and predictive models are the key to connect this information with component-level performance.

Heat exchanger design involves several tasks that differ in their objectives and constraints. In a sizing or preliminary design problem, the heat transfer area must be determined to allow both cold and hot streams to reach desired outlet temperatures while maintaining pressure drops below acceptable thresholds. Without explicit pressure drop constraints, the design process may yield an excessively compact heat exchanger with unfeasible pressure drops. In contrast, in off-design or simulation analyses, the heat exchanger geometry and size are known, and the objective is to determine the outlet conditions of both streams given their inlet temperatures and mass flow rates. Rating is a related but distinct task: given a fixed heat exchanger geometry, the analysis evaluates whether the existing area is sufficient to achieve the desired outlet temperatures while satisfying the maximum allowable pressure drop limits [43, 59].

For sizing problems, the logarithmic mean temperature difference (LMTD) approach is well-suited because the outlet temperatures are known variables, making it straightforward to calculate the required heat transfer area. When optimizing heat exchanger geometry to achieve the best performance, the design variables become the geometrical parameters. With inlet conditions specified, the outlet temperatures or power output, balanced against pressure drop across the heat exchanger, becomes the objective function to be determined. Considering this, this scenario effectively constitutes a simulation problem. For simulation applications, the LMTD technique could theoretically be applied iteratively until convergence, but this approach is inefficient. The ϵ-NTU method is more suitable for these cases, as it allows calculations to proceed sequentially based on two non-dimensional parameters: ϵ (heat exchanger effectiveness) and NTU (number of transfer units), whose definitions are provided in the next section [59].

2.1. Fundamentals of the Effectiveness-NTU Method

To introduce the formulation of the ϵ-NTU method, it is convenient to start from a simple steady-state heat transfer problem. In a heat exchanger, thermal energy flows from the hot fluid at bulk temperature T_{h} to the cold fluid at bulk temperature T_{c} through an interfacing wall. This process occurs in three sequential steps: heat transfer from the hot fluid to the wall by convection, conduction through the wall itself, and finally heat transfer from the wall to the cold fluid by convection. Under steady operating conditions, the heat flux remains constant throughout this series of processes.

This heat transfer sequence can be understood through an electrical circuit analogy, as illustrated in Figure 36, where heat flux corresponds to electric current and temperature difference corresponds to voltage. The three sequential heat transfer processes, two convection steps and one conduction step, are then equivalent to three thermal resistances connected in series.

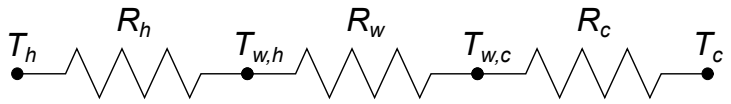

Figure 36: Thermal resistance network analogy of a heat exchanger, illustrating the conduction and convection processes as a series of equivalent thermal resistances.

In the general case, the heat transfer areas associated with the hot and cold sides of the exchanger are not necessarily equal, due to different surface geometries or flow arrangements. The three thermal resistances are therefore defined as

$$R_{\mathrm{h}} = \frac{1}{\eta_{\mathrm{o,h}}\, h_{\mathrm{h}}\, A_{\mathrm{h}}}, \qquad R_{\mathrm{w}} = \frac{t}{\lambda_{\mathrm{s}}\, A_{\mathrm{w}}} \qquad R_{\mathrm{c}} = \frac{1}{\eta_{\mathrm{o,c}}\, h_{\mathrm{c}}\, A_{\mathrm{c}}}, \tag{2.1}$$

where A_{h} and A_{c} denote the effective heat transfer areas on the hot and cold sides, respectively, and A_{w} represents the characteristic conduction area of the separating wall.

In the absence of extended surfaces, the overall surface efficiency η_{o} is unity. However, when fins are present, the temperature gradient along the extended surface reduces their effectiveness. The overall efficiency must therefore account for this reduction, as expressed by:

$$\eta_{\mathrm{o}} = 1 - \frac{A_{\mathrm{f}}}{A}(1 - \eta_{\mathrm{f}}) \tag{2.2}$$

where A_{f} represents the finned (extended) area and η_{f} the fin efficiency.

Since the thermal resistances are arranged in series, the total thermal resistance corresponds to the sum of the individual contributions:

$$R_{\mathrm{total}} = R_{\mathrm{h}} + R_{\mathrm{w}} + R_{\mathrm{c}} \tag{2.3}$$

The heat transfer rate can therefore be expressed directly in terms of the total thermal resistance as

$$\dot{Q} = \frac{T_{\mathrm{h}} - T_{\mathrm{c}}}{R_{\mathrm{total}}}. \tag{2.4}$$

The overall heat transfer capacity of the exchanger is characterized by the thermal conductance, *UA*. With this definition, the heat transfer rate can also be computed as follows

$$\dot{Q} = UA(T_{\mathrm{h}} - T_{\mathrm{c}}) \tag{2.5}$$

Comparing these two expressions for the heat transfer rate, $\dot{Q}$, the thermal conductance can be defined as the reciprocal of the total thermal resistance

$$UA = \frac{1}{R_{\mathrm{total}}} = \left(\frac{1}{\eta_{\mathrm{o,h}} h_{\mathrm{h}}} + \frac{t}{\lambda_{\mathrm{s}}} + \frac{1}{\eta_{\mathrm{o,c}} h_{\mathrm{c}}} \right)^{-1} \tag{2.6}$$

It is important to note that the numerical value of the overall heat transfer coefficient depends on the choice of the reference area. However, the thermal conductance *UA*, and therefore the heat transfer rate, remains invariant.

Originally proposed by Kays and London [43], the ϵ-NTU method is based on three non-dimensional parameters, chosen based on their convenience and physical significance.

Firstly, the heat capacity rates of the hot and cold streams are given by

$$C_{\mathrm{h}} = \dot{m}_{\mathrm{h}} c_{\mathrm{p,h}}, \quad C_{\mathrm{c}} = \dot{m}_{\mathrm{c}} c_{\mathrm{p,c}}, \tag{2.7}$$

and the heat capacity ratio is defined as

$$C^* = \frac{C_{\min}}{C_{\max}}. \tag{2.8}$$

where, $C_{\min}$ and $C_{\max}$ are the smaller and larger of the two magnitudes of C_{h} and C_{c}, respectively.

For a heat exchanger with inlet temperatures $T_{\mathrm{h,in}}$ and $T_{\mathrm{c,in}}$ and outlet temperatures $T_{\mathrm{h,out}}$ and $T_{\mathrm{c,out}}$, the effectiveness is defined as:

$$\epsilon = \frac{\dot{Q}}{\dot{Q}_{\max}} = \frac{C_{\mathrm{h}}(T_{\mathrm{h}}^{\mathrm{in}} - T_{\mathrm{h}}^{\mathrm{out}})}{C_{\min}(T_{\mathrm{h}}^{\mathrm{in}} - T_{\mathrm{c}}^{\mathrm{in}})} = \frac{C_{\mathrm{c}}(T_{\mathrm{c}}^{\mathrm{in}} - T_{\mathrm{c}}^{\mathrm{out}})}{C_{\min}(T_{\mathrm{h}}^{\mathrm{in}} - T_{\mathrm{c}}^{\mathrm{in}})} \tag{2.9}$$

this is the ratio of the actual heat transfer rate in a heat exchanger to the thermodynamically limited maximum possible heat transfer rate in a counterflow heat exchanger with infinite heat transfer surface.

The overall heat transfer capability of the exchanger is described by the Number of Transfer Units (NTU):

$$NTU = \frac{UA}{C_{\min}}, \tag{2.10}$$

Closed-form relationships between ϵ, NTU and C^* are available for several canonical flow configurations (counterflow, parallel flow, and cross-flow with mixed or unmixed streams), as tabulated by Kays and London [43] and presented from Equation 2.11 to Equation 2.14.

Counterflow:

$$\epsilon = \frac{1 - \exp\left[-NTU\,(1 - C^*)\right]}{1 - C^* \exp\left[-NTU\,(1 - C^*)\right]} \tag{2.11}$$

Parallel Flow:

$$\epsilon = \frac{1 - \exp\left[-NTU\left(1 + C^*\right)\right]}{1 + C^*} \tag{2.12}$$

Cross-flow, Both Fluid Unmixed:

$$\epsilon = 1 - \exp\left(\frac{\exp\left(-C^* NTU^{0.78}\right) - 1}{C^* NTU^{-0.22}}\right) \tag{2.13}$$

Cross-flow, Both Fluid Mixed:

$$\epsilon = \frac{1}{\frac{1}{1 - \exp(-\mathrm{NTU})} + \frac{C^*}{1 - \exp(-C^* \,\mathrm{NTU})} - \frac{1}{\mathrm{NTU}}} \tag{2.14}$$

These relationships enable component-level performance prediction, given only the geometric conductance (UA) and flow capacity rates. However, the preceding analysis and relationships are only valid under the following set of assumptions:

1. The heat exchanger operates under steady-state conditions.
2. There is no heat transfer to the surroundings.
3. The specific heat at constant pressure is constant for each fluid, which is valid if the temperature difference is not significant.
4. The overall heat transfer coefficient between the fluids is constant throughout the heat exchanger.

If the overall heat transfer coefficient or the specific heat of each fluid is not uniform, heat exchanger calculations may be made by subdividing the heat exchanger into sections over which these quantities are nearly uniform and by applying the previously developed relations to each subdivision. This method, referred to as the cell method in [65], consists of discretizing the heat transfer area into a finite number of elements over which the aforementioned assumptions hold. An example of this discretization can be observed in Figure 37. Although complexity appears to increase significantly with discretization, the problem can still be resolved using simple algebraic equations, so the computational cost does not increase substantially.

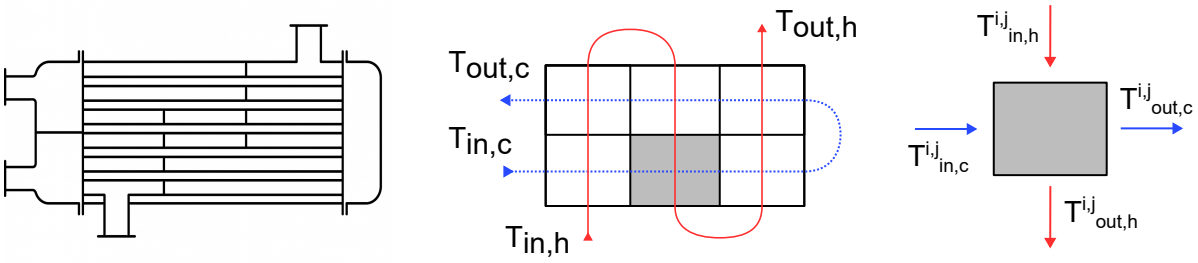

Figure 37: Example of the discretization scheme used in the cell method for a shell-and-tube heat exchanger, adapted from [65].

This approach is also particularly useful for computing the performance of heat exchangers with complex flow arrangements. Navarro and Cabezas-Gómez [66] validated the model by comparing the simulated results against established theoretical algebraic relations for various configurations, demonstrating high accuracy even for complex industrial designs where existing ϵ-NTU relations are often unavailable or imprecise.

2.2. Adaptation of the Effectiveness-NTU Model to a Cold Plate

To design and evaluate two fluid heat exchangers, the ϵ-NTU method developed by Kays and London [43] is widely used in industry and the scientific community. However, its application to electronic cooling devices such as heat sinks and cold plates is not evident, though with the right set of assumptions it becomes possible. Copeland [51] applied the ϵ-NTU method to air-cooled heat sinks, by modeling them as isothermal. An isothermal heat sink, at temperature $T_{\mathrm{s}}^{\mathrm{base}}$, implies that $C_{\max} \to \infty$, thus, $C^* = 0$. Intuitively, $C_{\min}$ is the heat capacity rate of the working fluid. Under this condition, the counterflow, parallel flow, and cross-flow (both fluids mixed) effectiveness relationships all converge to a single solution given by Equation 2.15.

$$\epsilon = 1 - e^{-NTU} \tag{2.15}$$

In addition, the resistance network, depicted in Figure 36, is reduced to only the solid conduction and fluid-side convection resistances. The thermal conductance *UA* is then given by Equation 2.16.

$$UA = \frac{1}{R_{\mathrm{total}}} = \left(\frac{t}{\lambda_{\mathrm{solid}} A^{\mathrm{base}}} + \frac{1}{\eta_{\mathrm{o}} h A^{\mathrm{interface}}} \right)^{-1} \tag{2.16}$$

Following the definitions of NTU (Equation 2.10 and effectiveness, which in this case reduces to Equation 2.17, the cold plate performance can be evaluated using the same methodology as conventional two-fluid heat exchanger analysis.

$$\epsilon = \frac{\dot{Q}}{\dot{Q}_{\max}} = \frac{C_{\mathrm{f}}(T_{\mathrm{f}}^{\mathrm{in}} - T_{\mathrm{f}}^{\mathrm{out}})}{C_{\min}(T_{\mathrm{s}}^{\mathrm{base}} - T_{\mathrm{f}}^{\mathrm{in}})} \tag{2.17}$$

Deans et al. [52] introduced a new approach for the thermal design of parallel plate heat sinks used in power electronics. The study reinterprets the fin array as a two-stream cross-flow heat exchanger, where the conduction along the fins is treated as a pseudo-fluid stream. An equivalent fin-side heat capacity, C_{s}, is defined based solely on geometry, as shown in Equation 2.18, quantifying energy conduction along the solid structure.

$$C_{\mathrm{s}} = \frac{N \bar{h} P}{m} \frac{\tanh\left(m L_{\mathrm{fin}}\right)}{1 - \dfrac{1}{\cosh\left(m L_{\mathrm{fin}}\right)}} \tag{2.18}$$

Therefore, the heat transfer rate can be written as follows:

$$\dot{Q} = C_{\mathrm{s}}(T_{\mathrm{s}}^{\mathrm{base}} - T_{\mathrm{s}}^{\mathrm{tip}}) = C_{\mathrm{f}}(T_{\mathrm{f}}^{\mathrm{in}} - T_{\mathrm{f}}^{\mathrm{out}}) \tag{2.19}$$

By applying conventional cross-flow (with both fluid mixed) ϵ-NTU relation Equation 2.14, the authors demonstrated that the heat sink can be evaluated as a single thermodynamic unit, rather than as independent fins. The predicted thermal resistance values agreed within $\pm 15\%$ of measurements. Importantly, the study revealed that the optimal fin design does not necessarily correspond to the optimum array design, a component-level insight enabled by the ϵ-NTU analogy.

Building upon this work, Ortega et al. [67] validated the cross-flow effectiveness heat sink model on a liquid-cooled mini-channel cold plate and characterized its performance limits. Their experimental investigation, conducted on a cold plate featuring straight fins, demonstrated good agreement with the thermal resistance model derived from a two-stream cross-flow ϵ-NTU formulation. In comparison, the traditional single-stream ϵ-NTU model adequately predicted the overall thermal resistance, although with increasing deviation at higher flow rates. Furthermore, analysis of the proposed model revealed two asymptotic regimes: a low-NTU convective limit, where the effectiveness approaches zero and thermal resistance is governed primarily by fin-side convection, and a high-NTU limit, where the effectiveness approaches unity and thermal resistance converges to its thermodynamic or advective limit.

3

Heat Exchanger Performance Optimization

Heat exchanger performance optimization has evolved in parallel with the development of increasingly sophisticated heat exchanger designs. Early design practices relied on empirical correlations and trial-and-error procedures. While practical, these methods were time-consuming and did not guarantee optimal solutions. This motivated the development of systematic optimization approaches capable of handling the complex design space defined by numerous geometric and operational parameters. These parameters must be adjusted to balance multiple, often conflicting objectives while satisfying design constraints.

Traditional gradient-based optimization algorithms are inadequate for heat exchanger design problems, as heat exchanger models are typically highly nonlinear, nonconvex, and discontinuous, often involving implicit correlations, numerical solvers, or CFD-based performance evaluations that do not provide analytical gradients. Moreover, the presence of multiple local optima and mixed continuous/discrete design variables causes gradient-based approaches to converge prematurely or produce infeasible solutions [29].

To address these limitations, researchers have adopted stochastic optimization methods, such as genetic algorithms, simulated annealing, and particle swarm optimization. These techniques do not require gradient information and are suitable for nonlinear, multi-objective, and constrained design problems [29]. A major challenge in applying such methods is the computational cost of repeatedly evaluating the heat exchanger performance for thousands of design candidates. Each evaluation requires determining thermalhydraulic performance through numerical simulations that solve the governing flow and energy equations. Many studies therefore employ surrogate-based approaches, in which reduced-order models or regression-based correlations replace detailed CFD simulations, enabling efficient design space exploration while maintaining sufficient predictive accuracy.

Rao et al. [29] published a comprehensive review of studies applying advanced optimization algorithms to heat exchanger design. They examined various techniques, including genetic algorithms, particle swarm optimization, differential evolution, simulated annealing, and teaching-learning-based optimization across different heat exchanger types. The review analyzed how these algorithms optimize key design variables such as tube diameters, baffle spacing, and fin geometry while addressing multiple objectives including cost, weight, and thermal performance. The authors found that stochastic optimization methods consistently outperform traditional trial-and-error approaches by providing more efficient solutions for complex, multi-objective problems. They concluded that

hybrid approaches and the integration of machine learning techniques and artificial intelligence represent the most promising directions for future research in this field.

The maturation of AM has not only enabled novel heat exchanger geometries but also relaxed many of the constraints traditionally imposed by manufacturability considerations. This expanded design freedom has made it feasible to apply adjoint-based and generative design methodologies, which were previously impractical due to the inability to manufacture their complex geometries using conventional techniques. Consequently, AM has made it possible to develop optimization frameworks in which complex geometries generated by topology optimization can be directly fabricated, eliminating the traditional gap between optimal designs and manufacturable solutions.

For instance, Yeranee et al. [30] developed a density-based topology optimization framework integrated with Triply Periodic Minimal Surface (TPMS) lattice infilling to design an advanced cooling channel for gas turbine blade trailing edges. The computational domain, depicted in Figure 38, represented a wedge-shaped trailing-edge passage operating at Reynolds numbers between 10,000 and 30,000. The optimization maximized heat transfer under fixed pumping power while enforcing flow uniformity through flow-rate ratio constraints. A continuous design variable governed the local solid-fluid distribution throughout the domain, with intermediate density values subsequently materialized using Diamond-type TPMS structures, selected for their superior surface-to-volume ratio. The optimized designs were validated against baseline pin fin and uniform lattice configurations through CFD simulations, and manufacturability was confirmed by fabricating a prototype via Laser Powder Bed Fusion in Inconel 718, with geometric fidelity verified through micro-CT scanning.

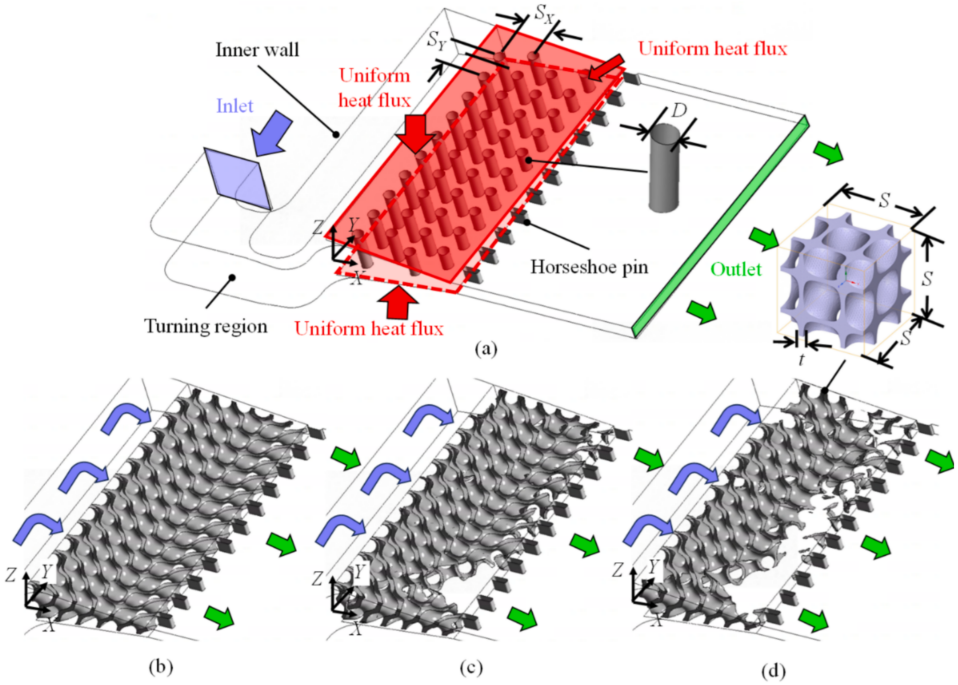

Figure 38: Trailing-edge cooling channels domains for (a) pin fin baseline, (b) uniform, and (c,d) topology-optimized Diamond TPMS lattices, adapted from [30].

Extending beyond academic test cases, the Rolls-Royce cold-plate benchmark, provides an industrially relevant platform to evaluate optimization methodologies for additively manufactured heat exchangers. The same configuration has been successively studied by Raske et al. [31], Daifalla et al. [32], and Chiodi et al. [33], enabling a direct comparison between topology, parametric, and multiscale machine-learning-based approaches.

The test case consists of a cold-plate heat exchanger used as a heat sink for power electronics. As shown in Figure 39, the baseline geometry features a multi-pass serpentine cooling channel with 180° U-bends, where both the flow inlet and outlet are positioned on the same side. The power electronics are represented by six heat cells, three on each side of the cold plate. This serpentine design is commonly used in cold plates due to their specific operational requirements. Unlike conventional heat exchangers, cold plates must maintain the surface contact temperature of each heat cell within the operating tolerances of the power electronics, which requires uniform temperature distribution across all heat cells. However, the 180° U-bends in the serpentine configuration generate high pressure losses due to secondary flows while providing limited heat transfer enhancement.

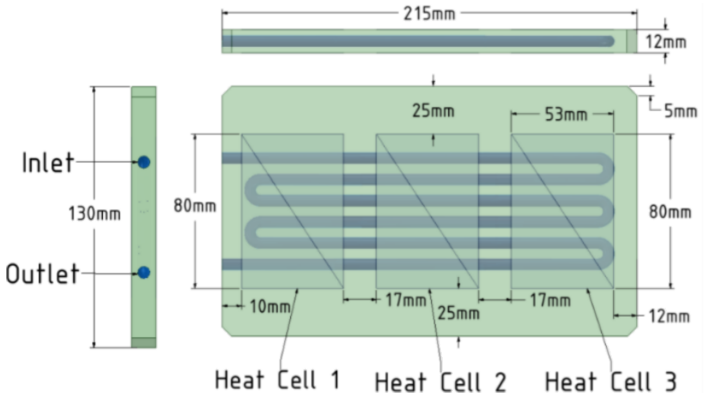

Figure 39: Rolls-Royce cold plate benchmark geometry, adapted from [32].

Raske et al. [31] used fluid topology optimization to redesign this cold-plate geometry, utilizing the commercial solver ToffeeX to generate an optimal flow path. The design domain was treated as a porous medium where an impermeability field was iteratively updated to minimize an objective function comprising weighted pressure losses and thermal energy extraction terms. The optimized geometry was markedly different from the serpentine baseline, featuring microchannels and chaotic flow paths with a fluid splitter at the inlet that effectively directed coolant toward the heated regions. This topology-optimized design achieved significant reductions in both pressure drop and peak temperature.

Both Chiodi et al. [33] and Daifalla et al. [32] adopted a different approach by replacing the serpentine with a channel filled with Gyroid lattice structures, though fundamentally different modeling strategies were applied to optimize the cold-plate performance. Chiodi et al. [33] treated the Gyroid lattice as an equivalent porous medium at the macroscale, characterized by a permeability tensor and heat transfer coefficients. To bridge the scales between the macroscopic flow field and the microscopic lattice geometry, machine learning models were trained on a database of microscale Direct Numerical Simulations performed on periodic Representative Volume Elements of individual lattice unit cells. These models enabled the prediction of closure relationships as nonlinear functions of local geometry and flow conditions, capturing the effects of Reynolds number and lattice parameters on permeability and heat transfer. This multiscale approach enabled topology optimization of the spatial distribution of lattice wall thickness across the domain without explicitly resolving the intricate lattice geometry, significantly reducing computational cost and enabling exploration of a broader design space.

In contrast, Daifalla et al. [32] simulated the full explicit Gyroid geometry using high-fidelity Conjugate Heat Transfer CFD, with meshes exceeding 80 million cells to adequately resolve the flow phenomena within the lattice structure. The substantial computational expense of this approach required a parametric optimization strategy rather than full topology optimization. A Design of

Experiments framework was adopted, where Kriging surrogate models were constructed from an initial set of CFD evaluations to approximate the relationship between design parameters and performance metrics. The NSGA-II algorithm then explored this surrogate model to identify optimal configurations. Eleven geometric parameters were optimized, including cell dimensions (size and aspect ratio along different axes) and thickness variation parameters (minimum and maximum wall thickness across combined planes). Although this high-fidelity method provided accurate predictions of thermal and fluid behavior for specific geometric configurations, the computational burden limited the number of design evaluations compared to the more efficient multiscale framework applied by Chiodi and co-workers.

Part IV

Closure

1

Conclusions

This thesis presented the development and validation of a tool for the thermo-hydraulic design and optimization of additively manufactured compact heat exchangers. This tool integrates information on the flow and heat transfer processes occurring in complex lattice geometries at micro-scale level to predict the performance of actual heat transfer devices adopting those fin or channel topologies, while minimizing computational cost. Its purpose is to support early-stage design and optimization of additively manufactured heat exchangers or cold plates.

The first part of the work focused on the numerical characterization of representative lattice geometries. Four structures were investigated, Pin Fin, BCC, Gyroid, and Diamond. These topologies were chosen to assess both strut-based and surface-based geometries. Their pressure loss and heat transfer characteristics were determined by performing a series of periodic unit cell simulations, which covered a wide range of Reynolds numbers, porosities, as well as two types of working fluids, namely air and a water-glycol mixture. The accuracy of the numerical setup was verified against the predictions of empirical correlations for pin-fin arrays. This systematic simulation campaign produced a consistent dataset that describes how geometry and flow conditions influence the thermal and hydraulic performance of lattice structures.

From this dataset, empirical correlations were derived for the friction factor and the Nusselt number of each topology. The formulation of the correlations was tailored to accurately predict the friction factor and the Nusselt number over laminar, transitional, and turbulent regimes, ensuring a smooth and physically meaningful transition between these regimes. Porosity was introduced in the correlations to capture the actual geometric configuration of the tested topologies. The resulting correlations showed excellent agreement with CFD data, with typical deviations within a few percent ($<10\%$), confirming that the main physical mechanisms were correctly represented.

In the second stage, the developed correlations were implemented into a reduced-order heat exchanger model (HERO) model to predict the thermo-hydraulic performance of an additively manufactured cold plate. Several discretization schemes of the cold plate geometry were assessed: a simple approach treating the plate as a single element, a discretization of the cold plate into a set of control volumes equal in number to the heating zones to account for the streamwise variation of fluid properties, and a detailed discretization of the cold plate geometry to resolve local effects such as non-uniform heating and mass flow distribution. The results obtained with the three modeling approaches were compared against high-fidelity CFD results. The comparison shows that with the use of a few control volumes or the full discretization of the cold plate geometry, the HERO model can predict wall temperatures and pressure drops with reasonable accuracy, while achieving

computational speeds several orders of magnitude faster than CFD simulations.

Lastly, the finely discretized representation of the cold plate enabled the optimization of the porosity distribution along the flow path. The optimization algorithm strategically reduced porosity in high-temperature regions where thermal demands were most critical, while simultaneously increasing porosity in regions where cooling requirements were less stringent. The optimized design achieved a measurable improvement in wall temperature uniformity while preserving the mean wall temperature and overall pressure drop of the uniform-porosity reference.

1.1. Revisiting the Research Questions

To further understand to what extent the research questions were answered, this section revisits each question and discusses how the conducted work addressed them.

RQ 1 - What computational setup allows the characterization of the thermo-hydraulic behavior of lattice structures in a way that captures the effects of geometry, flow regime, and porosity across the entire laminar-turbulent spectrum?

To address this question, the work first explored how to define computational domains and boundary conditions of CFD models suitable for reproducing the periodic characteristics of flow and heat transfer in lattice structures while minimizing simulation cost. The study established that representative unit cell simulations with periodic boundary conditions provide an effective characterization approach. By exploiting the inherent periodicity of lattice structures, a single unit cell subjected to streamwise periodic conditions can reliably capture the flow and heat transfer physics under fully developed conditions while reducing computational requirements. For Pin Fin and BCC configurations, the application of symmetry boundary conditions allowed simulation of only one quarter of the unit cell. For TPMS structures, which contain two topologically equivalent flow channels, simulating a single channel was sufficient.

Since the objective of the study was to characterize the thermohydraulic behavior over a wide range of Reynolds numbers, particular attention was devoted to the selection of an appropriate turbulence model. Given the large number of simulations required, RANS models represented an obvious compromise between computational cost and accuracy. Although the literature on turbulent flow through lattice structures does not indicate a universally accepted RANS model, the $k-\omega$ SST formulation was selected because of its proven robustness in internal flows and its ability to provide reliable predictions in low-Reynolds-number regimes.

Although the periodic computational setup is well suited for characterizing fully developed laminar and turbulent flows, its applicability in the transitional range requires careful interpretation. Flow transition is inherently local and involves the spatial development of turbulent instabilities. Consequently, the flow transition is modeled in an effective, averaged sense rather than resolved explicitly. Therefore, predictions in the transitional range are expected to exhibit higher uncertainty than in fully laminar or turbulent regimes.

All things considered, the reliability of the computational setup was verified against the predictions of widely adopted pin fin correlations. The friction factor and Nusselt number results showed good agreement with the predictions of these correlations, increasing the confidence that both the modeling assumptions and the numerical setup were appropriate for the characterization study.

RQ 2 - What generalized relationships can accurately describe the friction factor and Nusselt number of lattice structures across varying geometries and flow regimes?

RQ 2.1 - What is the most suitable characteristic length scale for the non-dimensionalization of thermo-hydraulic performance data to develop general correlations?

The development of these generalized relationships began by examining which characteristic length scale is most suitable as similarity parameter for the thermo-hydraulic data obtained for different porosities and flow regimes. The superficial definition of hydraulic diameter was the most effective option to correlate friction factor data, whereas the pore-based definition is more suitable to reduce the dimensionality of the heat transfer data. Considering this, porosity is treated explicitly in the friction factor correlations, whereas its contribution is implicit in the pore-based quantities used for the Nusselt number correlations.

RQ 2.2 - Which correlation expressions can accurately capture the trend in friction factor and Nusselt number from laminar to turbulent flow, ensuring also smooth and physically meaningful trends over the transitional regime?

To ensure smooth transitions between regimes, a sigmoid-type weighting function was used to smoothly transition between the laminar and turbulent regimes, replacing traditional piecewise fits. This formulation accurately reproduces the shift in flow behavior from the viscous-dominated regime (laminar flow) to the inertial-dominated regime (turbulent flow) without introducing discontinuities and ensuring physical consistency across the full Reynolds number range. The resulting correlation for the friction factor combined the Ergun-type expression for the laminar regime with a Blasius-type dependence for the turbulent regime. Conversely, the Nusselt number was correlated using a single Dittus-Boelter-type power law.

RQ 2.3 - How do the proposed correlations compare to existing empirical models in terms of predictive capability and generalization?

In comparison with existing empirical models for lattice structures, the obtained correlations showed significantly broader validity. They are applicable over a wider range of Reynolds numbers than typically considered for correlation development, as well as across broad ranges of porosities and Prandtl numbers. The proposed correlations were derived from a comprehensive parametric study covering porosities from 25% to 95%, Reynolds numbers from 100 to $100{,}000$, and Prandtl numbers from 0.7 to 15, representative of gases to commonly used liquid coolants. This broad validity range makes the developed correlations applicable to different thermal management applications, such as liquid-cooled heat sinks, air-cooled heat exchangers, and turbine blade cooling.

Almost every correlation achieved an R^2 value exceeding 0.99, demonstrating an excellent statistical fit. The friction factor predictions fell within $\pm 10\%$ of most CFD simulations used for fitting, while Nusselt number predictions remained within $\pm 20\%$, confirming that the derived mathematical relationships and the adopted data reduction can reliably capture performance trends. This level of accuracy is well aligned with expectations based on traditional correlations reported in the literature. However, comparing the correlation predictions with recent lattice studies is not straightforward. Experimental investigations often involve surface roughness from manufacturing processes, which affects the performance with respect to geometries with smooth surfaces. In addition, numerical studies employ different modeling assumptions, boundary conditions, and data reduction methods, making cross-comparison of correlation predictions difficult.

RQ 3 - How can the derived correlations be integrated into a reduced-order model to accurately predict the performance of heat exchangers?

RQ 3.1 - What are the limitations of simplified reduced-order approaches in predicting the thermo-hydraulic performance of heat-exchangers?

The derived correlations were integrated into heat exchanger preliminary design models of increasing discretization complexity. In particular, three versions of the model were developed differing in the level of detail in which the heat transfer geometry is discretized. The lumped approach, although computationally efficient, led to an overprediction of the wall temperatures and pressure drops because the variation in temperature and consequently in the thermophysical properties of the cooling medium is not accounted for in the model. The segmented approach addressed this limitation by dividing the flow path into six large control volumes, allowing local updates of the working fluid thermophysical properties along the streamwise direction. This significantly improved agreement with CFD results. The most complex version, based on a detailed discretization of the geometry, features similar accuracy, though accounts also for non-uniform heating conditions.

Despite the benefits of these discretized versions of the reduced-order model, the heat transfer and hydraulic problems in each control volume are still solved using an averaged 1D approach. The three-dimensionality of the flow and the conjugate heat transfer problems is therefore not resolved in detail. Consequently, transverse heat transfer and local flow maldistribution across different lattice channels cannot be predicted with confidence. This limitation was evident in the analysis of the optimal pin fin configuration. The reduced-order model prediction significantly overestimated the pressure losses estimated by the CFD simulation. This was attributed to the dependence of the structure dependence to the direction of the incoming flow, which was not considered in either the correlation development or the HERO model formulation. The correlations were developed assuming unidirectional flow, but the U-bend in the cold plate geometry forced a change in flow direction.

Moreover, local phenomena, such as entrance and discharge effects cannot intrinsically be captured. If these effects prove significant, they should be addressed through dedicated models. The flexibility and modularity of the design tool ensures that such local loss models can be easily implemented and calibrated if necessary.

In summary, due to these limitations, the model is suitable for preliminary design, parametric studies, and design-space exploration, while detailed assessment requires higher-fidelity conjugate heat transfer simulations as well as experiments.

RQ 3.2 - What are the trade-offs in computational time, memory requirements, and solution accuracy between the reduced-order model and high-fidelity CFD analysis?

Lattice-based heat exchangers exhibit inherently complex geometries with small-scale features that must be resolved using fine spatial discretization to accurately capture local flow and heat transfer phenomena. This requirement leads to dense meshes; for the cold plate test case considered here, the resulting mesh contains approximately 80 million elements. Beyond mesh size alone, this geometric complexity also significantly complicates geometry preparation and mesh generation, making these steps time- and resource-intensive within the CFD analysis workflow. Moreover, these operations must be repeated for each design solution to be analyzed. Computational demands become, then, significant, as geometry, mesh, and solution files require large memory allocations. Consequently, the CFD simulations reported in this work were executed on a 196-core cluster, with each simulation still requiring several hours to converge.

In contrast, individual simulations using the reduced-order model are completed in seconds, require negligible memory resources, and generate an output file of limited size. The resulting difference in computational cost is not meaningfully comparable to that of CFD analyzes, as the reduced-order model does not represent a cheaper or faster implementation of the same equations of the CFD model. Its computational efficiency makes the reduced-order framework particularly well-suited for design exploration contexts where the computational costs of the CFD simulations would be prohibitive. In optimization studies or preliminary design screening, where hundreds or thousands of configurations may require assessment, the reduced-order model enables parametric analyzes at a scale that would be impractical with CFD simulations. On the other hand, CFD provides sufficient physical fidelity to validate early-stage design results and support further development toward higher technology readiness levels.

When the reduced-order model results were verified against CFD simulations, they demonstrated excellent alignment, with deviations generally below 10% for both thermal and hydraulic performance metrics. The demonstrated predictive capability of the reduced-order framework, achieved at negligible computational cost, provides the necessary confidence to use it as a practical preliminary design tool for the next-generation of compact heat exchangers.

1.2. Closing Remarks

The overall research objective was to establish a computationally efficient yet physically grounded framework that closes the gap between the microscale thermo-fluid dynamics of lattice geometries and the component-level performance of additively manufactured heat exchangers. This goal was successfully achieved through the formulation of performance correlations and their integration into a reduced-order model capable of predicting heat exchanger performance with high accuracy at a fraction of the computational cost of CFD simulations. The model demonstrates that complex lattice-based heat exchangers can be effectively characterized and optimized using lower-order approaches, offering a powerful tool for early-stage thermal design and design-space exploration. This framework thus enables rapid design-space exploration that takes full advantage of the geometric flexibility offered by additive manufacturing for next-generation compact heat exchanger applications.

2

Future Work Recommendations

While the proposed methodology proved to be effective and accurate for the thermo-hydraulic characterization and modeling of additively manufactured heat exchanger cores, several aspects remain open for further development, as explained in the following recommendations.

Experimental validation of the proposed correlations.

While the correlations derived in this work showed strong agreement with CFD data, their predictive capability remains inherently tied to the assumptions underlying numerical modeling. A natural and necessary extension of the present research is therefore the experimental validation of the proposed friction factor and Nusselt number correlations. Dedicated experimental campaigns conducted on additively manufactured lattice samples, spanning representative ranges of Reynolds number, porosity, and working fluids, would provide a critical benchmark to quantify model uncertainty and identify potential systematic deviations.

However, such validation is non-trivial. Additively manufactured metallic samples are typically characterized by significant surface roughness and geometric imperfections, which would compromise a direct and fair comparison with the smooth geometries investigated numerically in this study. Two complementary strategies could address this mismatch. The first consists in scaling up the lattice geometries such that surface roughness effects become negligible relative to the hydraulic diameter ($R_a << D_h$). The second option involves the use of additively manufactured technical ceramics, which exhibit much lower surface roughness and better surface finish than metallic AM processes. Experimental confirmation using either approach would strengthen the confidence in the proposed correlations and support its adoption in design workflows.

Extension of the numerical dataset to additional geometries and geometrical parameters.

The current database includes a limited set of lattice morphologies, such as gyroid, diamond, and BCC and only the porosity of the structures was varied to generate the numerical dataset. This restricts the generality of the correlations. Including additional geometries, such as other versions of strut or surface-based lattices enumerated in the literature review, as well as anisotropic variations of existing unit cells (e.g. stretched or compressed along specific axes) would expand the design space and enable a more comprehensive description of the structure-property relationships. This extension would also require the development of anisotropy-aware models, improving predictive accuracy for components in which flow changes direction.

Inclusion of surface roughness effects in the performance characterization.

The present methodology assumes topologies with smooth surfaces . However, surface roughness, inherently resulting from the additive manufacturing process, can significantly influence both frictional losses and convective heat transfer. Capturing these effects is essential to design devices for practical applications, especially for metal AM processes where surface finishing is often limited. A future study could incorporate controlled roughness levels in CFD simulations or experimental campaigns to quantify the sensitivity of friction and heat transfer coefficients to roughness metrics such as the average surface roughness R_a or the equivalent sand-grain roughness k_s. The resulting correlations would enable the design tool to predict performance under as-built conditions.

Application of the tool to two-fluid heat exchanger design problem.

The reduced-order framework developed in this work was applied to single-fluid cold plates. An important next step is extending it to two-fluid heat exchangers. By incorporating the lattice-based friction and heat transfer correlations into a two-fluid $\epsilon - NTU$ model, the framework could support preliminary design and performance evaluation of compact heat exchangers with additively manufactured cores. This would enable the analysis of recuperators, intercoolers, and other configurations where compactness and high surface area are essential. This development would significantly expand the applicability of the tool, facilitating early-stage design and optimization of advanced thermal management systems.

References

[1] *Non-CO2 Emissions and Effects*. IATA. URL: https://www.iata.org/contentassets/726b8a2559ad48fe9decb6f2534549a6/non-co2-emissions-and-effects.pdf (visited on 09/29/2025).

[2] H. Ritchie. "What share of global CO emissions come from aviation?" In: *Our World in Data* (2024). URL: https://ourworldindata.org/global-aviation-emissions (visited on 09/29/2025).

[3] *Non-CO2 Aviation Emissions*. IATA. URL: https://www.iata.org/contentassets/5499da2b3b7d46b3b13be4dad54a9689/policy-position-non-co2-aviation-emissions.pdf (visited on 09/29/2025).

[4] R.G. Sanchez and T.K. Walker III. "Aviation Non-CO_2 Effects - Strategies for Minimizing Contrail Climate Impact". In: *Clean Air Task Force* (2025). URL: https://www.catf.us/resource/aviation-non-co2-effects-strategies-for-minimizing-contrail-climate-impact/.

[5] *Paris Agreement*. UNFCCC. URL: https://unfccc.int/process-and-meetings/the-paris-agreement (visited on 09/29/2025).

[6] S.L. Schnulo et al. "Assessment of the Impact of an Advanced Power System on a Turboelectric Single-Aisle Concept Aircraft". In: *AIAA Propulsion and Energy 2020 Forum*. American Institute of Aeronautics and Astronautics, Aug. 2020. ISBN: 978-1-62410-602-6. DOI: 10.2514/6.2020-3548.

[7] C. Lents et al. "Parallel Hybrid Gas-Electric Geared Turbofan Engine Conceptual Design and Benefits Analysis". In: July 2016. DOI: 10.2514/6.2016-4610.

[8] K.A. Thole, S.P. Lynch, and A.J. Wildgoose. "Review of advances in convective heat transfer developed through additive manufacturing". In: vol. 53. Advances in Heat Transfer. Elsevier, 2021, pp. 249–325. DOI: https://doi.org/10.1016/bs.aiht.2021.06.004.

[9] C. Pan, Y. Han, and J. Lu. "Design and Optimization of Lattice Structures: A Review". In: *Applied Sciences* 10.18, 6374 (Sept. 2020). ISSN: 2076-3417. DOI: 10.3390/app10186374.

[10] I. Kaur and P. Singh. "Effects of inherent surface roughness of additively manufactured lattice frame material on flow and thermal transport". In: *International Journal of Heat and Mass Transfer* 209, 124077 (Aug. 2023). ISSN: 00179310. DOI: 10.1016/j.ijheatmasstransfer.2023.124077.

[11] N. Castelli et al. "Experimental Analysis of Additive Manufactured Latticework Coupons". In: Boston, Massachusetts, USA: American Society of Mechanical Engineers, June 2023, V07BT13A010. ISBN: 978-0-7918-8701-1. DOI: 10.1115/GT2023-102445.

[12] T.M. Corbett and K.A. Thole. "Large eddy simulations of kagome and body centered cubic lattice cells". In: *International Journal of Heat and Mass Transfer* 218, 124808 (Jan. 2024). ISSN: 00179310. DOI: 10.1016/j.ijheatmasstransfer.2023.124808.

[13] D. Liang et al. "Investigating the effect of element shape of the face-centered cubic lattice structure on the flow and endwall heat transfer characteristics in a rectangular channel". In: *International Journal of Heat and Mass Transfer* 153, 119579 (June 2020). ISSN: 00179310. DOI: 10.1016/j.ijheatmasstransfer.2020.119579.

[14] A. Lorenzon et al. "Experimental investigation of heat transfer and pressure losses across staggered Body Centered cubic arrays fabricated by Laser Powder Bed Fusion". In: *Applied Thermal Engineering* 227, 120381 (2023). ISSN: 1359-4311. DOI: https://doi.org/10.1016/j.applthermaleng.2023.120381.

[15] S.S. Rathore et al. "Flow Characterization in Triply Periodic Minimal Surface (TPMS)-Based Porous Geometries: Part 1Hydrodynamics". In: *Transport in Porous Media* 146.3 (Feb. 2023), pp. 669–701. ISSN: 0169-3913, 1573-1634. DOI: 10.1007/s11242-022-01880-7.

[16] S. Piedra, A. Gómez-Ortega, and J. Pérez-Barrera. *Characterizing Flow Through Tpms Structures Using Darcy-Forchheimer Model*. 2023. DOI: 10.2139/ssrn.4470062.

[17] L.G. Ornelas-Ramón et al. "Computational analysis and engineering modeling for the heat transfer and fluid flow through the gyroid TPMS structure". In: *Applied Thermal Engineering* 268, 125865 (June 2025). ISSN: 13594311. DOI: 10.1016/j.applthermaleng.2025.125865.

[18] S.S. Rathore et al. *Flow Characterization in Triply-Periodic-Minimal-Surface (TPMS) based Porous Geometries: Part 2 Heat Transfer*. Jan. 2023. DOI: 10.21203/rs.3.rs-2427715/v1.

[19] F. Torri et al. "Evaluation of TPMS Structures for the Design of High Performance Heat Exchangers". In: Capri, Italy, Aug. 2023, 2023-24-0125. DOI: 10.4271/2023-24-0125.

[20] K. Yan et al. *Numerical Investigation into Thermal and Hydraulic Characteristics of Triply Periodic Minimal Surface-Based Heat Exchangers*. 2023. DOI: 10.2139/ssrn.4336822.

[21] S. Samson, P. Tran, and P. Marzocca. "Design and modelling of porous gyroid heatsinks: Influences of cell size, porosity and material variation". In: *Applied Thermal Engineering* 235, 121296 (Nov. 2023). ISSN: 13594311. DOI: 10.1016/j.applthermaleng.2023.121296.

[22] J. Wang et al. "Investigation on flow and heat transfer in various channels based on triply periodic minimal surfaces (TPMS)". In: *Energy Conversion and Management* 283, 116955 (May 2023). ISSN: 01968904. DOI: 10.1016/j.enconman.2023.116955.

[23] G. Brambati, M. Guilizzoni, and S. Foletti. "Convective heat transfer correlations for Triply Periodic Minimal Surfaces based heat exchangers". In: *Applied Thermal Engineering* 242, 122492 (Apr. 2024). ISSN: 13594311. DOI: 10.1016/j.applthermaleng.2024.122492.

[24] B.W. Reynolds et al. "Characterisation of Heat Transfer within 3D Printed TPMS Heat Exchangers". In: *International Journal of Heat and Mass Transfer* 212, 124264 (Sept. 2023). ISSN: 00179310. DOI: 10.1016/j.ijheatmasstransfer.2023.124264.

[25] W. Tang et al. "Analysis on the convective heat transfer process and performance evaluation of Triply Periodic Minimal Surface (TPMS) based on Diamond, Gyroid and Iwp". In: *International Journal of Heat and Mass Transfer* 201, 123642 (Feb. 2022). ISSN: 00179310. DOI: 10.1016/j.ijheatmasstransfer.2022.123642.

[26] W. Tang et al. *Experimental Investigation on the Convective Heat Transfer Performance of Five Triply Periodic Minimal Surfaces (Tpms): Gyroid, Diamond, Iwp, Primitive, and Fischer-Koch-S*. 2023. DOI: 10.2139/ssrn.4648952.

[27] Z. Zou et al. "Experimental investigation of the performance of an Industrial-Grade Schwartz-D heat exchanger". In: *Applied Thermal Engineering* 270, 126243 (July 2025). ISSN: 13594311. DOI: 10.1016/j.applthermaleng.2025.126243.

[28] A.G. Caket et al. "Recent studies on 3D lattice metal frame technique for enhancement of heat transfer: Discovering trends and reasons". In: *Renewable and Sustainable Energy Reviews* 167, 112697 (Oct. 2022). ISSN: 13640321. DOI: 10.1016/j.rser.2022.112697.

[29] R. V. Rao et al. "Design Optimization of Heat Exchangers with Advanced Optimization Techniques: A Review". In: *Archives of Computational Methods in Engineering* 27.2 (2020), pp. 517–548. DOI: 10.1007/s11831-019-09318-y.

[30] K. Yeranee et al. "Thermal Performance Enhancement for Gas Turbine Blade Trailing Edge Cooling with Topology-Optimized Printable Diamond TPMS Lattice". In: *International Journal of Heat and Fluid Flow* 110, 109649 (2024). ISSN: 0142-727X. DOI: 10.1016/j.ijheatfluidflow.2024.109649.

[31] N. Raske et al. "Thermal Management for Electrification in Aircraft Engines: Optimization of Coolant System". In: vol. Volume 6B: Heat Transfer General Interest/Additive Manufacturing Impacts on Heat Transfer; Internal Air Systems; Internal Cooling. Turbo Expo. June 2022, V06BT13A013. DOI: 10.1115/GT2022-82538.

[32] E. Daifalla et al. "Multi-Disciplinary Optimization of Gyroid Topologies for a Cold Plate Heat Exchanger Design". In: vol. Volume 13: Heat Transfer: General Interest / Additive Manufacturing Impacts on Heat Transfer; Wind Energy. Turbo Expo. June 2024, V013T13A038. DOI: 10.1115/GT2024-128603.

[33] A. Chiodi et al. "Multidisciplinary Optimisation of Additive Manufactured Heat Exchangers for Aeronautical Applications". In: vol. Volume 13: Heat Transfer: General Interest / Additive Manufacturing Impacts on Heat Transfer; Wind Energy. Turbo Expo. June 2024, V013T13A026. DOI: 10.1115/GT2024-126786.

[34] H.A. Schwarz. *Gesammelte Mathematische Abhandlungen. Erster Band*. 1st ed. Berlin, Heidelberg: Springer-Verlag Berlin Heidelberg, 1890. DOI: 10.1007/978-3-642-50665-9.

[35] A.H. Schoen. *Infinite Periodic Minimal Surfaces without Self-Intersections*. NASA Technical Note NASA-TN-D-5541. Cambridge, MA, United States: NASA Electronics Research Center, May 1970. URL: https://ntrs.nasa.gov/citations/19700020472.

[36] *nTop*. Version 5. nTop Inc. 2025. URL: https://ntop.com.

[37] *Fluent Theory Guide*. Version 2023 R2. ANSYS, Inc. Canonsburg, PA, 2023. URL: https://www.ansys.com/products/fluids/ansys-fluent.

[38] P. J. Roache. "Perspective: A Method for Uniform Reporting of Grid Refinement Studies". In: *Journal of Fluids Engineering* 116.3 (Sept. 1994), pp. 405–413. ISSN: 0098-2202. DOI: 10.1115/1.2910291.

[39] *PyFluent documentation*. Version 0.35.1. PyAnsys. 2025. URL: https://fluent.docs.pyansys.com/.

[40] D. E. Metzger, W. B. Shepard, and S. W. Haley. "Row Resolved Heat Transfer Variations in Pin-Fin Arrays Including Effects of Non-Uniform Arrays and Flow Convergence". In: *Proceedings of the 31st ASME International Gas Turbine Conference and Exhibit*. ASME. Duesseldorf, West Germany, June 1986, p. 9.

[41] J. Ostanek. "Flowfield and Heat Transfer Measurements in Staggered Pin-Fin Arrays". Doctor of Philosophy Dissertation. University Park, PA, USA: The Pennsylvania State University, Mar. 2012.

[42] M. Chyu, S. Siw, and H. Moon. "Effects of Height-to-Diameter Ratio of Pin Element on Heat Transfer From Staggered Pin-Fin Arrays". In: vol. 3. Jan. 2009. DOI: 10.1115/GT2009-59814.

[43] W.M. Kays and A.L. London. *Compact heat exchangers*. McGraw-Hill,New York, NY, Dec. 1983.

[44] C. F. Colebrook and C. M. White. "Experiments with fluid friction in roughened pipes". In: *Proc. R. Soc. Lond.* 161 (Aug. 1937), pp. 367–387. DOI: 10.1098/rspa.1937.0150.

[45] F.A. Morrison. "Data Correlation for Friction Factor in Smooth Pipes". URL: https://pages.mtu.edu/~fmorriso/DataCorrelationForSmoothPipes2013.pdf (visited on 09/05/2025).

[46] S. Ergun. "Fluid Flow Through Packed Columns". In: *Chemical Engineering Progress* 48.2 (1952), p. 89. URL: https://cir.nii.ac.jp/crid/1572261550410403712.

[47] H. Blasius. "Das Aehnlichkeitsgesetz bei Reibungsvorgängen in Flüssigkeiten". In: *Mitteilungen über Forschungsarbeiten auf dem Gebiete des Ingenieurwesens: insbesondere aus den Laboratorien der technischen Hochschulen*. Berlin, Heidelberg: Springer Berlin Heidelberg, 1913, pp. 1–41. ISBN: 978-3-662-02239-9. DOI: 10.1007/978-3-662-02239-9_1.

[48] L.F. Moody. "Friction Factors for Pipe Flow". In: *Transactions of the American Society of Mechanical Engineers* 66.8 (Dec. 2022), pp. 671–678. ISSN: 0097-6822. DOI: 10.1115/1.4018140.

[49] R. E. Hicks. "Pressure Drop in Packed Beds of Spheres". In: *Industrial & Engineering Chemistry Fundamentals* 9.3 (1970), pp. 500–502. DOI: 10.1021/i160035a020.

[50] F. W. Dittus and L.M.K. Boelter. "Heat Transfer in Automobile Radiators of the Tubular Type". In: *Publications in Engineering* 2 (1930), p. 443.

[51] D.W. Copeland. "Fundamental Performance Limits of Heatsinks". In: *Journal of Electronic Packaging* 125.2 (June 2003), pp. 221–225. ISSN: 1043-7398. DOI: 10.1115/1.1569262. URL: https://doi.org/10.1115/1.1569262.

[52] J. Deans et al. "The Use of Effectiveness Concepts to Calculate the Thermal Resistance of Parallel Plate Heat Sinks". In: *Heat Transfer Engineering* 27.5 (June 2006), pp. 56–67. ISSN: 0145-7632, 1521-0537. DOI: 10.1080/01457630600560643.

[53] K. Sankaranarayanan et al. "Architectural implications of spatial thermal filtering". In: *Integration* 46.1 (2013), pp. 44–56. ISSN: 0167-9260. DOI: https://doi.org/10.1016/j.vlsi.2011.12.002.

[54] N. Casini, L. Mazzei, and R. Da Soghe. "Numerical Analysis of Convective Heat Transfer Processes and Performance Assessment of Lattice and Triply Periodic Minimal Surface Geometries". In: vol. Volume 13: Heat Transfer: General Interest / Additive Manufacturing Impacts on Heat Transfer; Wind Energy. Turbo Expo. June 2024, V013T13A041. DOI: 10.1115/GT2024-129097.

[55] D. Rani et al. "Genetic Algorithms and Their Applications to Water Resources Systems". In: *Metaheuristics in Water, Geotechnical and Transport Engineering*. Elsevier, 2013, pp. 43–78. DOI: 10.1016/B978-0-12-398296-4.00003-9.

[56] A. Hassanat et al. "Choosing Mutation and Crossover Ratios for Genetic Algorithms-A Review with a New Dynamic Approach". In: *Information* 10.12, 390 (2019). DOI: 10.3390/info10120390.

[57] J. Blank and K. Deb. "pymoo: Multi-Objective Optimization in Python". In: *IEEE Access* 8 (2020), pp. 89497–89509.

[58] R.K. Shah and D.P. Sekuli. *Fundamentals of Heat Exchanger Design*. Hoboken, NJ, USA: John Wiley & Sons, Inc., 2003. ISBN: 9780471321712. DOI: 10.1002/9780470172605. URL: https://doi.org/10.1002/9780470172605.

[59] S. Kakaç, H. Liu, and A. Pramuanjaroenkij. *Heat Exchangers: Selection, Rating, and Thermal Design*. 4th ed. CRC Press, 2020. DOI: 10.1201/9780429469862.

[60] V. Gnielinski. "New equations for heat and mass transfer in the turbulent flow in pipes and channels". In: *NASA STI/Recon Technical Report A* 41.1 (Jan. 1975), pp. 8–16.

[61] R.M. Manglik and A.E. Bergles. "Heat transfer and pressure drop correlations for the rectangular offset strip fin compact heat exchanger". In: *Experimental Thermal and Fluid Science* 10.2 (1995). Aerospace Heat Exchanger Technology, pp. 171–180. ISSN: 0894-1777. DOI: https://doi.org/10.1016/0894-1777(94)00096-Q.

[62] I. Kaur et al. "Thermal-hydraulic performance of additively manufactured lattices for gas turbine blade trailing edge cooling". In: *Applied Thermal Engineering* 211, 118461 (July 2022). ISSN: 13594311. DOI: 10.1016/j.applthermaleng.2022.118461.

[63] E.R. Neovius. *Bestimmung zweier speciellen periodischen Minimalflächen*. Helsingfors, 1883.

[64] T. Femmer, A.J.C. Kuehne, and M. Wessling. "Estimation of the structure dependent performance of 3-D rapid prototyped membranes". In: *Chemical Engineering Journal* 273 (Aug. 2015), pp. 438–445. ISSN: 13858947. DOI: 10.1016/j.cej.2015.03.029.

[65] VDI e. V., ed. *VDI Heat Atlas*. 2nd ed. VDI-Buch. Springer Berlin, Heidelberg, 2010. ISBN: 978-3-540-77877-6. DOI: 10.1007/978-3-540-77877-6.

[66] H.A. Navarro and L.C. Cabezas-Gómez. "Effectiveness-ntu computation with a mathematical model for cross-flow heat exchangers". In: *Brazilian Journal of Chemical Engineering* 24.4 (Dec. 2007), pp. 509–521. ISSN: 0104-6632. DOI: 10.1590/S0104-66322007000400005.

[67] A. Ortega et al. "Determination of the Thermal Performance Limits for Single Phase Liquid Cooling Using an Improved Effectiveness-NTU Cold Plate Model". In: Garden Grove, California, USA: American Society of Mechanical Engineers, Oct. 2022, V001T01A008. ISBN: 978-0-7918-8655-7. DOI: 10.1115/IPACK2022-97421.

A

Periodic Flow Modeling

This appendix details the mathematical formulation used by Ansys Fluent [37] for streamwise-periodic flow simulations, providing the theoretical foundation for the computational methodology used in the thermo-hydraulic characterization of the lattice structures, in section 2.1.

Streamwise-periodic flow occurs when both the geometry and the resulting flow field repeat in a spatially periodic manner along the primary flow direction. The periodicity assumption permits reducing the computational domain to a single representative volume element, with appropriate boundary conditions ensuring equivalence to the full extended geometry.

In particular, the periodic formulation in Ansys Fluent requires:

- Incompressible flow;
- Constant thermophysical properties (density, viscosity, thermal conductivity, heat capacity);
- Transport properties may vary spatially in a periodic manner (permitting periodic turbulent flows with position-dependent effective properties);
- No net mass addition across periodic boundaries or volumetric source terms;
- Pressure-based solver (required for all thermal cases);
- Uniform thermal boundary condition types across all walls (either all constant temperature or all specified heat flux, though adiabatic walls may be combined with either);
- For constant temperature walls: all walls may be at the same temperature, with no viscous heating or volumetric heat sources allowed;
- For heat flux walls: non-uniform flux distributions are allowed across different boundaries;
- Solid regions, if present, must not intersect periodic planes.

These constraints ensure that the periodic module accurately represents the behavior of the infinite repeated component.

For a domain with periodicity vector $\vec{L}$, the velocity field satisfies:

$$\vec{u}(\vec{r}) = \vec{u}(\vec{r} + \vec{L}) \tag{A.1}$$

This spatial periodicity allows a single module to completely characterize the flow kinematics. However, the pressure field itself is not periodic. Instead, the streamwise pressure gradient drives the

flow, with each module experiencing an identical prescribed pressure drop:

$$\Delta p = p(\vec{r}) - p(\vec{r} + \vec{L}) \tag{A.2}$$

This constant pressure drop per module serves as the fundamental driving parameter. The problem can be formulated by either specifying Δp directly or prescribing the mass flow rate, with the solver determining the corresponding pressure gradient required to sustain that flow.

When walls are maintained at constant temperature T_{w}, as in the present study, the physical temperature field $T(\vec{r})$ cannot be periodic, as the fluid temperature necessarily increases as it absorbs heat while progressing downstream. To preserve a periodic formulation, Fluent introduces a scaled temperature:

$$\theta(\vec{r}) = \frac{T(\vec{r}) - T_{\mathsf{w}}}{T_{\mathsf{b}}(\vec{r}) - T_{\mathsf{w}}} \tag{A.3}$$

This normalized variable θ is spatially periodic, even though $T(\vec{r})$ is not. The bulk temperature is defined as the mass-flow-weighted average over the cross-section:

$$T_{\mathsf{b}}(\vec{r}) = \frac{\int_A T\,\rho|\vec{v}\cdot\vec{n}|\,dA}{\int_A \rho|\vec{v}\cdot\vec{n}|\,dA} \tag{A.4}$$

where the integration is performed over the flow cross-section A at position $\vec{r}$. The bulk temperature assigned at the inlet periodic plane serves as the reference for normalization. This transformation allows for a periodic thermal field solution capturing the physical temperature rise through the relationship between θ, T_{b}, and T_{w}.

B

Confidential: Correlation Details

This appendix contains supplementary confidential information to the correlation derivation process and is not available in the public version.

C

Discretized Reduced-Order Model

This appendix includes the analytical derivations of the discretized reduced-order model described in subsection 2.2.2.

C.1. End Plate Conduction Problem

Considering a thin wall of thickness t and thermal conductivity λ_{s}, subjected to a spatially varying heat flux $\dot{q}_{\mathrm{top}}(x,y)$ on its upper surface and to a convective boundary condition with a uniform heat transfer coefficient $\bar{h}$ on its bottom surface (interface) exposed to a fluid at a bulk temperature T_∞.

Under the thin-wall approximation, temperature variations through the thickness are neglected, and the wall temperature can be represented by its thickness-averaged value $T(x,y)$. Assuming steady-state conditions, the Fourier's heat transfer equation gives

$$-\lambda_{\mathrm{s}} t\,\nabla^2 T(x,y) = \dot{q}_{\mathrm{top}}(x,y) - \dot{q}_{\mathrm{bot}}(x,y), \tag{C.1}$$

where $\dot{q}_{\mathrm{bot}}(x,y)$ represents the heat flux at the bottom of the end plate.

At this bottom interface, heat transfer to the fluid is governed by Newton's law of cooling:

$$\dot{q}_{\mathrm{bot}}(x,y) = \bar{h}\,(T(x,y) - T_\infty). \tag{C.2}$$

Defining the temperature relative to the fluid bulk temperature, $\theta(x,y) = T(x,y) - T_\infty$, and substituting Equation C.2 into Equation C.1, one obtains

$$-\lambda_{\mathrm{s}} t\,\nabla^2 \theta(x,y) = q_{top}(x,y) - \bar{h}\,\theta(x,y). \tag{C.3}$$

To solve Equation C.3 efficiently, following the approach described in [53], a two-dimensional Fourier transform is applied using the following definitions

$$\widehat{f}(k_x,k_y) = \mathcal{F}(f(x,y)) = \iint_{-\infty}^{\infty} f(x,y)\, e^{-i(k_x x + k_y y)}\, dx\, dy, \tag{C.4}$$

$$f(x,y) = \mathcal{F}^{-1}(\widehat{f}(k_x,k_y)) == \frac{1}{(2\pi)^2}\iint_{-\infty}^{\infty} \widehat{f}(k_x,k_y)\, e^{i(k_x x + k_y y)}\, dk_x\, dk_y, \tag{C.5}$$

where k_x and k_y are the spatial wavenumbers, and $K = \sqrt{k_x^2 + k_y^2}$ is the total wavenumber magnitude. Using the property $\mathcal{F}\{\nabla^2\theta\} = -K^2\widehat{\theta}$, the Fourier transform of Equation C.3 yields

$$k_s t\, K^2\, \widehat{\theta}(k_x,k_y) = \widehat{q}_{top}(k_x,k_y) - \bar{h}\,\widehat{\theta}(k_x,k_y). \tag{C.6}$$

Rearranging gives

$$\widehat{\theta}(k_x,k_y) = \frac{1}{\lambda_s t\, K^2 + \bar{h}}\, \widehat{q}_{\mathrm{top}}(k_x,k_y). \tag{C.7}$$

From Equation C.2, the heat flux bottom surface in the frequency domain is $\widehat{q}_{interface} = \bar{h}\,\widehat{\theta}$. Substituting in Equation C.7 yields

$$\widehat{q}_{\mathrm{bot}}(k_x,k_y) = \underbrace{\frac{\bar{h}}{\lambda_s t\, K^2 + \bar{h}}}_{H(K)}\, \widehat{q}_{\mathrm{top}}(k_x,k_y), \tag{C.8}$$

where $H(K)$ represents the spatial attenuation of the surface heat flux pattern as it propagates through the cold plate end wall to the bottom interface. This transfer function $H(K)$ quantifies how effectively lateral heat conduction within the wall smooths out spatial variations in the applied heat flux. For spatially uniform heating, $K = 0 \rightarrow H(0) = 1$, meaning that the heat flux applied on the top surface is directly transferred to the end plate bottom interface. On the other hand, for spatially varying heating, as K increases, $H(K) \rightarrow 0$, which means that rapid spatial variations in the top surface heat flux are significantly damped before reaching the interface. The damping strength is also determined by whether conduction or convection dominates the heat transfer process. Conduction through the solid end wall (characterized by $\lambda_s t$) and convection at the bottom surface (characterized by $\bar{h}$) compete with each other, and their relative importance controls how much the spatial variations of the imposed heat flux are attenuated.

C.2. Mass Flow Distribution

The steady-state flow distribution is determined by solving a nonlinear system that enforces equal pressure drop across all parallel channels with the same bulk cross-sectional area while maintaining the specified total mass flow rate. A decoupled Newton method is employed, which iteratively updates local channel mass flow rates and the global pressure drop in alternating steps until convergence.

Each channel j has a monotonically increasing pressure-mass flow relationship $\Delta P_j(\dot{m}_j)$, where steeper curves correspond to higher-resistance channels and gentler curves to lower-resistance channels. The physical steady state requires that all channels experience the same pressure drop ΔP^* while their individual mass flow rates sum to the prescribed total

$$\sum_{j=1}^{N_c} \dot{m}_j \;=\; \dot{m}_{\mathrm{tot}}. \tag{C.9}$$

Graphically, this steady state corresponds to a horizontal line at $y = \Delta P^*$ intersecting each channel curve $\Delta P_j(\dot{m}_j)$ at exactly one point. The abscissae of these intersection points correspond to the individual mass flow rates, $\dot{m}_j$.

The problem is formulated as a nonlinear system of $N_c + 1$ equations:

$$\begin{cases} f_j(\dot{m}_j) - \Delta P^* \;=\; 0, \quad j = 1, \ldots, N_c, \\ \displaystyle\sum_{j=1}^{N_c} \dot{m}_j - \dot{m}_{\text{tot}} \;=\; 0, \end{cases} \tag{C.10}$$

where $f_j(\dot{m}_j)$ represents the nonlinear pressure-mass flow characteristic of channel j. The structure of the problem, however, allows for an efficient decoupled approach: since channels interact only through the shared pressure drop ΔP^* rather than directly with one another, a diagonal Newton method can be used. In this method, each channel equation is independently updated, followed by a global correction to ΔP^* that enforces the prescribed total mass flow rate.

The iterative procedure begins with a uniform distribution of the total mass flow rate across all channels

$$\dot{m}_j^{(0)} = \frac{\dot{m}_{\text{tot}}}{N_c}, \qquad j = 1, \ldots, N_c. \tag{C.11}$$

This uniform distribution provides an initial guess for the common pressure drop

$$\Delta P^{*,(0)} = \frac{1}{N_c} \sum_{j=1}^{N_c} f_j(\dot{m}_j^{(0)}). \tag{C.12}$$

With these initial values established, the iterative process begins. For each channel j, it is possible to define the residual

$$r_j \;=\; f_j(\dot{m}_j) - \Delta P^*, \tag{C.13}$$

which measures the deviation from global pressure drop equilibrium. If $r_j > 0$, the channel pressure drop exceeds ΔP^* and the mass flow rate must be reduced; if $r_j < 0$, the mass flow rate is too low and needs to be increased. To correct this imbalance, a Newton step is applied to each channel independently yielding

$$\dot{m}_j^{(k+1)} \;=\; \dot{m}_j^{(k)} \;-\; \frac{r_j^{(k)}}{f_j'(\dot{m}_j^{(k)})}. \tag{C.14}$$

After the local mass flow rate updates, the total mass flow rate constraint is generally violated

$$g^{(k+1)} = \sum_{j=1}^{N_c} \dot{m}_j^{(k+1)} - \dot{m}_{\text{tot}} \neq 0. \tag{C.15}$$

Therefore, a scalar Newton step is applied to correct this global imbalance. The key insight is that each channel's flow rate responds to changes in the imposed pressure drop according to the implicit relationship $\dot{m}_j = f_j'(\Delta P^*)$. Differentiating this equilibrium condition with respect to ΔP^* reveals how each channel's mass flow rate adjusts: $\dot{m}_j / d(\Delta P^*) = 1/f_j'(\dot{m}_j)$. Summing these individual sensitivities gives the total response of the flow imbalance to the pressure adjustments

$$\frac{dg}{d(\Delta P^*)} = \sum_{j=1}^{N_c} \frac{d\dot{m}_j}{d(\Delta P^*)} \approx \sum_{j=1}^{N_c} \frac{1}{f_j'(\dot{m}_j)}. \tag{C.16}$$

Considering this, the global pressure drop update is then computed according to Equation C.17.

$$\Delta P^{*,(k+1)} = \Delta P^{*,(k)} - \frac{g^{(k+1)}}{\sum_{j=1}^{N_c} \left[1/f_j'(\dot{m}_j^{(k+1)})\right]} \tag{C.17}$$

The local channel updates (Equation C.14) and global pressure drop correction (Equation C.17) are iterated until both the pressure drop equilibrium and the imposed total mass flow rate are satisfied within specified tolerances:

$$\max_j |r_j| \leq \epsilon_p, \qquad |g| \leq \epsilon_m, \tag{C.18}$$

where ϵ_p and ϵ_m denote the pressure drop-equality and mass flow-balance tolerances, respectively. A simulation was considered to be converged, once both of these tolerances fell under 10^{-6}.

C.3. Grid Independence Study

Since both the end plate conduction problem and the mass flow rate distribution are computed numerically, the accuracy of the reduced-order model depends on the adequate grid resolution. The end plate conduction problem is particularly sensitive to discretization because the accurate representation of $\dot{q}_{\text{top}}(x, y)$ requires sufficient grid refinement to resolve spatial variations in the heating pattern.

To ensure the reliability of the numerical predictions, a grid independence study was conducted considering a cold plate configuration filled with gyroid structures with a porosity of 65%. The study systematically varied the number of channels, which directly controls the number of control volumes in the discretization. Grid convergence was assessed by monitoring key performance indicators, specifically the average wall temperature T_{w} and the pressure drop ΔP, as functions of grid refinement.

Figure 40 presents the results of the grid independence study. The number of channels varied from 4 to 64, resulting in a number of control volumes ranging from 12×8 to 192×128.

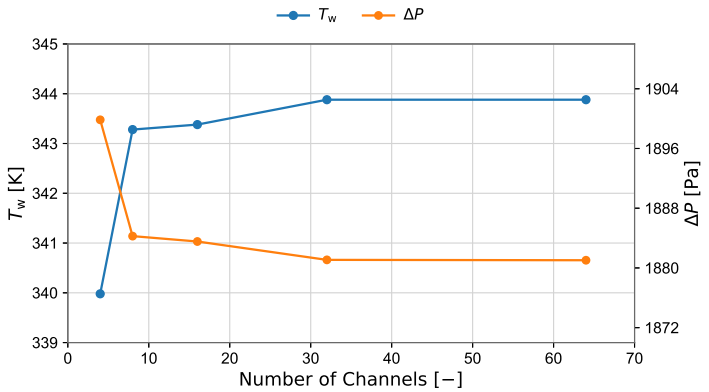

Figure 40: Results of the grid independence study of the discretized HERO model.

The results show that increasing the number of channels beyond 32 does not improve the predictions of the average wall temperature and pressure drop by more than 0.1%. Taking this into account, in the present analysis, the solutions obtained with the configuration with 32 channels were considered grid independent, and this discretization was adopted for the study.